Revista Brasileira de Ciências Mecânicas

Journal of the Brazilian Society of Mechanical Sciences

1

PUBLICAÇÃO DA ABCM - ASSOCIAÇÃO BRASILEIRA DE CIÊNCIAS MECÂNICAS

VOL. XIX - No.1 - MARCH 1997

ISSN 0100-738

JOURNAL OF THE BRAZILIAN SOCIETY OF MECHANICAL SCIENCES
REVISTA BRASILEIRA DE CIÊNCIAS MECÂNICAS

REVISTA BRASILEIRA DE CIÊNCIAS MECÂNICAS
JOURNAL OF THE BRAZILIAN SOCIETY OF MECHANICAL SCIENCES
Vol. 1. Nº 1 (1979)-
Rio de Janeiro: Associação Brasileira de Ciências Mecânicas
Trimestral
Inclui referências bibliográficas.
1. Mecânica
ISSN-0100-7386

A REVISTA BRASILEIRA DE CIÊNCIAS MECÂNICA publica trabalhos que cobrem os vários aspectos da ciência e da tecnologia em Engenharia Mecânica, incluindo interfaces com as Engenharias Civil, Elétrica, Química, Naval, Nuclear, Aeroespacial Alimentos, Agrícola, Petróleo, Materiais, etc., bem como aplicações da Física e da Matemática à Mecânica.

INDEXED by Applied Mechanics Reviews and Engineering Information, Inc.

Publicação da / Published by
ASSOCIAÇÃO BRASILEIRA DE CIÊNCIAS MECÂNICAS
THE BRAZILIAN SOCIETY OF MECHANICAL SCIENCES

Secretária da ABCM : **Ana Lúcia Fróes de Souza**
Avenida Rio Branco, 124 18º Andar
20040-001 Rio de Janeiro RJ
Tel.: (021) 221-0438/Fax: (021) 222-7128

Presidente: **Carlos Alberto de Almeida**
Vice-Presidente: **Arthur Palmeira Ripper Neto**
Secretário Geral: **Hans Ingo Weber**
Diretor de Patrimônio: **Felipe Bastos de F. Rachid**
Secretário: **Paulo Batista Gonçalves**

Secretária da RBCM: **Maria de Fátima Alonso de Souza**
UNICAMP - FEM - C.P. 6122
13083-970 Campinas SP
Tel.: (019) 239-8353/Fax: (019) 239-3722

EDITOR:
Leonardo Goldstein Júnior
UNICAMP FEM - DETF - C.P. 6122
13083-970 Campinas SP
Tel.: (019) 239-3006 Fax: (019) 239-3722

EDITORES ASSOCIADOS:
Agenor de Toledo Fleury
IPT - Instituto de Pesquisas Tecnológicas
Divisão de Mecânica e Eletricidade - Agrupamento de Sistemas de Controle
Cidade Universitária - C.P. 7141
01064-970 São Paulo SP
Tel.: (011) 268-2211 Ramal 504 Fax: (011) 869-3353

Angela Ourivio Nieckele
Pontifícia Universidade Católica do Rio de Janeiro
Departamento de Engenharia Mecânica
Rua Marquês de São Vicente, 225 Gávea
22453-900 Rio de Janeiro RJ
Tel.: (021) 239-0719 Fax: (021) 294-9148

Carlos Alberto Carrasco Altermani
UNICAMP - FEM - DE C.P. 6122
13083-970 Campinas SP
Tel.: (019) 239-8435 Fax: (019) 239-3722

Paulo Eigi Miyagi
Universidade de São Paulo - Escola Politécnica
Departamento de Engenharia Mecânica - Mecatrônica
Avenida Prof. Mello Moraes, 2231
05508-900 São Paulo SP
Tel.: (011) 818-5580 Fax: (011) 818-5471/813-1886

Walter L. Weingaertner
Universidade Federal de Santa Catarina
Departamento de Engenharia Mecânica - Laboratório de Mecânica de Precisão
Campus Universitário Trindade - C.P. 476
88040-902 Florianópolis SC
Tel.: (048) 231-9395/234-5277 Fax: (048) 234-1519

CORPO EDITORIAL:

Alcir de Faro Orlando (PUC-RJ)
Antonio Francisco Fortes (UnB)
Armando Albertazzi Jr. (UFSC)
Atair Rios Neto (INPE)
Benedito Moraes Purquerio (EESC-USP)
Caio Mario Costa (EMBRACO)
Carlos Alberto de Almeida (PUC-RJ)
Carlos Alberto Martin (UFSC)
Clovis Raimundo Maliska (UFSC)
Emanuel Rocha Woiski (UNESP-FEIS)
Francisco Emilio Baccaro Nigro (IPT-SP)
Francisco José Simões (UFPb)
Genesio José Menon (EFEI)
Hans Ingo Weber (UNICAMP)
Henrique Rozenfeld (EESC USP)
Jair Carlos Dutra (UFSC)
João Alziro Herz de Jornada (UFRGS)
José João de Espindola (UFSC)
Jurandir Itizo Yanagihara (EP USP)
Lirio Schaeter (UFRGS)
Lourival Boehs (UFSC)
Luis Carlos Sandoval Goes (ITA)
Marcio Ziviani (UFMG)
Moyses Zindeluk (COPPE-UFRJ)
Nisio de Carvalho Lobo Brum (COPPE-UFRJ)
Nivaldo Lemos Cupini (UNICAMP)
Paulo Afonso de Oliveira Soviero (ITA)
Rogério Martins Saldanha da Gama (LNCC)
Valder Steffen Jr (UFU)

REVISTA FINANCIADA COM RECURSOS DO

Programa de Apoio a Publicações Científicas

MCT CNPq FINEP

RBCM - J. of the Braz. Soc. Mechanical Sciences
Vol. XIX - No. 1 - 1997 - pp. 1-14

ISSN 0100-7386
Printed in Brazil

Heat Transfer to Viscoplastic Fluids in Laminar Flow Through Isothermal Short Tubes

Márcia Soares
Paulo Roberto Souza Mendes
Mônica Feijó Naccache
Pontifícia Universidade Católica do Rio de Janeiro
Departamento de Engenharia Mecânica
22453 Rio de Janeiro, RJ Brasil

Abstract

The heat transfer problem that occurs during the laminar flow of a Herschel-Bulkley fluid through the entrance portion of tubes is studied. The Nusselt number is obtained as a function of the axial coordinate, yield stress, and power-law exponent. The thermal boundary condition of uniform wall temperature is examined. Among other results,it is seen that the developing length decreases as the fluid behavior departs from the Newtonian one.
Keywords: Non-Newtonian Fluid Heat Transfer, Viscoplastic Fluid, Laminar Flow, Entrance-Region Flow, Uniform Wall Temperature.

Introduction

Non-isothermal viscoelastic flow situations are present in numerous processes found in the industries of food, cosmetics, paint, plastics, petroleum and many other. Some important non-Newtonian engineering fluids frequently involved in industrial processes are sludge, slurries, grease, paper pulp, polymer melts and solutions, aqueous foams, suspensions, most food products, cement, drilling mud, tooth paste, to name a few. In these processes, the temperature distribution in the liquid must be evaluated if its rheology is to be controlled.

As an engineering example, the process of drilling petroleum wells may be mentioned . Drill muds have a key role in this process, and are typically highly non-Newtonian in nature. They should have the correct density to provide the pressure needed for well integrity. Their rheological properties must be such as to allow carrying rock particles that are generated during drill aperation, with a minimum of pumping power. This requires a relatively low viscosity, but also a non-Zero yield stress limit. Also, the success of a well cementing operation depends to a great extent on the knowledge and control of the rheological properties of the cement.

Rheological properties are often strong functions of temperature. Because the fluids exchange heat with the surroundings as they flow, the temperature distributions can only be determined if heat transfer coefficients are known. In engineering applications, often the main goal is to obtain a flow rate / pressure drop, or flow rate / drag force relationship, for flows through ducts and other shear flows.

In these cases, an excellent representation of the mechanical behavior of viscoelastic liquids is obtained through the Generalized Newtonian Liquid model (GNL), in conjunction with a viscosity function of the Herschel-Bulkley type:

$$\tau = \eta\dot{\gamma} \tag{1}$$

where

$$\eta = \begin{cases} \dfrac{t_0}{\dot{\gamma}} + K\dot{\gamma}^{n-1} & \text{if } \tau > \tau_0; \\ \infty & \text{otherwise.} \end{cases} \tag{2}$$

Manuscript received: September 1996. Technical Editor: Angela Ourívio Nieckele

In Eq. (1), τ is the extra-stress tensor, $\dot{\gamma}$ the rate-of-deformation tensor, defined as grad v+ (grad $\mathbf{v})^T$, where $\mathbf{v}$ is the velocity vector. In Eq. (2), τ_0 is the yield stress, $\tau \equiv \sqrt{1/2\, tr\, \tau^2}$ a measure of the magnitude of τ, $\dot{\gamma} \equiv \sqrt{1/2\, tr\, \dot{\gamma}^2}$ a measure of the magnitude of $\dot{\gamma}$, K the consistency index, and n the power-law exponent. These three parameters (τ_0, K and n) are normally determined via least squares fit to experimental shear data.

While the power-law exponent, n, is often insensitive to the temperature of the liquid, this is typically not the case for both K and τ_0.

For laminar flow of power-law fluids[1] in ducts, some heat transfer information is available. For fully developed flow and uniform wall temperature, Bird et al. (1987) give Nu = 3.657, 3,949 and 4.175 respectively for the power-law exponent n = 1,0.5 and 1/3. For fully developed flow and uniform wall heat flux, Irvine and Karni (1987) present,

$$Nu = \frac{8(5n+1)(3n+1)}{31n^2+12n+1} \tag{3}$$

Joshi and Bergles (1980a, 1980b) reported a comprehensive study for power-law fluids, including both entrance region and fully developed results. In this study, they obtained correlations for q_w = constant, and considered the temperature dependence of K. Another detailed study for flow and heat transfer to pseudo-plastic liquids is presented by Scirocco et al. (1985). In both studies, at the inlet of the heated portion of the test section, the velocity profiles were already fully developed.

For turbulent flow, the thermal boundary condition becomes of minor importance, and the entry length becomes much shorter. Moreover, the shear rates are so large that the yield stress limit becomes unimportant. Therefore, information for power-law fluids and for fully developed flow can be employed for a wide range of situations. Irvine and Karni (1987) recommend Yoo's empirical correlation for predicting turbulent heat transfer, valid in the range $0.2 \le n \le 0.9$:

$$j_H \equiv \frac{Nu}{Re\, Pr^{1/3}} = \frac{0.0152}{Re^{0.155}} \tag{4}$$

where

$$Re = \frac{\rho\, \bar{u}^{2-n} D^n}{K} \left(\frac{2(3n+1)}{n} \right)^{1-n} \tag{5}$$

and

$$Pr = \frac{K c_p}{k} \left(\frac{(3n+1)}{4n} \right)^{n-1} \left(\frac{8\bar{u}}{D} \right)^{n-1} \tag{6}$$

In the above expressions, D is the tube diameter, ρ the mass density, $\bar{u}$ the average velocity, c_p the specific heat, and k the thermal conductivity. Yoo's correlation can be used for Re's in the range $3000 \le Re \le 90000$. From Eq. (4), it can be seen that j_H is a rather weak function of Re.

---

[1] A power -law fluid has a viscosity function that is well represented by Eq. (2) with $\tau_0 = 0$

Due to the industrial importance of non-Newtonian liquids that possess a non-zero yield stress, it is rather surprising that heat transfer information is so scarce in the open literature. Vradis et al. (1993), analyzed numerically the heat transfer problem for entrance-region flows of Bingham, constant-property liquids througt tubes. They considered the case of simultaneous velocity and temperature development. More recently, an experimental and theoretical heat transfer study for Herschel-Bulkley liquids is reported by Nouar et al. (1994). They also investigated the entrance region, but considered fully developed velocity profiles An interesting discussion regarding the impact of temperature-dependent rheological properties on velocity profiles and Nusselt numbers can be found there.

The purpose of the research reported here is to present laminar heat transfer coefficients for entrance-region flows in isothermal-wall tubes (T_w = constant) of yield-pseudoplastic liquids. The case of simultaneos velocity and temperature development is considered, and the liquids are assumed to obey the Herschel-Bulkley model. It is part of a research program whose first results, for fully developed flows of Herschel-Bulkley fluids, were recently reported by Souza Mendes and Naccache (1995). The conservation equations of mass, linear momentum and energy are solved numerically via a finite volume technique. Velocity, pressure and temperature fields are presented and discussed. The Nusselt number is also determined as a function of the (inverse) Graetz number and rheological parameters, namely, a dimensionless form of the yield stress limit and the power-law exponent.

Analysis

The flow under analysis is steady and axisymmetric. The thermophysical and rheological properties of the flowing fluid are independent of temperature. The fluid is a Generalized Newtonian Liquid (Eq. (1)) whose viscosity function is of the Herschel-Bulkley type (Eq. (2)), and enters the tube with uniform velocity and temperature profiles.The tube inner wall is kept at a uniform temperature, T_w, which is different from T_i, the inlet temperature.

Conservation of Momentum: Fully Developed Flow

The analysis begins by choosing characteristic quantities. Appropriate choices are very important, in order to yield convenient dimensionless forms for the governing equations.In this work we employ the fully developed values of some key quantities as characteristic. For example, the characteristic shear rate , $\dot{\gamma}_c$, is chosen to be the one that occurs at the wall in the fully developed region:

$$\dot{\gamma}_c \equiv \left(\frac{\tau_{R,fd} - \tau_0}{K} \right)^{\frac{1}{n}} \tag{7}$$

Where $\tau_{R,fd}$ is the shear stress at the wall in the fully developed region:

$$\tau_{R,fd} \equiv [\tau_{rx}(R)]_{fd} = -\left(\frac{dp}{dx}\right)_{fd} \frac{R}{2} = \frac{\Delta p}{L_{fd}} \frac{R}{2} \tag{8}$$

The subscript 'fd' indicates that quantity is to be evaluated in the fully developed region. In the above expression, p is the pressure, x the axial coordinate, R the tube radius, and L_{fd} a tube length in the fully developed region to whose ends the pressure difference Δp corresponds.

The characteristic viscosity is chosen as:

$$\eta_c \equiv \eta\,(\dot{\gamma}_c) = \frac{\tau_{R,fd}}{\dot{\gamma}_c} \tag{9}$$

Defining a dimensionless shear rate as $\dot{\gamma}' \equiv \dot{\gamma} / \dot{\gamma}_c$ and the dimensionless viscosity function as $\eta' \equiv \eta / \eta_c$, we can write:

$$\eta' = \begin{cases} \dfrac{\tau_0'}{\dot{\gamma}'} + (1 - t_0')\dot{\gamma}'^{\,n-1}, & \textit{if } \tau' > \tau_0', \\ \infty & \textit{otherwise} \end{cases} \tag{10}$$

Where

$$\tau' \equiv \frac{-\tau_{rx}}{\tau_{R,fd}} \quad \textit{and} \quad \tau_0' \equiv \frac{\tau_0}{\tau_{R,fd}} \tag{11}$$

In the fully developed region the shear stress is a linear function of the radial coordinate, r, i.e.,

$$\tau_{rx}(r) = -\tau_{R,fd}\,\frac{r}{R} \tag{12}$$

or, defining $r' \equiv r / R$,

$$\tau' = r' \quad \textit{and} \quad r_0' = \tau_0' \tag{13}$$

From Eq. (13) it is easy to observe that, in the fully developed portion of the flow, τ_0' has an important physical meaning: it is the dimensionless radial position where $\tau_{rx} = -\tau_0$. In other words, it is the radius of the plug-flow region that occurs in the flow core due to the existence of a non-zero yield stress. Because Eq. (13) holds for fully developed flow only, this interpretation of r_0' is not applicable in the entrance region.

For the Herschel-Bulkley fluid, and for $\tau > \tau_0$,

$$\tau' = \tau_0' + (1 - \tau_0')\dot{\gamma}'^{\,n} \tag{14}$$

Therefore, for fully developed flow conditions we can use Eq. (13) to obtain

$$r_0' + (1 - r_0')\dot{\gamma}'^{\,n} = r' \tag{15}$$

Defining a dimensionless axial velocity as

$$u' \equiv \frac{u}{R\dot{\gamma}_c} \tag{16}$$

and observing that

$$\dot{\gamma}' = -\frac{1}{\dot{\gamma}_c}\frac{du}{dr} = -\frac{du'}{dr'} \tag{17}$$

we can write Eq. (15) as

$$-\frac{du'}{dr'} = \left(\frac{r' - r_0'}{1 - r_0'}\right)^{1/n} \tag{18}$$

Integrating this equation and rearranging, we get

$$u'(r') = \frac{n}{n+1}\left(\frac{1}{1-r_0'}\right)^{\frac{1}{n}}\left[(1-r_0')^{\frac{n+1}{n}} - (r'-r_0')^{\frac{n+1}{n}}\right] \tag{19}$$

if $r' > r_0'$, *and*

$$u'(r') = \frac{n}{n+1}(1 - r_0') \tag{20}$$

if $r' \leq r_0'$.

From the definition of average velocity

$$\bar{u}' = 2\int_0^1 u'r'dr' \quad or \quad \bar{u}' = u_0' r_0'^2 + 2\int_{r_0}^1 \bar{u}'r'dr' \tag{21}$$

where $u_0' \equiv u'(r_0')$ Integrating, we get the following expression for $\bar{u}'$:

$$\bar{u}' = \frac{2n}{n+1}\left[\frac{1}{2}(1-r_0') - \frac{n}{2n+1}(r_0')(1-r_0')^2 - \frac{n}{3n+1}(1-r_0')^3\right] \tag{22}$$

It is observed that Eq. (22) reduces to Hagen-Poiseuille's, for the Newtonian case, and to the corresponding results for (i) the Bingham plastic (Buckingham equation) and (ii) the power-law fluid.

Another result of potential interest, easily obtained by Eq. (22), is an expression for the fully-developed wall shear rate, $\dot{\gamma}_c$ as a function of the average velocity, $\bar{u}$:

$$\dot{\gamma}_c = \frac{\bar{u}}{\bar{u}'R} = \frac{\bar{u}}{R}\frac{n+1}{2n}\left[\frac{1}{2}(1-r_0')-\frac{n}{2n+1}(r_0')(1-r_0')^2-\frac{n}{3n+1}(1-r_0')^3\right]^{-1} \tag{23}$$

As expected, when $r_0'=0$, the above equation reduces to the well-known expression for the fully-developed wall shear rate observed in flows of power-law fluids, namely:

$$\dot{\gamma}_{c,\ power\ law} = \left(\frac{8\bar{u}}{D}\right)\frac{3n+1}{4n} \tag{24}$$

Conservation of Mass and Momentum: Entrance Region

For the entrance steady flow of a Herschel-Bulkley fluid through a duct, the dimensionless mass and momentum equations are:

$$\frac{\partial u'}{\partial x'}+\frac{1}{r'}\frac{\partial (r'v')}{\partial r'}=0 \tag{25}$$

$$\begin{aligned} v'\frac{\partial u'}{\partial r'}+u'\frac{\partial u'}{\partial x'} &= -\frac{\partial p'}{\partial x'}+\frac{2\bar{u}'}{Re}\left[\frac{1}{r'}\frac{\partial}{\partial r'}\left(\eta' r'\frac{\partial u'}{\partial r'}\right)+\frac{\partial}{\partial x'}\left(\eta'\frac{\partial u'}{\partial x'}\right)\right. \\ &\quad +\frac{2\bar{u}'}{Re}\left[\frac{\partial \eta'}{\partial r'}\frac{\partial v'}{\partial x'}+\frac{\partial \eta'}{\partial x}\frac{\partial u}{\partial x'}\right] \end{aligned} \tag{26}$$

$$\begin{aligned} v'\frac{\partial v'}{\partial r'}+u'\frac{\partial p'}{\partial r'} &= -\frac{\partial v'}{\partial x'}+\frac{2\bar{u}'}{Re}\left[\frac{\partial}{\partial r'}\left(\frac{1}{r'}\frac{\partial}{\partial r'}(\eta' r' v')\right)+\frac{\partial}{\partial x'}\left(\eta'\frac{\partial v'}{\partial x'}\right)\right] \\ &\quad +\frac{2\bar{u}'}{Re}\left[\frac{\partial \eta'}{\partial r'}\frac{\partial v'}{\partial r'}+\frac{\partial n'}{\partial x'}\frac{\partial u'}{\partial r'}-\eta'\frac{v'}{r'^2}\right] \end{aligned} \tag{27}$$

In these equations, $u'=u/R\dot{\gamma}_c$, $v'=v/R\dot{\gamma}_c$, $x'=x/R$, *and* $p'=p/\rho\,(R\dot{\gamma}_c)^2$. The Reynolds number is defined as

$$Re \equiv \frac{\rho\,\bar{u}D}{\eta_c} = \frac{2\rho\,(\bar{u}')^{n-1}(\bar{u})^{2-n}R^n}{K+\tau_0{}^{(\bar{u}')^n R^n}_{\quad(\bar{u})^n}} \tag{28}$$

It is interesting to observe that, when $\tau_0 = 0$ Eq.(28) reduces to Eq.(5), which is a widely used expression for the Reynolds number for flows of power-law fluids.

As $x' \to \infty$, the dimensionless x-component of velocity, $u'(r',x')$ should approach the analytical solution for fully-developed flow, given by Eqs. (19) and (20).

The boundary conditions are the usual no-slip condition at the wall, the symmetry condition at the centerline, uniform velocity profile at the tube inlet, and locally parabolic flow at the outlet:

$$\begin{array}{ll} \dfrac{\partial u'}{\partial r'}(0,x') = 0 & v'(0,x') = 0 \\ u'(1,x') = 0 & v'(1,x') = 0 \\ u'(r',0) = \overline{\mu}' & v'(r',0) = 0 \\ \dfrac{\partial u'}{\partial x'}(r',L') = 0 & \dfrac{\partial v'}{\partial x'}(r',L') = 0 \end{array} \qquad (29)$$

where $L' \equiv L/R$ is the dimensionless tube length.

Modified Bi-viscosity Model

The viscosity function as given by Eq. (10) is not convenient to handle numerically. The usual approach in numerical schemes for flows of Bingham plastics is to replace it with an-other viscosity function, the so called bi-viscosity model (Beverly and Tanner, 1992). This idea can be easily extended to Herschel-Bulkley fluids, yielding the following approximate representation of the viscosity function:

$$n' = \begin{cases} \dfrac{r_0'}{\dot{\gamma}} + (1-r_0')\dot{\gamma}'^{n-1} & if\ \dot{\gamma}' > \dot{\gamma}'_{small} \\ \eta'_{large} & otherwise \end{cases} \qquad (30)$$

Beverly and Tanner (1992) recommend

$$\eta'_{large} = 1000 \qquad (31)$$

Therefore,

$$\dot{\gamma}'_{small} = \frac{r_0'}{1000 - (1-r_0')\dot{\gamma}'^{n-1}_{small}} \cong \frac{r_0'}{1000} \qquad (32)$$

Conservation of Energy

We now turn to the thermal problem for uniform wall temperature (T_w = constant).

Neglecting viscous dissipation effects and assuming that the thermal conductivity is a constant, the dimensionless energy equation for this situation is

$$u'\frac{\partial\theta}{\partial x'}+v'\frac{\partial\theta}{\partial r'}=\frac{2\bar{u}'}{Pe}\left\{\frac{\partial^2\theta}{\partial x'^2}+\frac{1}{r'}\frac{\partial}{\partial r'}\left(r'\frac{\partial\theta}{\partial r'}\right)\right\} \tag{33}$$

where $\theta\equiv(T-T_w)/(T_i-T_w)$ is the dimensionless temperature, $Pe\equiv\bar{u}D/\alpha$ the peclet number, and $\alpha\equiv k/(\rho c_p)$ the thermal diffusivity. Equation (33) shows that, when viscous dissipation effects are negligible, the influence of rheological behavior on heat transfer is conveyed through the velocity field only.

The boundary conditions for Eq. (33) are

$$\begin{array}{ll}\frac{\partial\theta}{\partial r'}(0,x')=0 & \theta\,(1,x')=0\\ \theta\,(r',0)=1 & \frac{\partial\theta}{\partial x'}(r',L')=0\end{array} \tag{34}$$

For this situation, the Nusselt number becomes

$$Nu(x')\equiv\frac{hD}{k}=-\frac{2}{\theta_b(x')}\frac{\partial\theta}{\partial r'}(1,x') \tag{35}$$

where

$$\theta_b\equiv 2\int_0^1\frac{u'}{\bar{u}'}\theta\; r'dr' \tag{36}$$

Numerical Solution

The conservation equations are discretized by the finite volume method described by Patankar (1980). Staggered velocity components are employed to avoid unrealistic pressure fields. The pressure-velocity coupling is handled by the SIMPLEC algorithm (Van Doormaal and Raithby, 1984). The resulting algebraic system is solved by the TDMA line-by-line algorithm (Patankar, 1980) with the block correction algorithm (Settari and Aziz, 1973) to increase the convergence rate.

A non-uniform 140 x 32 grid is employed, with points concentrated toward the inlet region in the x-direction, and toward the wall in the r-direction, to resolve the sharp gradients in these regions. The domain length in the axial direction, L, is equal to fifteen diameters for the low Pe cases, and ninety five diameters for the high Pe cases. Extensive grid tests were performed, which attested that the solutions obtained are grid-independent.

Results and Discussion

Results for some representative combinations of the governing parameters are now presented and discussed.

Figures 1 and 2 show velocity profiles at four different axial position along the entrance region. Is is seen in these figures that, close to the tube inlet, there is a velocity overshoot near the wall.This overshoot is related to axial diffusion of momentum, and therefore cannot be predicted by formulations that consider radial diffusion only. Although milder than the one observed for Newtonian fluids, this effect is not negligible, and might have important impact in heat transfer.

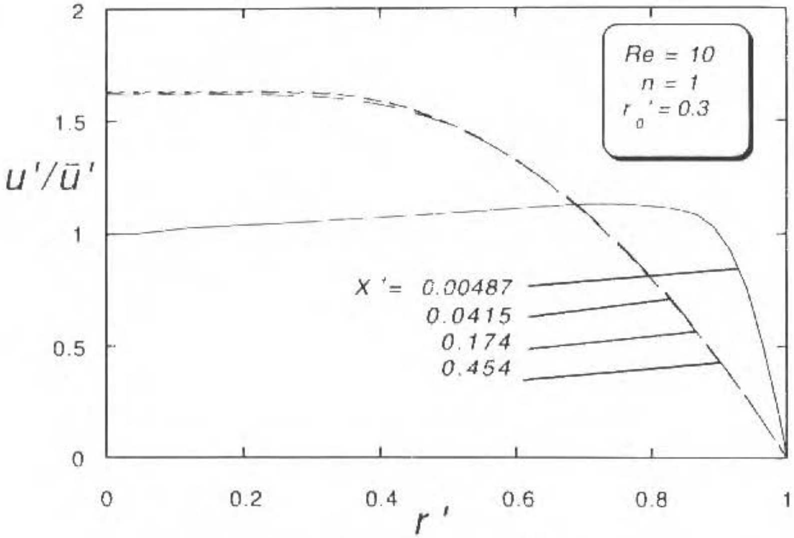

Fig. 1 Velocity Profiles - Bingham Fluid

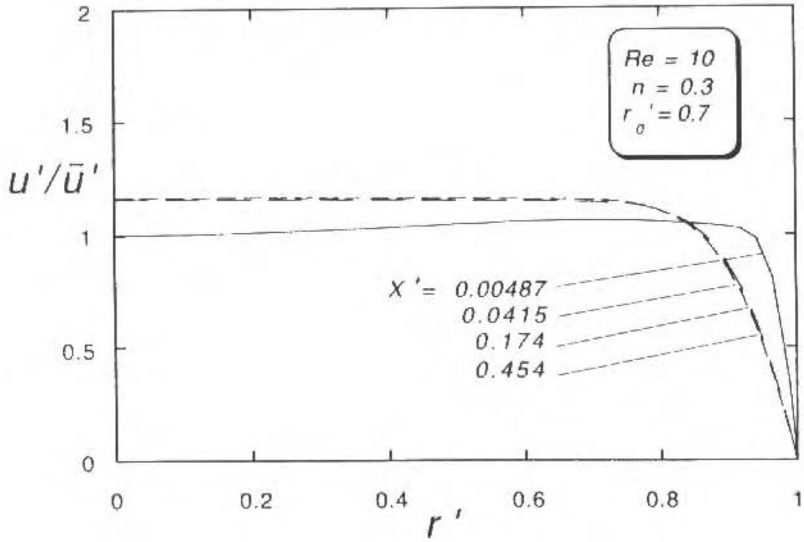

Fig. 2 Velocity Profiles - Herschel-Bulkley Fluid

Temperature profiles at some axial locations are seen in Figs. 3 and 4. In order to eliminate x-dependence in the fully developed region, these profiles are presented as a ratio of θ *to* θ_b. Because the Prandtl number, defined as $Pr \equiv n_c / \rho\, \alpha = Pe / Re$, is equal to 5, the temperature profiles for the cases shown take larger development lengths than the corresponding velocity profiles, shown in Figs. 1 and 2.

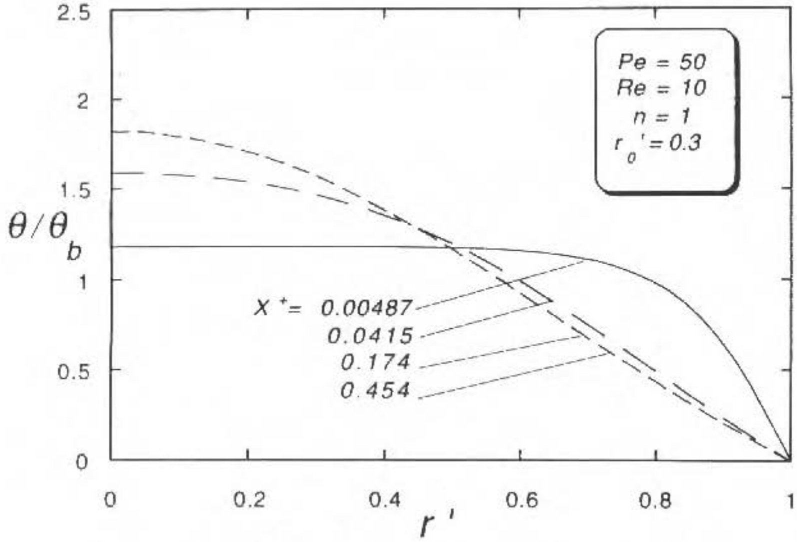

Fig. 3 Temperature Profiles - Bingham Fluid

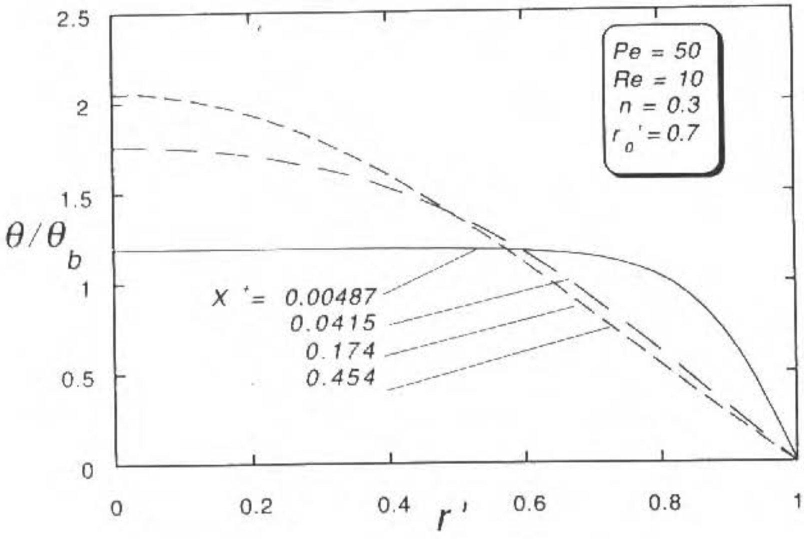

Fig. 4 Temperature Profiles - Herschel - Bulkley Fluid

Figure 5 shows the Nusselt number variation with the inverse Graetz number, $x^+ \equiv x'/Pe$,for a number of combinations of r_0' and n. It is seen that,whenever the velocity gradient is high in the neighborhood of the wall, the Nusselt number is also high. High $r_0''s$ imply high velocity gradients near the wall, as does low n's . For example, the curve for $r_0' = 0.7$ and $n = 0.3$ falls above all other in Fig. 5, while the curve for $r_0' = 0.3$ and $n = 1.0$ gives the lowest Nu for a given x^+.

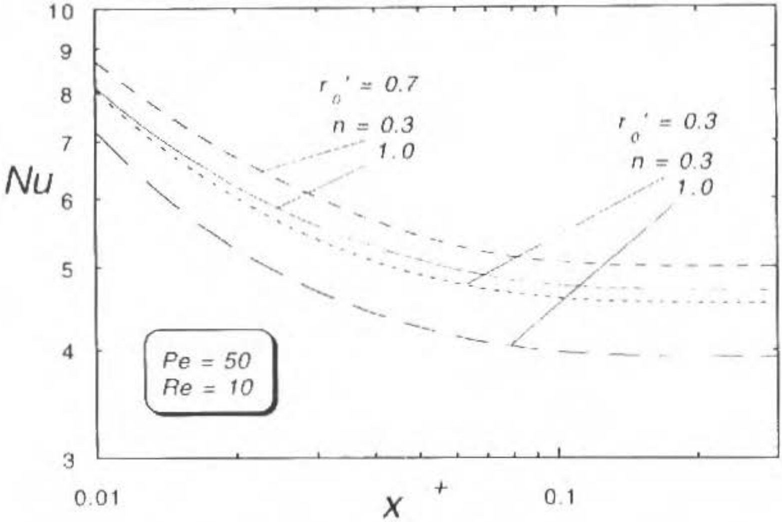

Fig. 5 Entrance-Region Nu for Different $r_0''s$ and n's

Figures 6 and 7 illustrate the entrance-region Nusselt number variation with the Peclet number, for some combinations of the governing parameters. It is interesting to observe that axial conduction is important in the vicinity of the tube inlet only, and its effect is to increase the Nusset number. Larger yield stresses tend to decrease the axial conduction effect. On the hand, axial conduction is not greatly affected by the power-law exponent in the range investigated

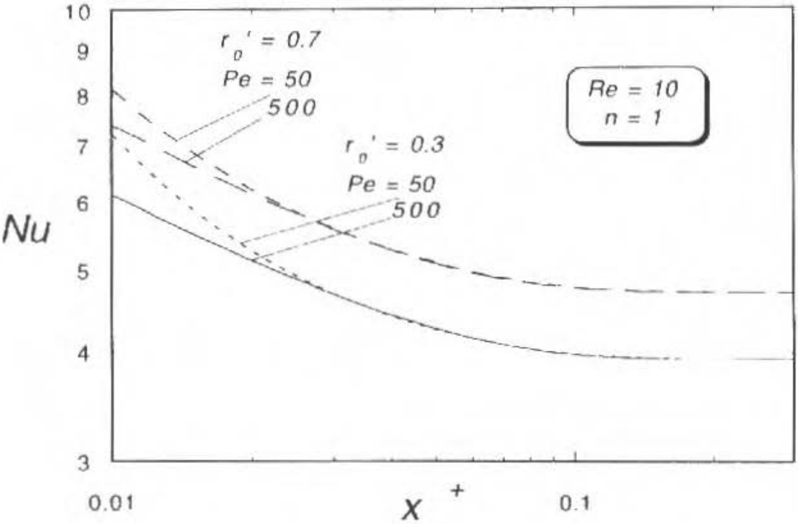

Fig. 6 Entrance-Region Nu for Different $r_0''s$ and Pe's

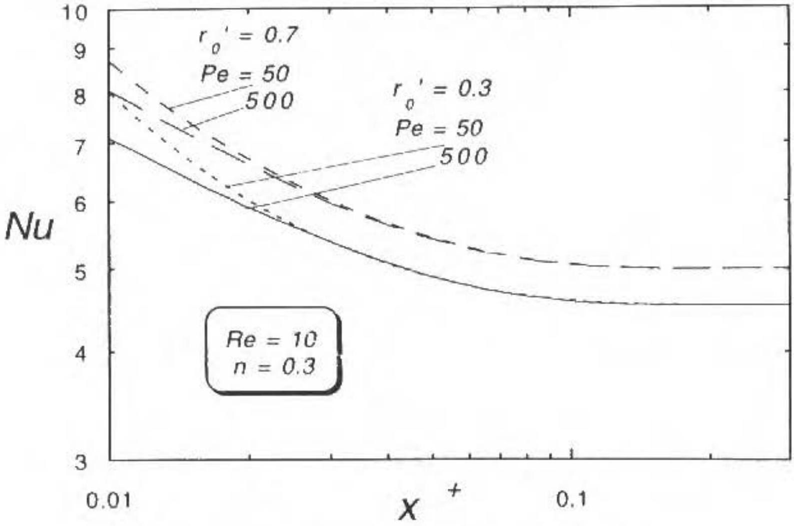

Fig. 7 Entrance-Region Nu for Different r_0''s and Pe's

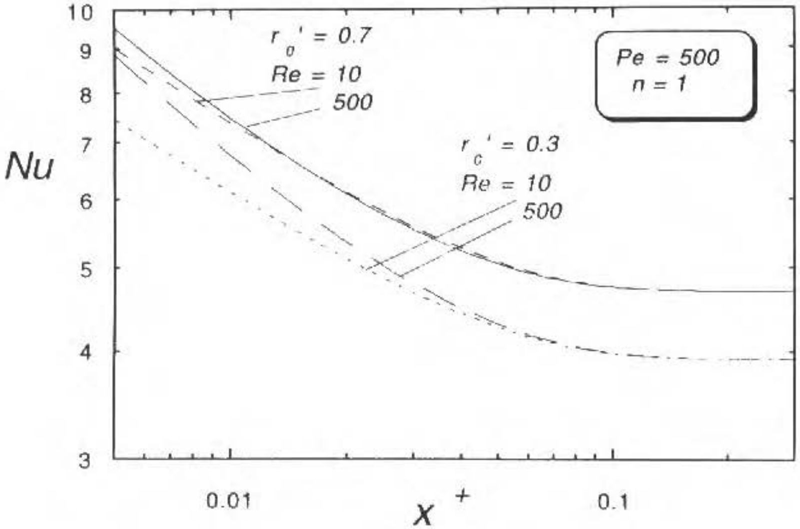

Fig. 8 Entrance-Region Nu for Different r_0''s and Re's

For the constant-property situations examined in this paper, the Nusselt number depends on the fluid rheology through its influence on the velocity profile only. Therefore, axial diffusion of momentum - which affects the velocity field - is expected to affect the Nusset number. This is illustrated in Figs. 8 and 9. It is seen in these Figures that the effect is restricted to the neighborhood of the tube inlet, and is negligible for high yield stress fluids. However, it becomes important as the rheological behavior approaches the Newtonian (higher n's and lower r_0''s).

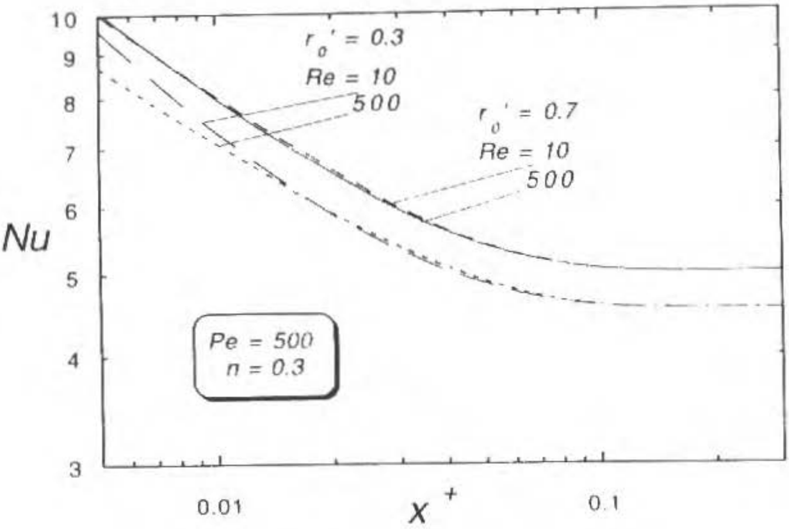

Fig. 9 Entrance-Region Nu for Different r_0''s and Re's

Conclusions

This paper has studied the heat transfer problem in the entrance-region flow of Herschel-Bulkley fluids. The case of uniform wall temperature and simultaneous development of velocity and temperature profiles is examined.

For fully developed flow, an analytical solution for the velocity profile is presented, which provides the characteristic quantities needed in the definition of the appropriate dimensionless governing parameters. Although in essence this analytical solution is already available in the open literature, the form of the solution presented here has some advantages. It is more compact,and gives the velocity in terms of two convenient dimensionless parameters, namely, n and r_0'.

The governing equations are solved numerically via a finite-volume technique. Results are presented in the form of velocity and temperature profiles, and entrance-region Nusselt number distributions.

Among other results, it is observed that the velocity profile presents an overshoot near the wall, in the tube neighborhood of the tube inlet, and that when the velocity gradient at the wall is high the Nusselt number is larger.

Aknowledgements

Financial support for the present research was provided by Petrobras S.A., CNPq and MCT.

References

Beverly, C. R., Tanner, R. I., 1992, "Numerical Analysis of Three-Dimensional Bingham Plastic Flow", J.Non-Newtonian Fluid Mechanics pp. 42,85-115.

Bird, R. B., Armstrong, R. C. and Hassager, O., 1987, "Dynamics of Polymeric Liquids", Vol. 1, Wiley

Irvine, Jr TF, Karni, J., 1987, "Non-Newtonian Fluid Flow and Heat Transfer", in Handbook of Single-Phase Convective Heat Transfer, edited by Kakaç S, R K Shah, W Aung, Wiley, p. 20.1-20.57.

Joshi SD, Bergles, AE, 1980a, "Experimental Study of Laminar Heat Transfer to In-Tube Flow of Non-Newtonian Fluids", J Heat Transfer 102, pp. 397-401.

Joshi SD, AE Bergles 1980b, "Analyical Study of Laminar Heat Transfer to In-Tube Flow of Non-Newtonian Fluids", AICHE Symposium Series, No 199, Vol. 76, pp. 270-281.

Nouar C, Devienne, R and Lebouche, M, 1994, "Convection Thermique Pour un Fluide de Herschel-Bulkley Dans la Région D'Entrée d'Une Conduite", Int. J. Heat Mass Transfer 37, pp.1-12.

Patankar S V 1980, Numerical Heat Transfer and Fluid Flow, Hemisphere Publishing Corporation.

Scirocco V, Devienne R., Lebouche, M 1985, "Écoulement Laminaire et Transfer de Chaleur Pour un Fluide Pseudo-Plastique Dans la Zone d'Entrée d'Un Tube", Int. J. Heat Mass Transfer 28, pp. 91-99.

Settari A, K Aziz, 1973, "A Generalization of the Additive Correction Methods for the Iterative Solution of Matrix Equations", SIAM J. Numerical Analyses 10, pp. 506-521.

Souza Mendes PR, MF Naccache, 1995, "Heat Transfer to Herschel-Bulkley Fluids in Laminar Fully Developed Flow Through Tubes", COBEM-CIDIM/95, Belo Horizonte (in CD-ROM).

Van Doormaal JP, GD Raithby, 1984, "Enhancements of the SIMPLE Method for Prediction Incompresible Fluid Flows", Numerical Heat Transfer 7, pp.147-163.

Vradis GC, Dougher, J. and Kumar, S., 1993, "Entrance Pipe Flow and Heat Transfer for a Bingham Plastic", Int. J. Heat Mass Transfer 36, pp. 543-552.

RBCM - J. of the Braz. Soc. Mechanical Sciences
Vol. XIX - No.1 - 1997 - pp. 15-29

ISSN 0100-7386
Printed in Brazil

Aspectos de Otimização na Estimação de Parâmetros Termofísicos

On Optimizing the Estimation of Thermophysical Properties

Gilmar Guimarães
Elias Bitencourt Teodoro
Universidade Federal de Uberlândia
Departamento de Engenharia Mecânica
38400-902 Uberlândia, MG Brasil

Paulo César Phillipi
Universidade Federal de Santa Catarina
Departamento de Engenharia Mecânica
88040-900 Florianópolis, SC Brasil

Abstract

This work presents an analysis of an experimental technique for simultaneous determination of the thermal conductivity and the thermal diffusivity of non metallic materials. The properties are determined by using the parameter estimation method. The experimental temperatures on the frontal and back surfaces of a sample are compared with their respective theoretical values obtained from the mathematical model. The heat flux evolution at the front surface and the heat loss evolution at the back surface are used as the boundary conditions. The purpose of this work is to investigate the ideal shape of the heat flux evolution, its duration and optimum measurement time. This information is important to guide designers on optimizing the parameters estimation.

Keywords : Optimization, Parameter Estimation, Experimental Techniques, Thermal Properties Measurements, Inverse Problems

Resumo

Este trabalho apresenta aspectos de otimização para uma técnica de estimação simultânea da condutividade e difusividade térmica de materiais sólidos. Nesse sentido uma análise de sensibilidade na estimação dos parâmetros em função da intensidade e duração do fluxo de calor imposto, espessura da amostra e tempo de medição é apresentada. Investiga-se também as formas ideais das evoluções desses fluxos de calor, sua duração e o tempo ótimo de medição, para a otimização de projetos de estimação de parâmetros. No método proposto as evoluções dos fluxos de calor são medidas por transdutores de fluxo de calor. Nessa análise as temperaturas e fluxos experimentais são simuladas numericamente.

Palavras-chave: Otimização, Estimação de Parâmetros, Técnicas Experimentais, Medição de Propriedades Térmicas, Problemas Inversos

Introdução

Existem vários métodos transientes que possibilitam a obtenção da condutividade térmica, λ, e da difusividade térmica, α. Todavia, esse número diminui quando se deseja a obtenção dessas propriedades de forma simultânea. Como exemplos, citam-se os métodos Flash, originalmente desenvolvido para a obtenção da difusividade térmica, (Parker et all, 1961) e o da Sonda Térmica, que mede a condutividade térmica, (Blackwell,1954). Ambos são capazes da obtenção simultânea das duas propriedades. Nesse caso, para o método Flash, é necessário conhecer-se o fluxo de calor imposto e, para o da Sonda térmica, um sensor de temperatura adicional deve ser inserido dentro da amostra.

Um método experimental compõe-se da concepção de um modelo físico a ser simulado experimentalmente e da técnica de obtenção das propriedades. Assim, um modelo físico ideal não deve impor nenhuma restrição nas condições de contorno, ou seja, nas evoluções de temperatura e/ou fluxos de calor superficiais enquanto a técnica de obtenção das propriedades deve ser capaz de obtê-las a partir de medições das grandezas superficiais.

A realização de qualquer experimento deve seguir, sempre, procedimentos que busquem o melhor resultado. Esses procedimentos passam não somente por um cuidado na execução de cada passo

Manuscript received: March 1996. Technical Editor: Angela Ourívio Nieckele

experimental mas também pela idealização de cada projeto. Nos casos de determinação de propriedades térmicas, torna-se importante a busca do projeto ótimo de experimentos em condução de calor. Esse trabalho apresenta análise de um método experimental, cujo modelo físico foi proposto por Guimarães (1993) e cuja técnica de obtenção simultânea das propriedades, λ e α é a técnica de estimação de parâmetros descrita por Beck et al. (1990).

O sucesso dessa técnica para os diversos materiais depende da escolha de parâmetros de projeto para a simulação experimental do modelo físico. A otimização de projetos de experimentos tem sido tema de um grande número de artigos entre os quais pode-se citar Beck (1969), Vigak et al (1989), Taktak et al (1993) e Artyukhin (1989). A maioria desses trabalhos focalizam, no entanto, a melhor posição para a localização de sensores de medição (normalmente termopares) ou o tempo ótimo de medição. Todavia, variáveis como parâmetros geométricos ou físicos como intensidade e forma do fluxo de calor imposto não tem sido estudados.

O presente trabalho investiga os vários parâmetros ótimos de projeto para materiais isolantes, semicondutores e condutores na determinação simultânea da condutividade e difusividade térmica. Apresenta-se assim, uma análise que busca a otimização de parâmetros de projeto como o fluxo de calor imposto (duração e forma de aquecimento), tempo de medição, características geométricas como espessura da amostra, L, e tipo de material (materiais condutores, semi-condutores e isolantes).

Uma das maiores dificuldades no uso da técnica de estimação de parâmetros é a escolha das regiões de medição onde, claramente, os coeficientes de sensibilidade (primeira derivada da temperatura em relação ao parâmetro estimado) são linearmente independentes. A identificação dessa região é fundamental para o uso da técnica. Nesse sentido, um estudo prévio de otimização dessas regiões, antes da definição do projeto, é extremamente importante. Além do aspecto de otimização da técnica, esse procedimento permite ainda, uma minimização significativa de custos operacionais. Nesse caso, seriam necessários o uso de um grande número de amostras, elementos de aquecimento e sensores de medição que, sem um estudo prévio, não estariam bem determinados. A definição dessa região para diversos tipos de materiais, bem como a indicação das melhores formas de imposição de calor são as principais contribuições desse trabalho.

Descrição do Método

A Figura 1 apresenta uma amostra plana, homogênea, sujeita a uma temperatura inicial T_0, cujo fluxo de calor unidimensional transiente, $\phi_1(t)$, é imposto num instante t_0 na superfície superior da amostra, e o fluxo de calor resultante, $\phi_2(t)$, atravessa a superfície oposta.

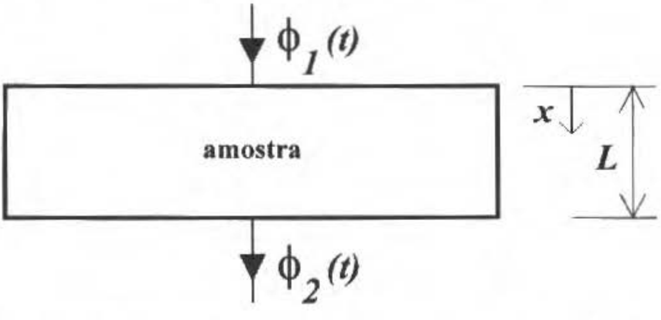

Fig. 1 Modelo Físico de uma Amostra Sujeita a Condições de Fluxos de Calor Superficiais

Sob estas condições, e considerando as propriedades térmicas constantes com a variação de temperatura, o problema apropriado a valor de contorno é

$$\frac{\partial^2 T}{\partial x^2} = \frac{1}{\alpha}\frac{\partial T}{\partial t} \tag{1}$$

sujeita às seguintes condições de contorno,

$$\phi(0,t) = -\lambda \frac{\partial T(0,t)}{\partial x} = \phi_1(t) \qquad (2)$$

$$\phi(L,t) = -\lambda \frac{\partial T(L,t)}{\partial x} = \phi_2(t) \qquad (3)$$

e à condição inicial

$$T(x,0) = T_0 \qquad (4)$$

onde T representa a temperatura e $\phi(t)$ o fluxo calor transiente nos contornos da amostra. Obtém-se a solução do problema dado pelas Equações (1-4) usando-se uma técnica de solução baseada nas funções de Green (Guimarães, 1993), ou seja,

$$\begin{aligned} T = T_0 &+ \frac{\alpha}{L\lambda}\int_0^t \phi_1(\tau)\,d\tau + \frac{\alpha}{L\lambda}\int_0^t \phi_2(\tau)\,d\tau \\ &+ \frac{2\alpha}{L\lambda}\sum_{m=1}^{\infty} e^{-\beta_m^2 \alpha t/L^2} \cos(\beta_m x/L) \int_0^t e^{\beta_m^2 \alpha t/L^2} \phi_1(\tau)\,d\tau \, . \qquad (5) \\ &+ \frac{2\alpha}{L\lambda}\sum_{m=1}^{\infty} [(-1)^m - 1]\, e^{-\beta_m^2 \alpha t/L^2} \cos(\beta_m x/L) \int_0^t e^{\beta_m^2 \alpha t/L^2} \phi_2(\tau)\,d\tau \end{aligned}$$

onde $\beta_m = m\pi$ com m=1, 2, 3 ... e $\phi_1(t)$ e $\phi_2(t)$ são os fluxos de calor definidos a partir de curvas de ajuste que podem ser obtidas sobre os valores medidos com os transdutores de fluxo de calor aplicados nas superfícies da amostra (Guimarães, 1993). Observa-se que o valor de m para o truncamento das séries ($m \rightarrow \infty$) foi escolhido de forma a se obter uma variação no cálculo da temperatura, Eq. (6), em qualquer tempo, inferior a 0,01K. Nesse caso, o valor usado foi m =600. Nesse sentido, o erro devido ao truncamento é bem inferior à própria incerteza de medição (0,25K) usada na simulação das temperaturas experimentais, não causando qualquer influência nos resultados.

Tendo estabelecido a solução formal do problema direto dado pelas Eqs. (1-4), estima-se os parâmetros λ e α minimizando-se a função mínimos quadrados (Beck et al., 1990) definida a seguir

$$S = \sum_{i=1}^{n}\sum_{j=1}^{2} [Y_j(i) - T_j(i)]^2 \qquad (6)$$

onde Yj(i) são as temperaturas experimentais e Tj(i) as temperaturas calculadas através do modelo teórico nas superfícies da amostra. Os sub-índices i e j representam, respectivamente, o instante discreto de medição e o número de sensores, no caso dois termopares, aplicados às superfícies (x=0 e x=L). Assim, os parâmetros λ e α são estimados para a obtenção da melhor concordância entre os valores das temperaturas medidas experimentalmente e aquelas obtidas através do modelo teórico. As equações de recorrência para as propriedades são obtidas através da minimização de Gauss da função S (Guimarães, 1993), ou seja, fazendo as primeiras derivadas de S em relação a cada parâmetro iguais a zero, como

$$\frac{\partial S}{\partial \lambda} = -2{,}0 \sum_{i=1}^{n} \sum_{j=1}^{2} [Y_j(i) - T_j(i)] \; X_{j1}(i) = 0 \tag{7}$$

e

$$\frac{\partial S}{\partial \alpha} = -2{,}0 \sum_{i=1}^{n} \sum_{j=1}^{2} [Y_j(i) - T_j(i)] X_{j2}(i) = 0 \tag{8}$$

onde Xj_k (i) são os coeficientes de sensibilidade definidos pela primeira derivada da temperatura em relação ao parâmetro estimado. O índice j representa a posição do sensor nas superfícies frontal (j=1,x=0) e oposta (j=2, x=L) e k o parâmetro a ser estimado λ (k=1) ou α (k=2). Assim, X_{jk} (i) podem ser definidos por

$$X_{11}(i) = \frac{\partial T_1}{\partial \lambda} \tag{9}$$

e

$$X_{21}(i) = \frac{\partial T_2}{\partial \lambda} \tag{10}$$

$$X_{12}(i) = \frac{\partial T_1}{\partial \alpha} \tag{11}$$

e

$$X_{22}(i) = \frac{\partial T_2}{\partial \alpha} \tag{12}$$

e representam um papel importante na técnica de estimação de parâmetros. Observa-se que para o sucesso da estimação simultânea de λ e α, é necessário que os coeficientes sejam linearmente independentes e, ainda, possuam os maiores valores possíveis (Beck et al., 1990) . As equações de recorrência para os parâmetros λ e α são bem conhecidas e podem ser encontradas nas referências de Beck et al (1990) ou Guimarães (1993).

Caracterização do Experimento através do Agrupamento $(q \times L)/\lambda$

Salienta-se que este trabalho visa a otimização dos parâmetros de projeto envolvidos na técnica de estimação de parâmetros. Nesse sentido, os dados experimentais são simulados numericamente, permitindo-se assim uma maior flexibilidade na análise de diferentes tipos de materiais e suas espessuras, além de considerável redução de custos.

Os diversos tipos de materiais são simulados através da variação do agrupamento $(\phi_1.L/\lambda)$, com os valores de λ e α representativos de materiais isolantes ($\lambda < 0.5$ W/mK), materiais semicondutores (0,5 W/mK $< \lambda <$ 10 W/mK) e materiais condutores (10 W/mK $< \lambda$) . A Tabela 1 apresenta os valores de λ e α usados na simulação.

Tabela 1 Valores de λ e α para Materiais Típicos Usados na Simulação

Propriedade	Material		
	Não Condutor	Semicondutor	Condutor
λ [W/mK]	0,4	5,0	70,0
α [m^2/s]	2,3x10^{-07}	16,0x10^{-07}	16,0x10^{-05}

Observa-se ainda que as temperaturas experimentais $Y_j(i)$ são simuladas numericamente usando-se as temperaturas teóricas e uma função erro aleatório, $\varepsilon_j(i)$, definidas por

$$Y_j(i) = T_j(i) + \varepsilon_j(i) \tag{13}$$

cujos limites são $-0{,}25 < \varepsilon_{j(i)} < 0{,}25$. Os limites máximos situam os erros aleatórios dentro da região de incerteza de medição de temperatura usando-se termopares adequados e calibrados (Guimarães, 1993). Para o cálculo de T_j (i) na Eq. (5) os valores de ϕ_1, ϕ_2 e λ, são fixados para cada teste. A Tabela 2 apresenta esses parâmetros.

Tabela 2 Teste 1 - Parâmetros Estimados para Material não Condutor.

Valores Iniciais	α = 1,0 x 10^{-07}m^2/s λ = 0,1W/mK		Fluxo de Calor Máximo			$\phi_{1(máx)}$ =200 W/m^2
λ [W/mK]	α x 10^7 [m^2/s]	L [mm]	Erro [%] λ	/ α	$(q \times L)/\lambda$ [K]	Teste
0,458	2,63	1,0	14,5	14,35	0,5	a
0,4114	2,363	5,0	2,85	2,74	2,5	b
0,406	2,331	10,0	1,5	1,35	5,0	c
0,404	2,313	20,0	1,0	0,57	10,0	d
Não convergiu	Não convergiu	40,0			20,0	e

Observa-se que a técnica de estimação de parâmetros usada nesse trabalho necessita de um procedimento iterativo. Assim quando há sucesso na estimação os valores iniciais de λ e α convergem a aqueles das propriedades da amostra investigada. Entretanto, como nesse trabalho os experimentos são simulados numericamente, os valores iniciais dos parâmetros devem, portanto, convergir aos valores de λ e α fixados para cada amostra simulada (Tabela 2). Inicialmente os testes foram realizados fixando-se o fluxo de calor imposto, ϕ_1, e o tipo de material (não condutor). Assim, variou-se a espessura entre 5 mm e 50 mm para um material isolante típico (Teste 1). O valor inicial de λ e α para todas as simulações são apresentados nas Tabelas 2 - 4.

A Figura 2 apresenta os perfis de temperatura na superfície frontal (x=0) para uma amostra não condutora. Observou-se que, para L superiores a 40 mm, as evoluções de temperatura nessa superfície passam a ter o mesmo comportamento.

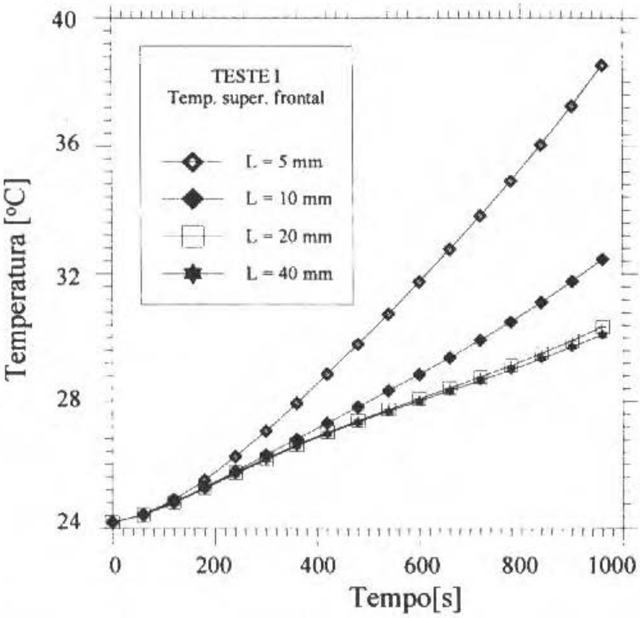

Fig. 2 Evolução da Temperatura na Superfície Frontal ao Aquecimento - Amostra não Condutora.

As Figuras 3-6 apresentam os coeficientes de sensibilidade para essa amostra variando-se os valores da espessura. (Teste 1). Observa-se, assim, que o melhor comportamento (coeficientes linearmente independentes) são para amostras de comprimento, L, iguais a 10 e 20 mm (Figs. 5 e 6)

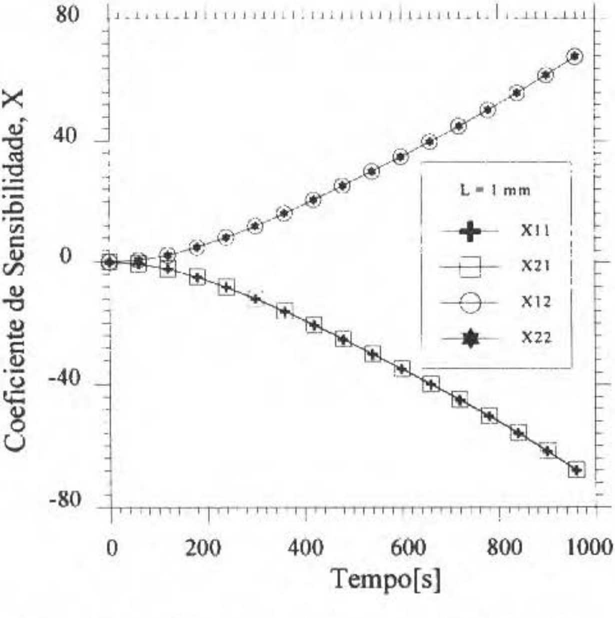

Fig. 3 Coeficientes de Sensibilidade - Amostra não Condutora, L = 1 mm

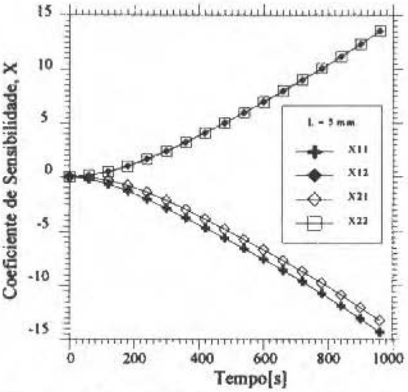

Fig. 4 Coeficientes de Sensibilidade - Amostra não Condutora, L = 5 mm

Este comportamento se reflete no sucesso das estimativas apresentadas na Tabela 2. Os erros percentuais na estimação de λ e α são, nesses casos, iguais ou inferiores a 1,5%. Uma inspeção nas Figs. 3 e 7 permite concluir que a dependência linear entre os coeficientes (Fig. 3) e seus baixos valores (Fig. 7) é a responsável pela falha na estimação apresentada na Tabela 2.

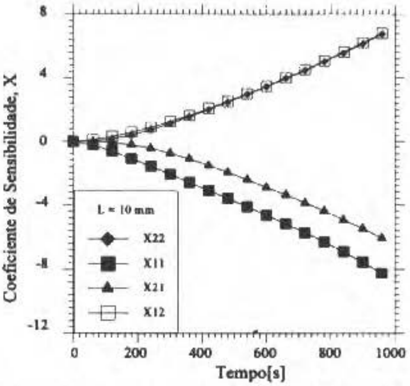

Fig. 5 Coeficientes de Sensibilidade - Amostra não Condutora, L = 10 mm.

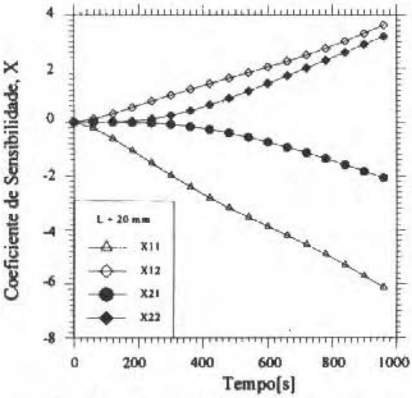

Fig. 6 Coeficientes de Sensibilidade - Amostra não Condutora, L = 20 mm.

Todavia, mantendo-se constantes a intensidade de fluxo de calor imposto imposto ($200 W/m^2$) e a espessura (L=10 mm), para materiais condutores e semicondutores, nenhum teste de estimação obteve sucesso. A principal razão, nesse caso, é a pequena diferença entre os perfis de temperatura entre as superfícies. (Figs. 8 e 9). Pode-se observar, também, o consequente comportamento linear nos coeficientes de sensibilidade (Figs. 10 e 11).

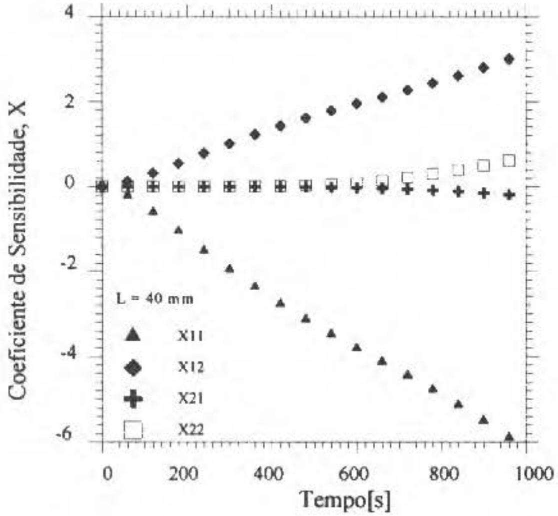

Fig. 7 Coeficientes de Sensibilidade - Amostra não Condutora, L = 40 mm.

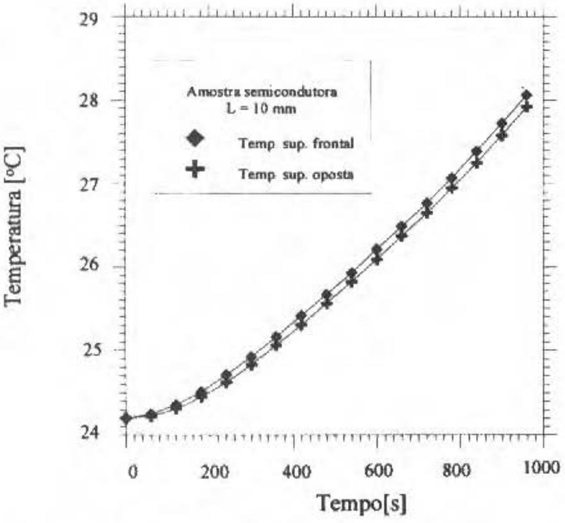

Fig. 8 Evolução da Temperatura nas Superfícies Frontal e Oposta ao Aquecimento - Amostra Semicondutora, L = 10 mm.

A solução de projeto para esses materiais passa por uma maior intensidade de fluxo de calor ou, alternativamente, uma menor espessura da amostra. A Tabela 3 apresenta as simulações para esses materiais com intensidades de fluxo de calor superiores a $200 W/m^2$.

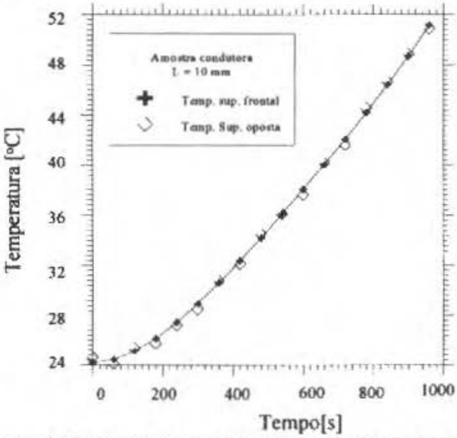

Fig. 9 Evolução da Temperatura nas Superfícies Frontal e Oposta ao Aquecimento.

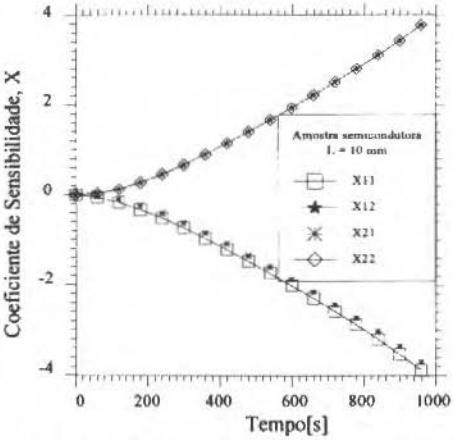

Fig. 10 Coeficientes de Sensibilidade, L = 10 mm.

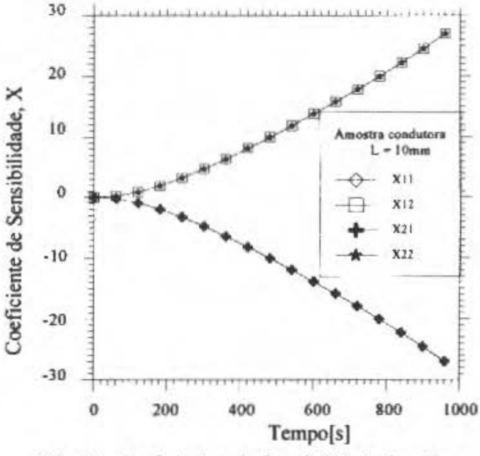

Fig. 11 Coeficientes de Sensibilidade, L = 10 mm.

Observando-se as Tabelas 1 e 2 nota-se que as melhores estimativas de λ e α são encontradas para os valores de $(q \times L)/\lambda$ situados entre 4 e 10. Ou seja, Teste 1 casos c e d, Teste 2 casos f, i, e j.

Tabela 3 Teste 2 - Materiais Condutores e não Condutores.

Valores Iniciais $\alpha = 1{,}0 \times 10^{-07} m^2/s$ $\lambda = 0{,}1 W/mK$

λ [W/mK]	α [m^2/s]	$(q \times L)/\lambda\,[K]$	ϕ_1(max) W/m^2	Erro [%] λ / α	Amostra	**Teste**
5,08	$16{,}26 \times 10^{-07}$	4,0	2.000,0	1,6 /1,62	Semi-cond.	f
Não convergiu	Não convergiu	40,0	20.000,0		Semi-cond.	g
91,65	$20{,}0 \times 10^{-05}$	0,285	2.000,0	30,9 / 25	Condutora	h
71,69	$16{,}38 \times 10^{-05}$	2,8	20.000,0	2,41/2,34	Condutora	i
70,8	$16{,}18 \times 10^{-05}$	5,60	40.000,0	1,14/1,12	Condutora	j

Esses resultados indicam que a espessura e a intensidade de fluxo de calor disponíveis são parâmetros extremamente importantes para um bom projeto de experimento e têm relação direta com o tipo de material estudado. Nesse ponto, uma questão ainda deve ser estudada: será a forma da evolução do aquecimento imposto na amostra, uma variável importante de projeto? Tal questão é investigada na próxima seção.

Forma Ideal do Fluxo de Calor Imposto

Uma vez que a intensidade de aquecimento da amostra, bem como a espessura e tipo de material foram analisados, optou-se, nessa seção por fixar-se esses parâmetros. Esse procedimento, entretanto, não compromete a generalidade da análise, quanto à influência da forma do fluxo de calor na estimação.

Assim, investigar-se-á a forma do fluxo de calor imposto numa amostra não condutora, com propriedades térmicas e características geométricas definidas como $\lambda = 0{,}4$ W/mK, $\alpha = 2{,}3\ 10^{-07}\ m^2/s$, espessura L = 50 mm e área 0.09 m^2.

Cumpre-se observar que, para o estudo das formas das evoluções dos fluxos de calor, foram estabelecidos limites para o tempo máximo de medição e intensidade máxima de aquecimento. Esses valores são aproximadamente de 2000 s e 200 W/m^2, respectivamente. Esses limites são fixados com o objetivo de se obter uma melhor comparação entre os resultados. Além disso, tempos superiores a 2000 s poderiam representar transientes muito longos e fluxos superiores acarretariam grandientes de temperatura excessivos, o que comprometeria a hipótese de propriedades térmicas constantes. A Fig. 12 apresenta as diversas formas de aquecimento em estudo.

Novamente, o êxito dos resultados obtidos é comparado segundo o critério de sucesso na estimação dos parâmetros. Assim, nesse caso, os parâmetros iniciais devem convergir aos parâmetros esperados ($\lambda = 0{,}4$ W/mK e $\alpha = 2{,}3\ 10^{-07}\ m^2/s$). Além disso, o número de iterações e a porcentagem de desvio entre as propriedades também devem ser analisadas.

Apresenta-se na Tabela 4 uma análise do tempo de exposição ao fluxo de calor em relação à estimação de λ e α, usando-se o fluxo imposto contínuo com evolução polinomial (Fig. 12, curva b). Observa-se que somente o uso de tempos de medição inferiores a 1000 s não garante a estimação dos parâmetros. Esses problemas se devem ao coeficientes de sensibilidade serem baixos e proporcionais.

Entretanto, como observado na Tabela 4, os parâmetros podem ser estimados na faixa de 1500 a 2000s ou usando-se toda região de medição. Nota-se contudo, que o erro percentual na difusividade térmica, assim como a variação de temperatura máxima não são ideais.

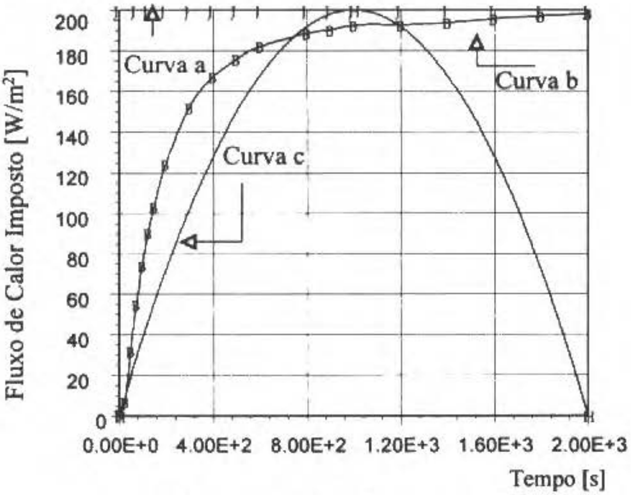

Fig. 12 Formas de Fluxo de Calor Imposto

Na busca de melhores resultados (menor erro e menor gradiente de temperatura), a forma de fluxo de calor tipo degrau (Fig. 12, curva a) é investigada. Nota-se, nesse caso, uma maior faixa de medição com melhores resultados no desvio percentual dos parâmetros estimados. Porém a curva de fluxo de calor do tipo constante é de difícil realização experimental. Observa-se que, devido às inércias térmicas da amostra e do elemento de aquecimento, as evoluções naturais do fluxo de calor, quando gerado por efeito Joule, adquirem a forma de evolução polinomial (Guimarães, 1993). Salienta-se ainda que o problema de gradientes térmicos excessivos, ($\Delta T > 10K$), não foi solucionado. Torna-se, assim, necessário o estudo de formas de imposição de aquecimento que permitam a estimação dos parâmetros, sem comprometer, contudo, os níveis de temperatura na amostra. A possibilidade de se usar aquecimento e desaquecimento surje então, naturalmente, como uma boa opção. Como já analisado anteriormente, a alternativa de diminuição da intensidade de fluxo de calor acarretaria menores coeficientes de sensibilidade e, consequentemente, insucesso da estimação.

Tabela 4 Estimação de Parâmetros para Fluxo de Calor Contínuo - Evolução Polinomial (5ª ordem) - *Curva b*

Valores Iniciais		$\alpha = 1,0 \times 10^{-07} m^2/s$		$\lambda = 0,1 W/mK$	
Tempo de Medição [s]	λ [W/mK]	Erro(λ) [%]	$\alpha \times 10^{07}$ [m^2/s]	Erro(α) [%]	ΔT máx [K]
0 - 300	0,27	32,5	0,99	56,9	-
300 - 1000	-	-	-	-	-
600 - 1000	-	-	-	-	-
1000 - 2000	0,27	32,5	1,01	52,2	-
1500 - 2000	0,39	2,5	2,14	7,0	11,56
0 - 2000	0,39	2,5	2,10	8,7	11,46

Investigou-se diferentes evoluções de fluxo de calor que poderiam ser obtidas a partir de procedimentos do tipo liga/desliga em um elemento de aquecimento baseado em efeito Joule. Todas as curvas simuladas foram construídas a partir dos limites extremos de tempo, que são indicados nas Tabelas 6 e 7. Inicialmente uma evolução parabólica perfeita foi simulada (curva tipo c). Posteriormente, buscando-se evoluções mais realistas que poderiam ser obtidas experimentalmente, simulou-se as curvas tipo c e e, mostradas nas Figs. 13 e 14.

Pode ser visto na Tabela 6 que as curvas do tipo c, da Fig. 12 apresentam ótimos resultados para a estimação de λ e α, uma vez que os desvios percentuais são inferiores à 3% (com excessão da faixa 0-800s). Também o gradiente máximo de temperatura na amostra situa-se entre os limites desejáveis (inferiores a 8,3 K). Todavia, essa curva é de difícil execução experimental. Nesse aspecto, as curvas apresentadas na Fig. 13 representam um avanço.

Tabela 5 Estimação de Parâmetros para Fluxo de Calor Constante (Fig. 1 - Curva a)

Valores Iniciais	$\alpha = 1{,}0 \times 10^{-07} m^2/s$		$\lambda = 0{,}05$ W/mK		
Tempo de Medição Usados na Estimação [s]	λ [W/mK]	Erro(λ) [%]	$\alpha \times 10^{07}$ [m^2/s]	Erro(α) [%]	ΔT máx na Amostra [K]
0 - 300	0,195	51,3	8,09	64,8	-
0 - 500	0,194	51,5	8,09	64,8	-
0 - 1000	0,213	46,8	0,91	60,6	-
0 - 1500	0,401	0,25	2,32	0,87	10,48
0 - 2000	0,401	0,25	2,31	0,44	12,08

Observa-se, nesse sentido, que as evoluções apresentadas pelas curvas tipo c e d tem características experimentais que podem ser obtidas ao se desligar o aquecimento e medir-se a evolução total do fluxo. Nesse caso, torna-se imprecindível o uso de trasdutores de fluxo de calor.

Tabela 6 Simulação da Estimação de Parâmetros para Fluxo de Calor, Evolução Polinomial (2ª ordem - Curva tipo c)

Valores Iniciais	$\alpha = 1{,}0 \times 10^{-07} m^2/s$		$\lambda = 0{,}05$W/m K		
Tempos Limites p/ Polin. 2ª Ordem. [s]	λ [W/mK]	Erro(λ) [%]	$\alpha \times 10^{07}$ [m^2/s]	Erro(α) [%]	ΔT máx [K]
0-800	0.378	5.50	2.06	10.4	3.3
0-1000	**0.395**	**1.25**	**2.24**	**2.61**	**4.9**
0-1500	0.401	0.25	2.302	0.09	7.13
0-2000	0.398	0.50	2.31	0.44	8.30

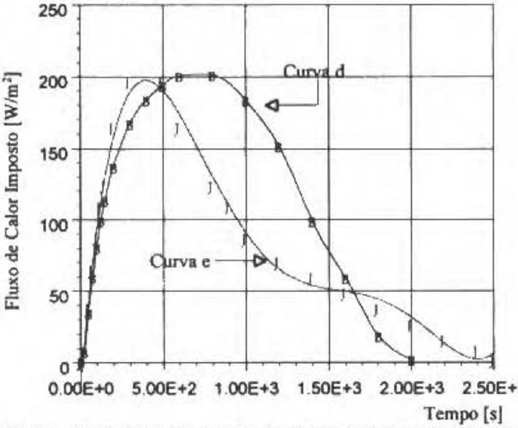

Fig. 13 Evolução Polinomial de Fluxo de Calor (liga/desliga)

Pode-se ainda, a partir dessas curvas, obter uma otimização dos tempos ideais de aquecimento, considerando-se os desvios percentuais de λ e α, e o limite de 6K para o gradiente de temperatura na amostra. A Tabela 7 apresenta essa análise.

Tabela 7 Simulação de Estimação de Parâmetros para Fluxo de Calor - Evolução Polinomial 5ª ordem. - Curvas tipo d e e

Valores Iniciais $\alpha = 1,0 \times 10^{-07}$ m²/s $\lambda = 0,1$W/m K

Tempos de Medição [s]	Tipo de Curva	λ [W/mK]	Erro(λ) [%]	$\alpha \times 10^{07}$ [m²/s]	Erro(α) [%]	ΔT máx [K]
0-2000	***d***	0,401	0,2	2,315	0,65	7,74
0-2500	***e***	0,401	0,2	2,312	0,52	5,71

As Figuras 14 e 15 apresentam os coeficientes de sensibilidade calculados a partir das curvas b (Fig. 12, faixa de 0 a 300 s) e e (Fig. 13, faixa de 0 a 2000 s). Pode-se assim, observar a dependência e a indepedência linear dos coeficientes, respectivamente, no pior caso (curva a - Tabela 4: 0 a 300s) e melhor (curva e - Tabela 6: 0 a 2500s).

Uma observação quanto ao uso de forma de fluxo de calor do tipo liga desliga é a conveniência de se trabalhar com baixos gradientes de temperatura na amostra. Isso só é possível quando se usa pelo menos dois sensores de temperatura (um em cada superfície). Dessa forma, enquanto a temperatura da face frontal cai, com o cessar do aquecimento, acarretando queda no coeficiente de sensibilidade, a temperatura da face oposta ainda sofre os efeitos do aquecimento, contribuindo com o seu aumento a uma boa informação (via coeficiente de sensibilidade) para a estimação de parâmetros. Isto pode ser visto nas Figs. 15 e 16 que mostram a evolução de temperatura para as superfícies frontal e oposta, com um fluxo de calor imposto do tipo liga/desliga (Curva e).

Observa-se ainda, a partir da Fig. 15, que o uso de tempos superiores a 2000 s no caso de imposição de fluxo de calor com desaquecimento pode ser interessante. Esse fato se deve ao aumento da temperatura na face oposta poder contribuir para uma boa estimação, enquanto a temperatura máxima ocorrida na amostra não se altera (ver Tabela 7 para tempos de medição de 0 a 2500 s). Todavia, observa-se da Fig. 15 que os valores dos coeficientes de sensibilidade relativos à face oposta tendem a diminuir seus valores, o que não representa contribuição à estimação. Isso indica que tempos superiores à 2500s não trariam nenhum ganho ao processo. Salienta-se ainda que 5 iterações foram necessárias na grande maioria das simulações. Esse número só aumentava nos casos de insucesso da estimativa dos parâmetros. Por essa razão o número de iterações não foi considerado na análise de otimização.

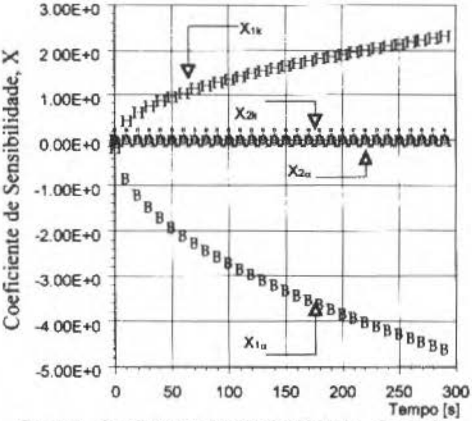

Fig. 14 Coeficientes de Sensibilidade - Curva b

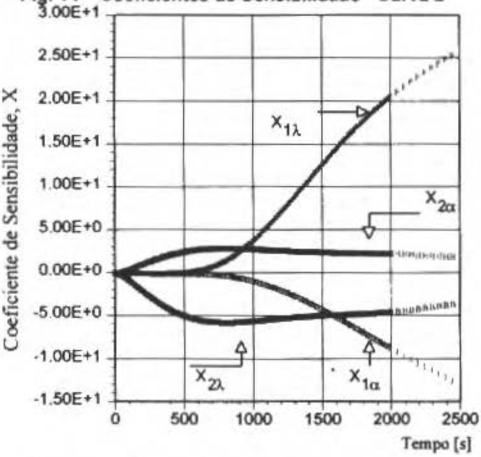

Fig. 15 Coeficientes de Sensibilidade - Curva e

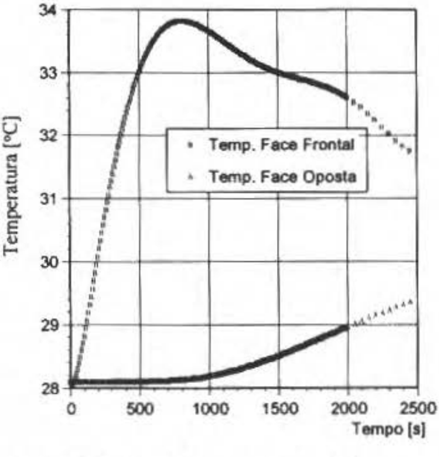

Fig. 16 Evolução de Temperatura nas Faces Frontal e Oposta - Curva e

Conclusões

Observa-se que a obtenção simultânea das propriedades térmicas λ e α através do método proposto é bastante sensível às variáveis de projeto ϕ_1, L e do tipo de material a ser investigado. Uma primeira investigação nos perfis de temperatura e fluxo de calor imposto é imprescindível para uma boa estimação desses parâmetros. O fluxo de calor imposto e a espessura da amostra, nesse caso, só devem ser definidos a partir de testes experimentais ou simulações numéricas desses experimentos.

Como foi observado, além da geometria e tipo de material a ser investigado, a forma do fluxo de calor imposto que estabelece o problema térmico é também extremamente importante. Se ainda se deseja estabelecer como limites uma boa precisão nos parâmetros a serem estimados (erros percentuais inferiores a 3%) e a representatividade das propriedades a uma determinada temperatura (variação de temperatura máxima na amostra inferior a 6 K) pode-se concluir que tipos de evolução como aquecimento e desaquecimento são as formas mais indicadas para a estimação simultânea de propriedades térmicas como a condutividade e difusividade térmica.

Agradecimentos

Os autores gostariam de agradecer o suporte financeiro prestado pela Agência Governamental CNPq (Proc.521212/93).

Referências

Artyukhin, E. A, Budnik, S. A. and Okhapkin, A. S, 1989, "Temperature-Measurement Optimization and Numerical Inverse Conduction-Treatment Solution", J. Engng Phys., Vol. 55, pp. 924-929.

Beck, J. V, 1969, "Determination of Optimum Transient Experiments for Thermal Contact Condutance", Int. J. Heat Mass Transfer, Vol. 12, pp.621-633.

Beck, J. V. and Blackwell, B, 1990., "Inverse problems", Handbook of Numerical Heat Transfer, pp 787-834

Blackwell, J. H., 1954, "A transient-flow Method for determination of thermal constants of insulating materials in bulk", Journal of Applied Physics, vol 25, pp. 137-144.

Guimarães, G., 1993, "Estimação da Condutividade e da Difusividade Térmica no Domínio da Frequência", Tese de Doutorado, Universidade Federal de Santa Catarina, Florianópolis, S.C, Brasil.

Guimarães, G e Philippi, P. C., 1994, " Uma Análise de Sensibilidade na Determinação de Propriedades Térmicas através da Técnica de Estimação de Parâmetros." Anais do V Encontro Nacional de Ciências Térmicas,. pp. 391-195.

Thaktak, R., Beck, J. V. and Sott, E. P., 1993, "Optimal Experiment Design for Estimating Thermal Properties of Composite Materials", Int. J. Heat Mass Transfer, Vol. 36, pp. 2977-2986.

Parker, W. J., Jenkins, R. J., Butler, C. P. and Abbott, G. L., 1961, "Flash method of determining thermal diffusivity, heat capacity and thermal conductivity", Journal of Applied Physics, 32, pp. 1679-1684.

Vigak, V. M., Kostenko, A. V. and Svirida, M. I., 1989, "Optimization of Two-Dimensional Nonsteady-State Temperature Regimes with Limitation Imposed on the Parameters of the Thermal Process", J. Engng. Phys., Vol. 56, pp. 463-467.

RBCM - J. of the Braz. Soc. Mechanical Sciences
Vol. XIX - No. 1 - 1997 - pp. 30-47

ISSN 0100-7386
Printed in Brazil

Vibration and Dynamic Instability Analysis of Turbomachinery Blades and Airfoils

Armando Miguel Awruch
Carlos Ferreira Ehlers
Universidade Federal do Rio Grande do Sul
Escola de Engenharia
Curso de Pós-Graduação em Eng. Civil
90035-190 Porto Alegre . RS Brasil

Abstract

Computational methods for determining natural frequencies and to study buckling and dynamic instability of turbomachinery blades and airfoils are presented here. A beam element with four degrees of freedom per node together with subspace interation method are used to calculate frequencies and vibration modes. Stability due to non conservative forces is analyzed using a beam element with six degrees of freedom per node and the QZ method is employed to compute eigenvalues.

Keywords: Turbomachinery Blades and Airfoils, Vibration Analysis, Dynamic Instability, Finite Elements.

Introduction

Three decades ago research envolving dynamic analysis of blades was carried out using analytical tools based on beam theory.

Recent advances in technology has led to more complex blade geometries and consequently it has become necessary to use modern numerical techniques to accomplish the corresponding structural analysis taking advantage of the simultaneous evolution in computer architecture.

Because of its versatility, the Finite Element Method (FEM) is a natural choice for carrying out the dynamic analysis and the structural design of turbomachinery blades and airfoils. Both shell theory and beam theory may be used to analyze such blades and airfoils (Leissa and Ewing, 1983). In spite of accuracy problems arising in the analysis of blades and airfoils having large aspect ratio, the thick beam model is adopted in this work because of its simplicity and because this model requires less degrees of freedom that would be the case if shell theory was employed.

The computation of natural frequencies is a fundamental stage in turbomachinery design in order to avoid resonance caused by excitation frequencies, such as electrical network frequencies, frequencies of rotation, etc. (Abbas, 1979; Kadarag, 1984.a; Kadarag, 1984.b; Subrahmayam and Kaza, 1985). Cracking due to fatigue may be also caused by vibrations.

In addition it is very important to analyze turbomachinery blades or airfoils operating under generalized non conservative loads (such as generalized follower and aerodynamic forces). For this case a beam model is employed here to study buckling loads due to generalized follower forces and to determine the flutter velocity due to aerodynamic forces. (See also Bendiksen and Friedmann, 1982; Chen and Chen, 1989; Chen and Ku, 1991; Sivanieri and Chopra, 1981).

Frequencies and Vibration Modes

Natural frequencies and vibration modes are obtained using a Timoshenko beam element with the following characteristics: (a) effects of rotation are taken into account (as natural frequencies of rotating blades are higher than natural frequencies of non rotating blades); (b) all geometric and natural boundary conditions are represented; (c) a flexible root at the blade-disc interface may be considered. The element is shown in Fig. 1.

Manuscript received: March 1996. Technical Editor: Agenor Toledo Fleury

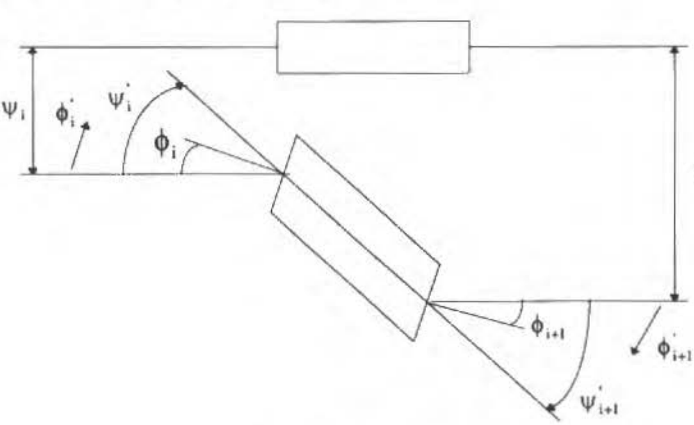

Fig. 1 Beam Element

The generalized dimensionless coordinates for each node are: the total deflection ψ, the total slope ψ', the bending slope ϕ and the first derivative of the bending slope ϕ'. Therefore, each element has four degrees of freedom per node.

The strain energy U and the kinetic energy T of the i-th rotating thick element of length 'l', as indicated in Figs. 2 and 3, are given by

$$U = \frac{1}{2}\frac{EI}{l}\int_0^1\left(\frac{d\phi}{d\eta}\right)^2 d\eta + \frac{1}{2}kAGl\int_0^1\left(\frac{d\psi}{d\eta}-\phi\right)^2 d\eta + \frac{1}{2}\rho A\Omega^2 l^3\cos^2\beta\int_0^1\psi^2 d\eta$$
$$+\frac{1}{2}\rho A\Omega^2 l^3\int_0^1\left\{[\delta+(i-1)+\eta_i]\left[\int_0^1\left(\frac{d\psi}{d\eta_1}\right)^2 d\eta_1+\ldots+\int_0^1\left(\frac{d\psi}{d\eta_i}\right)^2 d\eta_i\right]\right\}d\eta_i \tag{1}$$

Nomenclature

A = cross sectional area of the blade (m^2)
E = modulus of elasticity (N/ m^2)
G = modulus of rigidity (N/ m^2)
I = second moment of area of cross section (m^4)
I_x = mass moment of inertia per unit span about x-axis (Kgm^2/m)
J = geometric property of cross section (m^4)
L = length of blade (m)
RD = disc radius (m)
S$_x$ = mass moment per unit span about x-axis (Kgm^2/m)
T = kinetic energy (Nm)
U = strain energy (Nm)
V = fluid velocity (m/s)
b = semichord length of blade (m)
c = distance between aerodynamic center and elastic axis (m)
k = shear coefficient (dimensionless)
l = element length (m)
β = stagger angle (radians)
β_1 = translational flexibility (dimensionless)
β_2 = rotational flexibility (dimensionless)
δ = ratio of disc radius to length of blade (dimensionless)
η = dimensionless coordinate
θ = twist angle about x-axis (radians)
ρ = specific mass of the blade (Kg/m^3)
ρ_a =specific mass of the air (Kg/m^3)
ϕ = bending slope (dimensionless)
ψ = deflection (dimensionless)
ω = circular frequency (radians/s)
Ω = disc rotation (rpm)

$$T = \frac{1}{2}\rho A l^{3} \int_{0}^{1} \dot{\psi}^{2} d\eta + \frac{1}{2}\rho I l \int_{0}^{1} \dot{\phi}^{2} d\eta \qquad (2)$$

where ψ is the dimensionless total deflection, ϕ is the bending slope, β is the stagger angle, η is the dimensionless coordinate (x/l), ρ is the specific mass, Ω is the disc rotational speed, δ is RD/l (with RD being the disc radius), l is the element length, k is the shear coefficient, x is the longitudinal coordinate, E is the modulus of elasticity, G is the modulus of rigidity, A is the cross sectional area and I is the second moment of area of cross section.

The dots above the symbols ψ and ϕ in T indicate time derivatives.

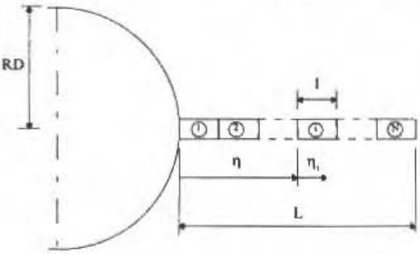

Fig. 2 Blade Element

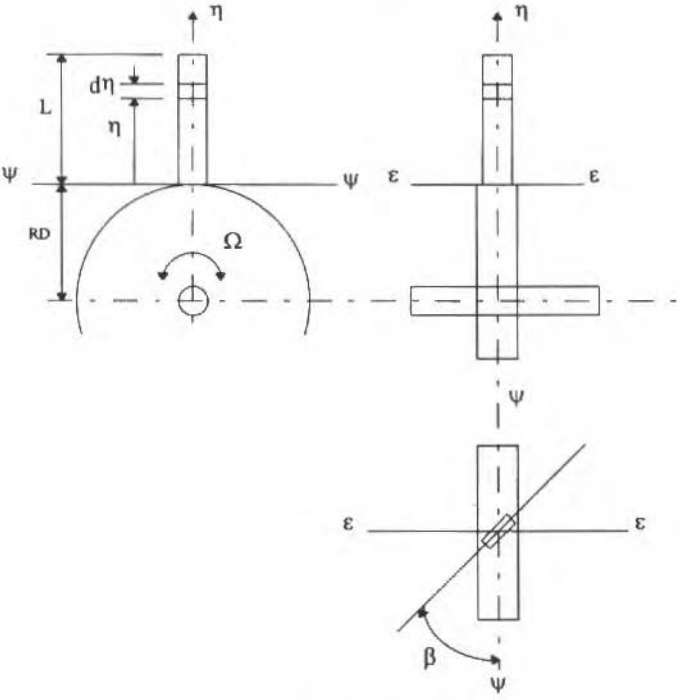

Fig. 3 Disc and Rotating Blade

Using cubic polynomial expansions ,ψ and ϕ may be written as follows:

$$\psi = \sum_{i=0}^{3} a_i \eta^i \quad ; \quad \phi = \sum_{i=0}^{3} b_i \eta^i \tag{3}$$

Substituting (3) into (1) and (2), and replacing a_i and b_i by the nodal coordinates, one obtains

$$U = \frac{1}{2}\frac{EI}{l}\{\zeta\}^T [K]\{\zeta\} \tag{4}$$

and

$$T = \frac{1}{2}\rho\frac{A}{l}\{\dot{\zeta}\}^T [M]\{\dot{\zeta}\} \tag{5}$$

where [K] and [M] are the symmetric stiffness and mass matrices respectively, and are given explicitly in Appendix I (see also Abbas,1979).

Vector $\{\zeta\}$ has the following components

$$\{\zeta\}^T = \{\psi_i, \phi_i, \psi'_i, \phi'_i, \psi_{i+1}, \phi_{i+1}, \psi'_{i+1}, \phi'_{i+1}\}$$

Applying the Lagrange principle, the dynamic equilibrium equation is given by

$$\frac{\partial U}{\partial \zeta} + \frac{d}{dt}\left(\frac{\partial T}{\partial \dot{\zeta}}\right) = \{Q\} \tag{6}$$

where {Q} is the vector of generalized forces corresponding to the vector of generalized displacements $\{\zeta\}$. Assuming harmonic motion with a cyclic frequency, and substituting U and T in (6) by (4) and (5) one obtains

$$\{[K] - \lambda [M]\}\{\zeta\} = \{0\} \tag{7}$$

where

$$\lambda = \frac{pAl^4}{EI} \tag{8}$$

is the element frequency parameter, $\{\zeta\}$ the vibration mode and 'p' the natural frequency.

Equation (7), after assembling and prescribing boundary conditions, is a classical eigenvalue problem and may be solved using a subspace iteration algorithm (Bathe, 1982).

At the top of the blade (free end) the bending moment and the shear force are zero, leading to the following boundary conditions:

$$\psi' = 0 \quad and \quad \psi' - \phi = 0 \tag{9}$$

At the bottom (disc-blade interface) the prescribed boundary conditions are

$$\psi = 0 \quad and \quad \phi = 0 \tag{10}$$

Equation (10) is applied in the case where the disc is very rigid with respect to the blade. For a flexible disc, the corresponding boundary conditions may be written as

$$\psi = \beta_1 \psi' - \beta_1 \beta_2 \phi' \tag{11}$$

$$\phi = \beta_2 \phi' \tag{12}$$

where

$$\beta_1 = \frac{kAG}{lk_2} \tag{13}$$

is the translational flexibility parameter (with k_1 being the translational stiffness) and

$$\beta_2 = \frac{EI}{lk_2} \tag{14}$$

is the rotational flexibility parameter (with k_2 being the rotational stiffness).

Values of k_2 may be found in McBrain and Genin (1973). It is not easy to find values for k_1 in the literature, but fortunately β_1 influences only higher modes.

When boundary conditions involve linear relations of different degrees of freedom, as is the case of Eqs. (11) and (12), the method of generalized restrictions may be used. In matrix form it can be expressed as follows:

$$[C_{dg}]\{U_g\} = [[C_{dn}]\ [C_{dd}]] \begin{Bmatrix} \{U_n\} \\ \{U_d\} \end{Bmatrix} = \{0\} \tag{15}$$

where $\{U_g\}$ has been partitionned in two vectors: $\{U_n\}$ containing 'n' independent degrees of freedom and $\{U_d\}$ containing 'd' dependent degrees of freedom.

Solving (15) for $\{U_d\}$, one obtains

$$\{U_d\} = [C_{dd}]^{-1}\,[C_{dn}]\,\{U_n\} = [G_{dn}]\,\{U_n\} \tag{16}$$

Defining the linear transformation

$$\{U_g\} = \begin{Bmatrix} \{U_n\} \\ \{U_d\} \end{Bmatrix} = \begin{bmatrix} [I_{nn}] \\ [G_{dn}] \end{bmatrix} \{U_n\} = [T_{gn}]\{U_n\} \tag{17}$$

where $[I_{nn}]$ is the identity matrix of order 'n', it is possible to define the stiffness matrix with respect to the 'n' non dependent degrees of freedom with

$$[K_{nn}] = [T_{gn}]^T [K_{gg}]\,[T_{gn}] = [[\overline{K}_{nn}] + [K_{nd}][G_{dn}] + [G_{dn}]^T [K_{nd}]^T [G_{dn}]^T [K_{nd}][G_{dn}]] \tag{18}$$

It may be observed that the stiffness matrix $[K_{gg}]$ (including dependent and non dependent degrees of freedom) was partitionned as

$$\begin{bmatrix} K_{gg} \end{bmatrix} = \begin{bmatrix} [\overline{K}_{nn}] & [K_{nd}] \\ [K_{nd}]^T & [K_{dd}] \end{bmatrix} \tag{19}$$

A similar reduction process may be used for the mass matrix.

Turbomachinery Blades and Airfoils Subject to non Conservative Loads

Stability analysis of elastic systems subject to non-conservative loads, such as follower and aerodynamic forces is very important in modern turbomachinery design. Several types of non-conservative stability problems for structural components are given in Bolotin (1963).

Forces are characterized as non-conservative when the work developed by them is path dependent and there is not any potential in such a way that its variation can be carried out in order to obtain the virtual work of the applied forces.

Non-conservative forces which are not explicitly dependent of time may be classified as either circulatory forces (or velocity independent) or dissipative forces (or velocity dependent). Aerodynamic forces are of the first kind, while follower forces are of the second kind.

When instability occurs such that an adjacent equilibrium configuration exists, a divergence or bifurcation problem is characterized. If on the other hand the instability occurs by oscillations with increasing amplitudes, the problem is one of dynamic instability or flutter.

Stability of non-conservative systems may be analysed numerically using either the transfer matrix or the finite element method. Although the first method requires less computer memory, the other one allows for the systematic formulation of more complex problems and produces more reliable results. A characteristic of non-conservative forces is that they lead to non self adjoint systems and consequently the finite element formulation lead to non-symmetric matrices.

The finite element used to analyze blades and airfoils under non-conservative forces are similar to that used in the previous section, but the twist angle and its derivative are added as new unknowns at each node.

The strain and the kinetic energy are given respectively by

$$U = equation\ (1) + \frac{1}{2}\frac{GJ}{l}\int_0^1 \left(\frac{d\theta}{d\eta}\right)^2 d\eta \tag{20}$$

$$T = equation\ (1) + S_x l^2 \int_0^1 \dot{\psi}\,\dot{\theta}\, d\eta + \frac{1}{2} I_x l \int_0^1 \dot{\theta}^2 d\eta \tag{21}$$

where J is the geometric property of cross section, S_x is the mass moment per unit span about x-axis, S_x is the mass moment of inertia per unit span about x-axis, θ is the twist angle about x-axis and x is the longitudinal axis.

The conservative work W^c and non-conservative work due to a follower moment M and uniform air velocity V, $\delta\ W_2^N$ and W_1^N, in a thick rotating blade element are given, respectively, by

$$W^c = M \int_0^1 \left(\frac{d^2\psi}{d\eta^2}\right) \theta\, d\eta \tag{22}$$

$$\delta\, W_2^N = M\theta(L)\delta\psi'(L) \tag{23}$$

$$W_1^N = l^2 \int_0^1 LF\psi\, d\eta + l \int_0^1 PM\theta\, d\eta \tag{24}$$

where LF is the lifting force and PM is the pitching moment.

LF and PM are given, for an incompressible fluid, by (Canergie, 1959)

$$LF = 2\pi\rho_a Vb(-l\dot{\psi} - V\theta) \tag{25}$$

$$PM = 2\pi\rho_a Vbc(l\dot{\psi} - V\theta) \tag{26}$$

where ρ_a is the air density, b is the semichord length of blade and c is the distance between aerodynamic center and elastic axis. Warping effects are not considered.

Employing cubic polynomial expansions for ψ, ϕ and θ in a similar form as in expression (3), and using Hamilton's principle, we get the following expression.

$$[M]\{\ddot{\zeta}\} - [N_1^N]\{\dot{\zeta}\} + [F]\{\zeta\} = \{0\} \tag{27}$$

with

$$[F] = [K] - [N^C] - [N_2^N] - [N_2^{N^*}] \tag{28}$$

and where [M], [K] are the symmetric mass and stiffness matrices respectively; $[N_2^N]$ and $[N_2^{N^*}]$ are the non symmetric matrices due to follower moment and aerodynamic forces respectively; $[N^C]$ is the symmetric geometric matrix due to conservative forces. All matrices are expressed explicitly in Appendix II (See also Chen and Chen, 1988).

The unknown vector $\{\xi\}$ has the following components for the i-th element with end nodes 'i' and (i+1):

$$\{\zeta\}^T = \{\psi_i, \phi_i, \theta_i, \psi'_i, \phi'_i, \theta'_i, \psi_{i+1}, \phi_{i+1}, \theta_{i+1}, \psi'_{i+1}, \phi'_{i+1}, \theta'_{i+1}\}$$

Equation (27) may also be written in a compact form as

$$[E]\{\dot{q}\} - [A]\{q\} = \{0\} \tag{29}$$

where

$$\{q\} = \begin{Bmatrix} \{\dot{\zeta}\} \\ \{\zeta\} \end{Bmatrix} ; \; [E] = \begin{bmatrix} -[N_1^N] & [M] \\ [M] & [0] \end{bmatrix} ; \; [A] = \begin{bmatrix} -[F] & [0] \\ [0] & [M] \end{bmatrix}$$

Taking $\{q\} = \overline{\{q\}}\, e^{\omega t}$ and replacing this expression in (29), one obtains

$$([A] - \omega [E])\, \overline{\{q\}} = \{0\} \tag{30}$$

Expression (30) is, after assembling and prescribing boundary conditions, an eigenvalue problem involving non-symmetric matrices. Boundary conditions are applied as in the previous section, but including for this case prescribed values for θ and θ'.

The QZ method (Moler and Stewart, 1973 and Ward, 1973) was used to solve (30). The computational procedure to solve the dynamic instability problem is shown in Fig. 4.

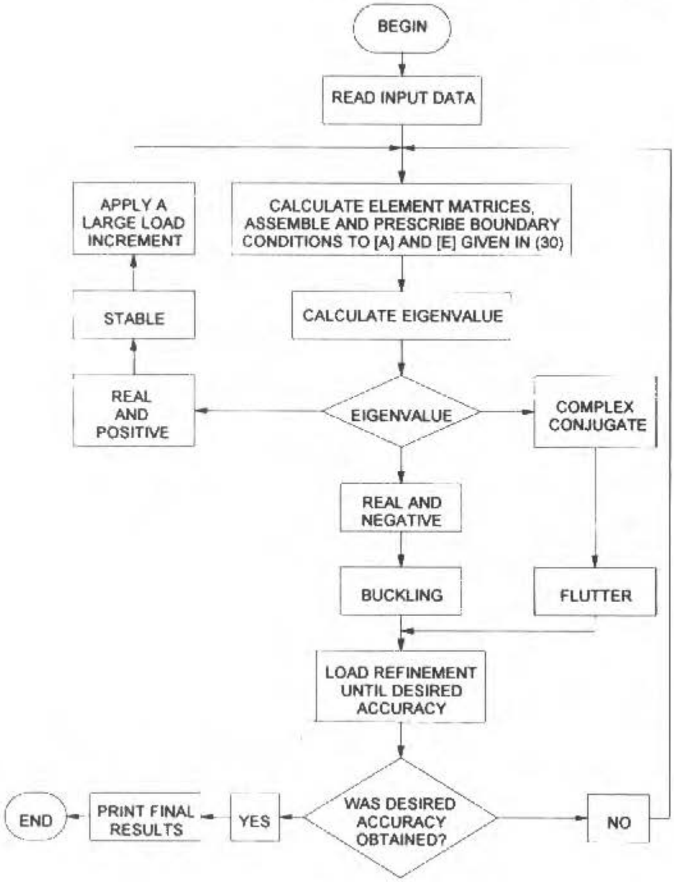

Fig. 4 Flowchart

Examples

Vibration of Rotating Blades

In Table 1, results for natural frequencies of a blade, with properties given below, are presented:

$L = 203.2\ mm$

$A = 232.272\ mm^2$

$I = 1002.28\ mm^4$

$J = 3523.2\ mm^4$

$\beta = 90^0$

$k = 0.8334$

$E = 2.0685 \times 10^{11}\ \mathrm{N/m^2}$

$G = 9.0252 \times 10^{10}\ \mathrm{N/m^2}$

$\rho = 7830\ \mathrm{kg/m^3}$

$RD = 152.4\ mm$

$\Omega = 3500\ rpm$

Table 1 Natural Frequencies

Number of Elements	Natural Frequencies (Hz)		
	Mode 1	Mode 2	Mode 3
1	172.45	-	-
2	175.70	951.44	-
3	171.31	943.37	2560.50
4	168.42	936.33	2547.74
5	166.45	932.83	2533.63
10	162.02	926.22	2521.31
15	160.38	923.93	2519.25

In Table 2, a comparative analysis with results obtained by Kadarag (1984) is given.

Table 2 Comparative Analysis

Number of Elements	Natural Frequencies (Hz)		
	Mode 1	Mode 2	Mode 3
Thin blade,7 elements (Kadarag, 1984.a)	170.17	928.31	2552.49
Thick blade, 7 elements (Kadarag, 1984.a)	169.97	922.35	2512.64
Experimental results	165.00	914.00	2475.00
Present model, 15 elements	160.38	923.93	2519.25

The influence on natural frequencies of rotation Ω, translational and rotational flexibility, including the combined effects of β_1 and β_2 are shown in Figs. 5 to 8.

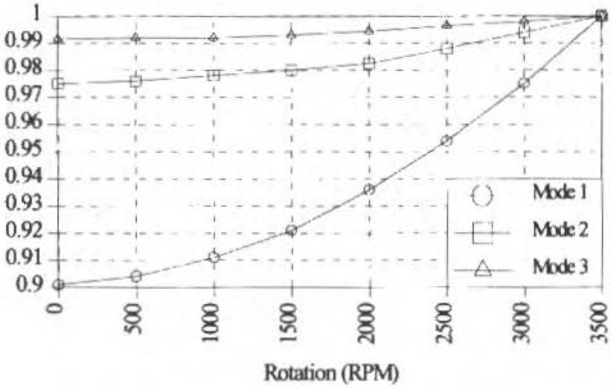

Fig. 5 Influence of Rotation on Natural Frequencies (Rotation×Natural Frequencies/Natural Frequencies with 3500 RPM)

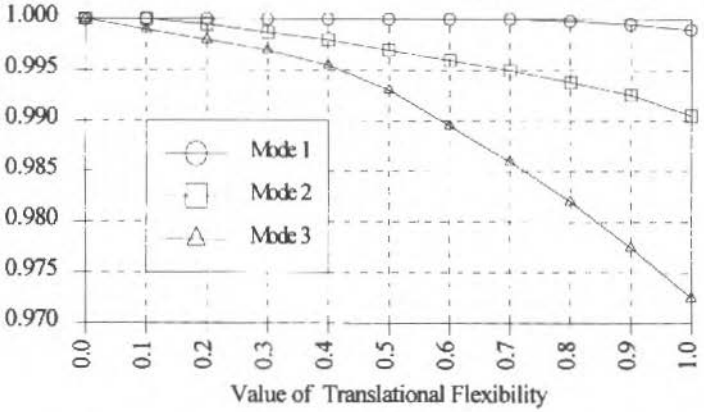

Fig. 6 Influence of Translational Flexibility on Natural Frequencies (β_1 × Natural Frequencies/Natural Frequencies for $\beta_1 = \beta_2 = 0$)

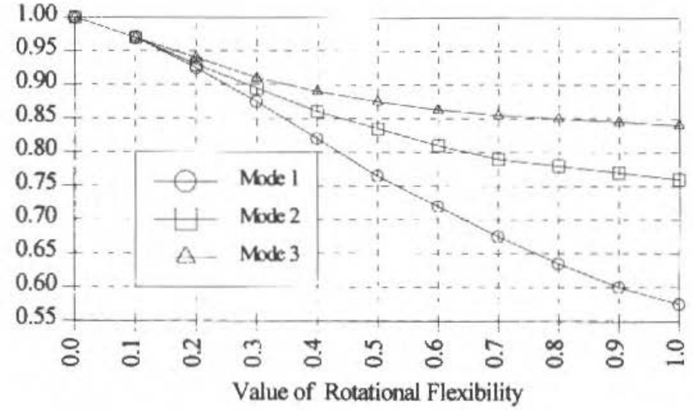

Fig. 7 Influence of Rotational Flexibility on Natural Frequencies (β_2 × Natural Frequencies/Natural Frequencies for $\beta_1 = \beta_2 = 0$)

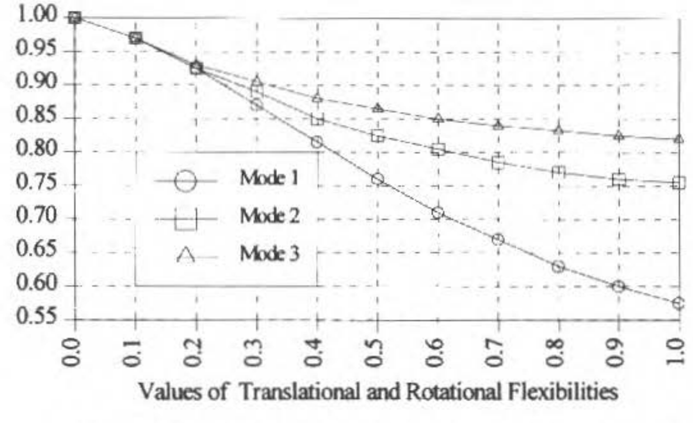

Fig. 8 Combined Effects of β_1 and β_2 on Natural Frequencies (β_1 and β_2 × Natural Frequencies/Natural Frequencies for a Clamped Beam, with $\beta_1 = \beta_2$)

From this example it can be concluded that: (a) rotation has an important influence on lower modes; (b) β_1 has more influence in higher modes; (c) β_2 influences mainly lower modes; (d) results are in good agreement with those obtained by Kadarag (1984, a).

Beam Subjected to a Follower Moment

A beam of 0.01m width and 0.1m height is subjected to a follower moment M. The properties are:

$k=1.2$ $\quad A = 1 \times 10^{-3} m^2$

$G = 9.025 \times 10^{10}\, \mathrm{N/m^2}$ $\quad I = 8.33 \times 10^{-7} m^4$

$E = 2.060 \times 10^{11}\, \mathrm{N/m^2}$ $\quad I_x = 6.59 \times 10^{-3} Kgm^2 / m$

$\rho = 7830\, Kg / m^3$ $\quad J = 3.12 \times 10^{-8} m^4$

Bolotin (1963) gives an exact solution for the critical moment

$$M_{cr} = 1.43\pi \sqrt{\frac{EIGJ}{L}}$$

which in this case is 32994 Nm.

In Table 3 results for different meshes are shown together with the relative computer times.

Table 3 Results for a Beam Subject to a Follower Moment.

Number of Elements	Follower Moment	Comparisons of Computer Process Time For Each Iteration
2	38970	1.0
3	37610	3.0
4	37060	6.5
5	36780	12.0
6	36610	20.0
7	36500	32.5
8	36410	45.0

Comparisons of computer process time in Table 3 were made taking as reference the case in which two elements were used.

It can be seen that reasonable results were obtained.

Flutter Velocity Analysis for an Airfoil

The airfoil of the airplane "Spirit of St. Louis" used by Charles Lindbergh to cross the Atlantic Ocean is taken as an example. The airfoil properties are (Belvins, 1990):

$k = 0.85$ $L = 6.4\ m$ $J = 1.5 \times 10^{-5} m^4$

$G = 3.7 \times 10^9\ \mathrm{N/m^2}$ $\beta = 0°$ $\rho_a = 1.2\ \mathrm{Kg/m^3}$

$E = 9.6 \times 10^9\ \mathrm{N/m^2}$ $A = 0.4398\ m^2$ $b = 1.65\ m$

$\rho = 22.96\ \mathrm{Kg/m^3}$ $I = 0.0301 m^4$ $c = 0.254\ m$

$RD = 0\ m$ $I_x = 4.52\ \mathrm{Kgm^2/m}$

$\Omega = 0\ rpm$ $S_x = 2.09\ \mathrm{Kgm/m}$

In the Table 4 results for a flutter velocity and the relative CPU time for each iteration are shown.

The result given by Belvins (1990) for the flutter velocity is 19 m/s, that is close to the values obtained here. Differences may be caused by approximate calculations of some properties that were not specified in Belvin's book.

Table 4 Flutter Velocity Calculations for an Airfoil

Nº of Elements	Flutter Velocity (m/s)	Comparisons of Computer Process, Time for Each Iteration
2	18.0	1.00
3	17.9	2.92
4	17.9	6.17
5	17.9	11.83

Comparisons of computer process time in Table 3 were made taking as reference the case in which two elements were used.

Conclusions

Promissing results were obtained for frequencies and modes of rotating blades. The same may be concluded with respect to the analysis of beams and airfoils subjected to non conservative loads, but more work is necessary. More sophysticated models and the presence of cracks and warping could be studied.

The model such as presented in this paper requires some improvements in the eigenvalue subroutine for dynamic instability analysis, and the large amount of input data required to analyze stability problems may be a source of errors. In spite of these drawbacks, a practical and simple method to analyze vibration and problems envolving dynamic instability of turbomachinery blades and airfoils was implemented.

References

Abbas, B.A.H., 1979. "Dynamic Analysis of Thick Rotating Blades with Flexible Roots". Aeronautical Journal, V. 83, pp. 450-453.

Bathe, K-J, 1982. "Finite Element Procedures in Engineering Analysis". Prentice Hall, NJ, USA.

Bendiksen, O.O. and Friedmann, P.P., 1982. "The Effect of Bending-Torsion Coupling on Fan and Compressor Blade Flutter", Journal of Engng. For Power, , V.104, pp. 617-623.

Belvins; R.D., 1990. "Flow Induced Vibrations". Van Nostrand Reinhold, 2nd Ed., NY, USA.

Bolotin, V.V., 1963. "Non Conservative Problems of the Theory of Elastic Stability". Pergamon Press, NY, USA.

Carnegie,W., 1959. "Vibration of Rotating Cantilever Blading : Theoretical Approaches to the Frequency Problem Based in Energy Methods". Journal of Mech. Eng. Science, V. 1, N.3, pp. 235-240.

Chen, L.W. and Chen, C.L., 1988. "Vibration and Stability of Thick Rotating Blades". Comp. and Structures, V. 35, N.1, pp. 67-74.

Chen, L.W. and Ku, D.M., 1991. "Stability Analysis of a Timoshenko Beam Subjected to Distributed Follower Forces Using Finite Elements", Comp. and Structures, V.41, N.4, pp. 813-819.

Kadarag, V., 1984. "Dynamical Analysis of Practical Blades with Shear Center Effects". Journal of Sound and Vibration, V.92, N.4, pp. 471-490.

Kadarag, V., 1984. "Finite Element Dynamic Analysis of Blades Shear Center Effects on Practical Blade Discs". Journal of Sound and Vibration, V.94, N.2, pp. 183-197.

Leissa, A.W. and Ewing M.S., 1983. "Comparison of Beam and Shell Theories for the Vibration of Thin Turbomachinery Blades". Journal of Eng. for Power, V. 105, pp. 383-392.

Mc Bain, J.C. and Genin,J., 1973. "Natural Frequencies of a Beam Considering Support Characteristics". Journal of Sound and Vibration, V. 27, N.2, pp. 197-206.

Moler, C.B. and Stewart, G.W., 1973. An Algorithm for Generalized Matrix Eigenvalue Problem". Siam Journal Num. Anal., V. 10, pp. 241-256.

Sivaneri, N.T. and Chapra, I. 1981. "Dynamic Stability of a Rotor Blade Using Finite Element Analysis". AIAA Journal, V.20, N.3, pp. 716-723.

Subrahamanyam, K.B. and Kaza, K.R.V., 1985. "Vibration Analysis of Rotating Turbomachinery Blades by an Improved Finite Difference Method". Int. J. for Num. Meth. in Engng., V.21, pp. 1871-1886.

Ward, R.C., 1973. "An Extension of the QZ Algorithm for Solving the Generalized Matrix Eigenvalue Problem". Technical Note. NASA TN D-7305.

Appendix I

Mass and stiffness matrices to determine natural frequencies and vibration modes of thick rotating blades.

$$[M]=\frac{1}{420}\begin{bmatrix} 156 & 0 & 22 & 0 & 54 & 0 & -13 & 0 \\ & 156R & 0 & 22R & 0 & 54R & 0 & -13R \\ & & 4 & 0 & 13 & 0 & -3 & 0 \\ & & & 4R & 0 & 13R & 0 & -3R \\ & & & & 156 & 0 & -22 & 0 \\ & & & & & 156R & 0 & -22R \\ & & & & & & 4 & 0 \\ & & & & & & & 4R \end{bmatrix}$$

$$[K]=\frac{1}{420}\begin{bmatrix} K(1,1) & 210S & K(1,3) & 42S & K(1,5) & 210S & K(1,7) & -42S \\ & 156S+504 & -42S & 22S+42 & -210S & 54S+504 & 42S & -13S+42 \\ & & K(3,3) & 0 & K(3,5) & 42S & K(3,7) & -7S \\ & & & 4S+56 & -42S & 13S-42 & 7S & -3S-14 \\ & & & & K(5,5) & -210S & K(5,7) & 42S \\ & & & & & 156S+504 & -42S & -22S-42 \\ & & & & & & K(7,7) & 0 \\ & & & & & & & 4S+56 \end{bmatrix}$$

$$K(1,1) = 504S + 180S1 - 156S2 + 252S3 + 504S4$$

$$K(1,3) = 42S + 6S1 - 22S2 + 0S3 + 42S4$$

$$K(1,5) = -504S - 180S1 - 54S2 - 252S3 - 504S4$$

$$K(1,7) = 42S + 27S1 + 13S2 + 43S3 + 42S4$$

$$K(3,3) = 56S + 24S1 - 4S2 + 42S3 + 56S4$$

$$K(3,5) = -42S - 6S1 - 13S2 + 0S3 - 42S4$$

$$K(3,7) = -14S - 4S1 + 3S2 - 7S3 - 14S4$$

$$K(5,5) = 504S + 180S1 - 156S2 + 256S3 + 504S4$$

$$K(5,7) = -42S - 27S1 + 22S2 - 42S3 - 42S4$$

$$K(7,7) = 56S + 10S1 - 4S2 + 14S3 + 56S4$$

where

$$R = \frac{I}{Al^2} \;;\; S = \frac{kAGl^2}{EI} \;;\; S1 = \left(\frac{\rho A l^4}{EI}\right)\Omega^2 \;;\; S2 = S1\cos^2\beta$$

$$S3 = S1[\delta + (i-1)] \;;\; S4 = \sum_{K=1}^{i-1} S1[\delta + (i-1) + 1/2] \;;\; \delta = RD/l$$

Remark: [M] and [K] are symmetric matrices.

Appendix II

Matrices for stability problem of blades subjected to non-conservative loads.

$$[M] = \frac{1}{420} \times \begin{bmatrix}
156 & 0 & -156R1 & 22 & 0 & -22R1 & 54 & 0 & -54R1 & -13 & 0 & 13R1 \\
 & 156R & 0 & 0 & 22R & 0 & 0 & 54R & 0 & 0 & -13R & 0 \\
 & & 156R2 & -22R1 & 0 & 22R2 & -54R1 & 0 & 54R2 & 13R1 & 0 & -13R2 \\
 & & & 4 & 0 & -4R1 & 13 & 0 & -13R1 & -3 & 0 & 3R1 \\
 & & & & 4R & 0 & 0 & 13R & 0 & 0 & -3R & 0 \\
 & & & & & 4R2 & -13R1 & 0 & 13R2 & 3R1 & 0 & -3R2 \\
 & & & & & & 156 & 0 & -156R1 & -22 & 0 & 22R1 \\
 & & & & & & & 156R & 0 & 0 & -22R & 0 \\
 & & & & & & & & 156R2 & 22R1 & 0 & -22R2 \\
 & & & & & & & & & 4 & 0 & -4R1 \\
 & & & & & & & & & & 4R & 0 \\
 & & & & & & & & & & & 4R2
\end{bmatrix}$$

$$[K]=\frac{Sr}{420}\times\begin{bmatrix} K(1,1) & 210S & 0 & K(1,4) & 42S & 0 & K(1,7) & 210S & 0 & K(1,10) & -42S & 0 \\ & 156S+504 & 0 & -42S & 22S+42 & 0 & -210S & 54S-504 & 0 & 42S & -13S+42 & 0 \\ & & 504S5 & 0 & 0 & 42S5 & 0 & 0 & -504S5 & 0 & 0 & 42S5 \\ & & & K(4,4) & 0 & 0 & K(4,7) & 42S & 0 & K(4,10) & -7S & 0 \\ & & & & 4S+56 & 0 & -42S & 13S-42 & 0 & 7S & -3S-14 & 0 \\ & & & & & 56S5 & 0 & 0 & -42S5 & 0 & 0 & -14S5 \\ & & & & & & K(7,7) & -210S & 0 & K(7,10) & 42S & 0 \\ & & & & & & & 156S+504 & 0 & -42S & -22S-42 & 0 \\ & & & & & & & & 504S5 & 0 & 0 & -42S5 \\ & & & & & & & & & K(10,10) & 0 & 0 \\ & & & & & & & & & & 4S+56 & 0 \\ & & & & & & & & & & & 56S5 \end{bmatrix}$$

$$\left[N^C\right]=\frac{1}{420}\begin{bmatrix} 0 & 0 & -504W1 & 0 & 0 & -42W1 & 0 & 0 & 504W1 & 0 & 0 & -42W1 \\ & 0 & 0 & 0 & 0 & 0 & 0 & 0 & 0 & 0 & 0 & 0 \\ & & 0 & -462W1 & 0 & 0 & 504W1 & 0 & 0 & -42W1 & 0 & 0 \\ & & & 0 & 0 & -56W1 & 0 & 0 & 42W1 & 0 & 0 & 14W1 \\ & & & & 0 & 0 & 0 & 0 & 0 & 0 & 0 & 0 \\ & & & & & 0 & 42W1 & 0 & 0 & 14W1 & 0 & 0 \\ & & & & & & 0 & 0 & -540W1 & 0 & 0 & 42W1 \\ & & & & & & & 0 & 0 & 0 & 0 & 0 \\ & & & & & & & & 0 & 462W1 & 0 & 0 \\ & & & & & & & & & 0 & 0 & -56W1 \\ & & & & & & & & & & 0 & 0 \\ & & & & & & & & & & & 0 \end{bmatrix}$$

Remark: $[M]$, $[K]$ and $[N^c]$ are symmetric matrices.

$$\left[N_1^N\right]=\begin{bmatrix} -156W2 & 0 & 0 & -22W2 & 0 & 0 & -54W2 & 0 & 0 & 13W2 & 0 & 0 \\ 0 & 0 & 0 & 0 & 0 & 0 & 0 & 0 & 0 & 0 & 0 & 0 \\ 156W3 & 0 & 0 & 22W3 & 0 & 0 & 54W3 & 0 & 0 & -13W3 & 0 & 0 \\ -22W2 & 0 & 0 & -4W2 & 0 & 0 & -13W2 & 0 & 0 & 3W2 & 0 & 0 \\ 0 & 0 & 0 & 0 & 0 & 0 & 0 & 0 & 0 & 0 & 0 & 0 \\ 22W3 & 0 & 0 & 4W3 & 0 & 0 & 13W3 & 0 & 0 & -3W3 & 0 & 0 \\ -54W2 & 0 & 0 & -13W2 & 0 & 0 & -156W2 & 0 & 0 & 22W2 & 0 & 0 \\ 0 & 0 & 0 & 0 & 0 & 0 & 0 & 0 & 0 & 0 & 0 & 0 \\ 54W3 & 0 & 0 & 13W3 & 0 & 0 & 156W3 & 0 & 0 & -22W3 & 0 & 0 \\ 13W2 & 0 & 0 & 3W2 & 0 & 0 & 22W2 & 0 & 0 & -4W2 & 0 & 0 \\ 0 & 0 & 0 & 0 & 0 & 0 & 0 & 0 & 0 & 0 & 0 & 0 \\ -13W3 & 0 & 0 & -3W3 & 0 & 0 & -22W3 & 0 & 0 & 4W3 & 0 & 0 \end{bmatrix}$$

$$\left[N_2^N\right]=\frac{1}{420}\begin{bmatrix} \ldots & \ldots & & & \theta(L) & \psi'(L) & \phi'(L) & \theta'(L) \\ 0 & \ldots & \ldots & \ldots & 0 & 0 & 0 & 0 \\ \ldots & \ldots & & & & & & \\ \ldots & \ldots & & & & & & \\ \ldots & \ldots & & & 0 & \ldots & \ldots & \ldots \\ \ldots & \ldots & & & 0 & 0 & 0 & 0 \\ \ldots & \ldots & & & 420W1 & 0 & 0 & 0 \\ \ldots & \ldots & & & 0 & 0 & 0 & 0 \\ 0 & \ldots & \ldots & \ldots & 0 & 0 & 0 & 0 \end{bmatrix}$$

$$\left[N_2^{N^*}\right]=\begin{bmatrix}
0 & 0 & 156W4 & 0 & 0 & 22W4 & 0 & 0 & 54W4 & 0 & 0 & -13W4 \\
0 & 0 & 0 & 0 & 0 & 0 & 0 & 0 & 0 & 0 & 0 & 0 \\
0 & 0 & -156W5 & 0 & 0 & -22W5 & 0 & 0 & -54W5 & 0 & 0 & 13W5 \\
0 & 0 & 22W4 & 0 & 0 & 4W4 & 0 & 0 & 13W4 & 0 & 0 & -3W4 \\
0 & 0 & 0 & 0 & 0 & 0 & 0 & 0 & 0 & 0 & 0 & 0 \\
0 & 0 & -22W5 & 0 & 0 & -4W5 & 0 & 0 & -13W5 & 0 & 0 & 3W5 \\
0 & 0 & 54W4 & 0 & 0 & 13W4 & 0 & 0 & 156W4 & 0 & 0 & -22W4 \\
0 & 0 & 0 & 0 & 0 & 0 & 0 & 0 & 0 & 0 & 0 & 0 \\
0 & 0 & -54W5 & 0 & 0 & -13W5 & 0 & 0 & -156W5 & 0 & 0 & 22W5 \\
0 & 0 & -13W4 & 0 & 0 & -3W4 & 0 & 0 & -22W4 & 0 & 0 & 4W4 \\
0 & 0 & 0 & 0 & 0 & 0 & 0 & 0 & 0 & 0 & 0 & 0 \\
0 & 0 & 13W5 & 0 & 0 & 3W5 & 0 & 0 & 22W5 & 0 & 0 & -4W5
\end{bmatrix}$$

where

$$K(1,1) = 504S - 72S1 - 156S2 - 252S3 + 504S4$$

$$K(1,4) = 42S - 15S1 - 22S2 - 43S3 + 42S4$$

$$K(1,7) = -504S + 72S1 - 54S2 + 252S3 - 504S4$$

$$K(1,10) = 42S + 6S1 + 13S2 + 0S3 + 42S4$$

$$K(4,4) = 56S - 4S1 - 4S2 - 14S3 + 56S4$$

$$K(4,7) = -42S + 15S1 - 13S2 + 42S3 - 42S4$$

$$K(4,10) = -14S + 3S1 + 3S2 + 7S3 - 14S4$$

$$K(7,7) = 504S - 72S1 - 156S2 - 252S3 + 504S4$$

$$K(7,10) = -42S - 6S1 + 22S2 + 0S3 + 504S4$$

$$K(10,10) = 56S - 18S1 - 4S2 - 42S3 + 56S4$$

$S = kAGl^2 / EI$; $R = I / Al^2$;

$S1 = \left(\frac{\rho A l^4}{EI}\right) \Omega^2$; $R1 = Sx / \rho Al$;

$S2 = S1 \cos^2 \beta$; $R2 = Ix / \rho Al^4$;

$S3 = S1[\delta + (i-1)]$; $W1 = M / \rho Al^3$;

$$S3 = S1[\delta + (i-1)] ; \qquad W1 = M / \rho A l^3 ;$$

$$S4 = \sum_{K=1}^{i-1} S1[\delta + (i-1) + 1/2] ; \qquad W2 = 2\pi \rho_a b V / \rho A ;$$

$$S5 = GJ / EI ; \qquad W3 = 2\pi \rho_a b c V / \rho A l ;$$

$$Sr = EI / \rho A l^4 ; \qquad W4 = 2\pi \rho_a b V^2 / \rho A l ;$$

$$\delta = \frac{RD}{l} ; \qquad W5 = 2\pi \rho_a b c V^2 / \rho A l^2 .$$

RBCM - J. of the Braz. Soc. Mechanical Sciences
Vol. XIX - No.1 - 1997 - pp. 48-57

ISSN 0100-7386
Printed in Brazil

Análise Plástica da Flexão-Torção em Peças de Hastes de Paredes Delgadas com Seção Aberta

Plastic Analysis of Bending-Torsion of Thin-Walled Beams

Emil de Souza Sánchez Filho
Universidade Federal de Juiz de Fora
Faculdade de Engenharia
Departamento de Estruturas
36036-330 Juiz de Fora, MG Brasil

Abstract

This paper presents the basic expressions of the Plasticity Theory which allow the formulation of the bending-torsion in the plastic regime for which the equilibrium equations are deduced, showing the change of position of the shear center in the plastic section. The combined forces in the section are also presented.
Keywords: Plastic Analysis, Bending-Torsion, Thin-Walled Beams.

Resumo

Este trabalho apresenta as expressões básicas da Teoria da Plasticidade que permitem a formulação da flexo-torção em regime plástico, para o qual são deduzidas as equações de equilíbrio, mostrando-se a variação da posição do centro de cisalhamento da seção plastificada. A interação entre esforços seccionais é apresentada resumidamente.
Palavras-chave: Análise Plástica, Flexo-Torção, Peças de Hastes de Paredes Delgadas.

Introdução

O estudo da torção de Saint-Venant em peças lineares de material homogêneo em regime plástico, faz-se através da analogia do monte de areia devida à Nadai. Porém, quando da flexo-torção de peças em hastes de paredes delgadas (torção de Vlassov), tem-se o empenamento da seção e o surgimento de tensões normais à seção transversal, originadas pelo Bimomento. Em regime plástico — deve-se atender à uma lei de plastificação e à lei de fluência plástica -, esse esforço modifica substancialmente o comportamento mecânico da peça, variando a posição do centro de cisalhamento da seção.

A função sinal de Prager é o artifício matemático usado para desacoplar os vários esforços seccionais na análise plástica da flexo-torção, permitindo obter funções de interação entre esses parâmetros, tornando viável, a nível de dimensionamento, a elaboração de gráficos e tabelas, o que foge ao escopo deste trabalho.

Conceitos da Teoria da Plasticidade

Para um tensor de tensões genérico σ_{ij}, tem-se que as componentes do vetor de tensões numa faceta qualquer num ponto arbitrário do corpo se escreve:

$$T_i = \sigma_{ij} n_j \quad ; \quad i,j = 1,2,3 \tag{1}$$

Manuscript received: July 1994. Technical Editor: Agenor de Toledo Fleury. Presented at XXVII Jornadas Sudamericanas de Ingenieria Civil , San Miguel de Tucuman, Argentina, 1995.

onde n_j é o vetor normal à faceta e T_i a componente do vetor de tensões, que pode ser decomposto em duas componentes, uma segundo a normal à faceta, outra tangente à esta.

Os eixos principais de tensões são obtidos através de:

$$(\sigma_{ij} - \sigma\delta_{ij})\, n_j = 0 \tag{2}$$

sendo σ a tensão principal e δ_{ij} o delta de Kronecker.

Resolvendo-se esse sistema de equações obtém-se os três invariantes do tensor, dados por:

$$I_1 = \sigma_{ii} \tag{3}$$

$$I_2 = \frac{1}{2}\,(\sigma_{ii}^2 - \sigma_{ij}\sigma_{ji}) \tag{4}$$

$$I_3 = \frac{1}{6}\,(2\sigma_{ij}\sigma_{jk}\sigma_{ki} - 3\sigma_{ii}\sigma_{ij}\sigma_{ji} + \sigma_{ii}^3) \tag{5}$$

Definindo-se o tensor hidrostático — produz a mudança de volume do corpo — como:

$$\sigma_m = \frac{1}{3}\,\sigma_{ii} \tag{6}$$

determina-se o tensor desviador — responsável pela variação de forma do corpo — através de

$$s_{ij} = \sigma_{ij} - \sigma_m\delta_{ij} \tag{7}$$

Seguindo linha de análise análoga à utilizada para o cálculo das tensões principais, tem-se a equação característica do tensor desviador (estado de cisalhamento puro):

$$s^3 - J_1 s^2 - J_2 s - J_3 = 0 \tag{8}$$

com os coeficientes denominados invariantes do tensor desviador, dados por

$$J_1 = s_{ii} = 0 \tag{9}$$

$$J_2 = \frac{1}{2}\, s_{ij}s_{ji} \tag{10}$$

$$J_3 = \frac{1}{3}\, s_{ij}s_{jk}s_{ki} \tag{11}$$

Dentre os vários critérios de plastificação, o critério de Huber-von Mises-Hencky é, em geral, adotado quando do estudo de materiais dúcteis. Através de considerações puramente teóricas, pode-se supor que a plastificação ocorra quando J_2 atinja um valor crítico, o que implica que a energia elástica de distorção chegue a um certo valor limite na plastificação, o que pode ser expresso em função do tensor desviador:

$$s_{ij}s_{ji} = 2k^2 \tag{12}$$

ou em função do estado de tensões

$$(\sigma_x - \sigma_y)^2 + (\sigma_y - \sigma_z)^2 + (\sigma_z - \sigma_x)^2 + 6\tau_{xy}^2 + 6\tau_{yz}^2 + 6\tau_{zx}^2 = 2f_y^2 \tag{13}$$

onde $f_y = \sqrt{3}\ k$ é a tensão de plastificação em ensaio uniaxial.

A regra da normalidade ou lei de fluência plástica, em sua forma genérica escreve-se

$$\dot{\epsilon}_{ij} = \dot{\lambda}_k \frac{\partial F_k(\sigma_{ij})}{\partial \sigma_{ij}} \ ; \ \dot{\lambda}_k \geq 0 \tag{14}$$

com a lei de plastificação $F_k(\sigma_{ij})$ assumindo diversas funções, dependendo do tensor de tensões e com o escalar λ_k definido para cada caso específico de σ_{ij}; se $F_k(\sigma_{ij}) < 0$, regime elástico, tem-se $\lambda_k = 0$; $\lambda_k > 0$ se $F_k(\sigma_{ij}) = 0$, ou seja, a plastificação é atingida.

O estado de tensão uniaxial de um corpo pode ser estudado em regime rígido-plástico perfeito, utilizando-se o conceito de função SINAL(x) idealizado por Prager. Essa função, um operador de posição, não pode ser expandida, isto é, não é integrável e derivável, visa somente delimitar o estágio de solicitação a que está submetido o corpo, ou em conjunto com outras funções facilitar análises mais complexas. Define-se função SINAL(x) como a função que possui as seguintes características:

SINAL(x) = 1 quando $x > 0$

SINAL(x) = -1 quando $x < 0$

$-1 \leq$ SINAL(x) ≤ 1 quando $x = 0$

A Figura 1 ilustra a função SINAL(x) em relação aos valores algébricos assumidos por seu argumento.

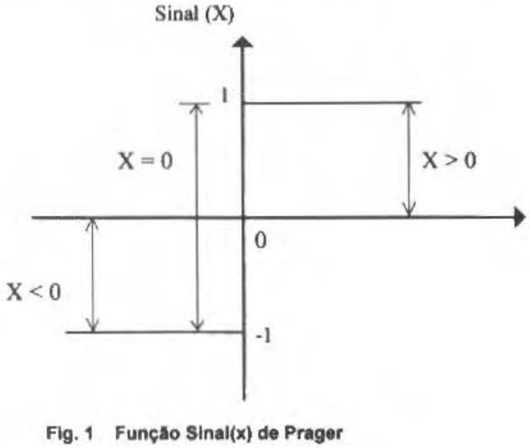

Fig. 1 Função Sinal(x) de Prager

Equações de Equilíbrio

Adotando-se a terminologia empregada por Flügge (1973), denomina-se ação ativa a que produz trabalho interno ponderável e ação reativa a estritamente necessária ao equilíbrio, relacionadas através das equações:

$$\frac{dN}{dx} = 0 \qquad (15)$$

$$\frac{dM}{dx} = -V_y \qquad (16)$$

$$\frac{dM_z}{dx} = -V_z \qquad (17)$$

$$\frac{dB}{dx} = T_\omega \qquad (18)$$

onde as ações ativas são N, M_y, M_z e B e as reativas são V_y, V_z e T_ω (em geral despreza-se T_σ). O torçor de empenamento T_ω representa a soma das parcelas referentes ao empenamento longitudinal e transversal, grafadas como $T_{\bar{\omega}}$ e $T_{\bar{\bar{\omega}}}$, respectivamente; para os casos correntes, em geral, despreza-se a parcela $T_{\bar{\bar{\omega}}}$, considerando-se $T_{\bar{\omega}} = T_{\bar{\bar{\omega}}}$, exceto nas seções em que $J_{\bar{\omega}} \cong 0$, por exemplo, seções L, T, K, etc.

Em regime plástico as tensões longitudinais σ_X sofrem influência da torção de Saint-Venant, T_S, que origina τ^s_{sx} (tensão cisalhante devida a T_S); por outro lado as tensões τ^s_{sx} são afetadas pelas ações solicitantes N, M_y, M_Z e B. Em geral quando σ_X é máxima τ^s_{sx} não o é, e vice-versa. A não aplicabilidade do Princípio da Superposição dos Efeitos em regime plástico leva à seguinte simplificação: devido à impossibilidade de levar em conta as influências de σ_X sobre τ^s_{sx} e vice-versa, faz com que as ações ativas N, M_y e B sejam desacopladas de T_S.

Esta simplificação torna possível a divisão do estudo em regime plástico em duas regiões distintas, a primeira sob domínio da torção de Saint-Venant e a segunda sob domínio da flexo-torção, na qual são realçadas as solicitações ativas, logo:

- Região 1:predominância de T_S, originando τ^S_{SX};
- Região 2:predominância de N, M_y, M_Z e B, originando σ_X.

As equações de equilíbrio interno são dadas por:

$$N = \int_s \int_{-t/2}^{t/2} \sigma_x \cdot dn \cdot ds \qquad (19)$$

$$M_y = -\int_s \int_{-t/2}^{t/2} \sigma_x \; z \cdot dn \cdot ds \qquad (20)$$

$$M_z = -\int_s \int_{-t/2}^{t/2} \sigma_x \; y \cdot dn \cdot ds \qquad (21)$$

$$B = -\int_s \int_{-t/2}^{t/2} \sigma_x \, \omega \cdot dn \cdot ds \qquad (22)$$

Em regime plástico perfeito a tensão σ_x atinge o valor f_y, tornando-se constante. A utilização da função SINAL(x) permite reescrever as equações de equilíbrio interno sob a forma:

$$N = f_y \int_s \int_{-t/2}^{t/2} \text{SINAL}(\epsilon_x) dn \cdot ds \tag{23}$$

$$M_y = -f_y \int_s \int_{-t/2}^{t/2} \text{SINAL}(\epsilon_x) dn \cdot ds \tag{24}$$

$$M_z = f_y \int_s \int_{-t/2}^{t/2} \text{SINAL}(\epsilon_x) dn \cdot ds \tag{25}$$

$$B = -f_y \int_s \int_{-t/2}^{t/2} \text{SINAL}(\epsilon_x) dn \cdot ds \tag{26}$$

Estas expressões mostram que as ações ativas quando da plastificação dependem apenas de direção da deformação específica — SINAL(ϵ_x) —, independendo do valor desta. Como ϵ_x possui quatro parcelas, cada uma correspondente à sua respectiva ação ativa, é possível elaborar um domínio de plastificação quadri-dimensional na flexo-torção, originando superfícies de interação entre as ações ativas e, portanto, doze curvas de interação. As superfícies de interação são convexas, mas não uniformes em geral, isto é, podem possuir pontos de inflexão. A Figura 2 ilustra as parcelas de ϵ_x:

$$\epsilon_x = \frac{\partial u}{\partial x} = \epsilon_o - z\xi'' - y\eta'' - \omega\theta'' \tag{27}$$

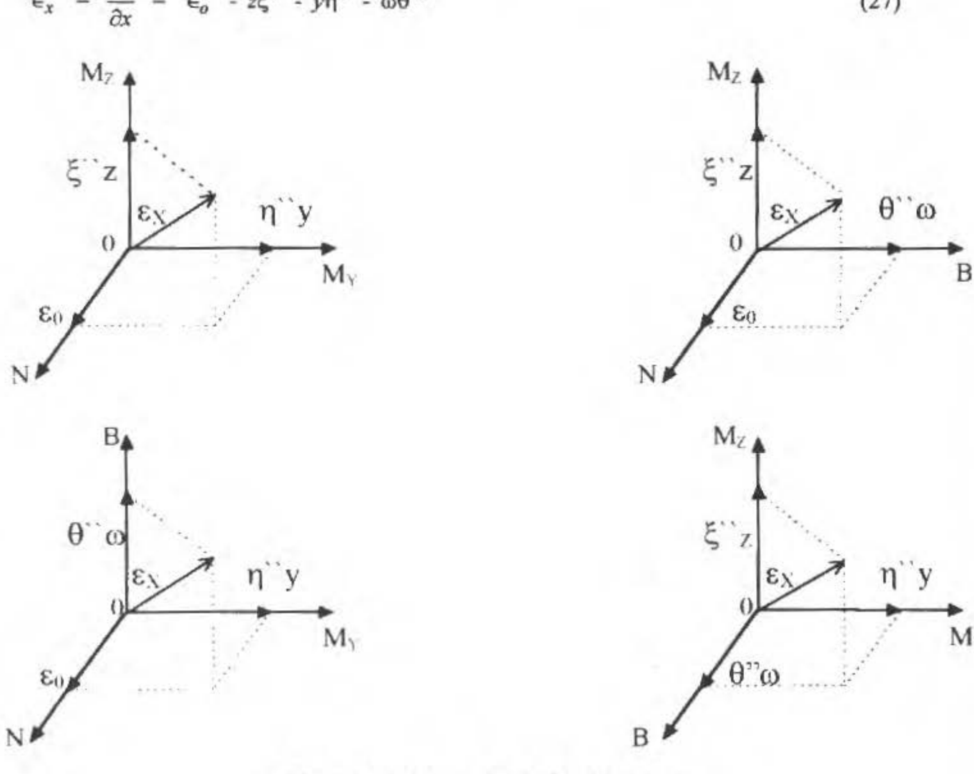

Fig. 2 Vetores ϵ_x Devidos às Ações Ativas

Sistemas de Referência em Regime Plástico

A obtenção dos eixos principais coordenados e pólo principal é efetuada após o desacoplamento das ações ativas (ações que originam tensões normais), aliado ao conceito de função sinal de Prager. Desacoplando-se as ações ativas, isto é, fazendo $N = 0$, $M_y = 0$ e $B = 0$, que acarreta $\epsilon_o = 0$, $\xi'' = 0$, $\eta'' = 0$ e $\theta'' = 0$, respectivamente; este é um procedimento usual na Teoria da Plasticidade. Substituindo-se as parcelas que contribuem para ϵ_X quando uma ação é desacoplada, chega-se a um sistema de equações que resolvido determina univocamente os eixos principais coordenados e o pólo principal.

Fazendo-se primeiramente $N = 0$, tem-se que $\epsilon_o = 0$; substituindo-se a expressão $\epsilon_X = -\xi''z - \eta''y - \theta''\omega$ na Eq. 23 e procedendo-se de modo análogo para as demais ações ativas ($M_y = 0$, $\eta'' = 0$; $M_Z = 0$, $\xi'' = 0$; $B = 0$, $\theta'' = 0$) ficam definidas as seguintes expressões:

$$N = \int_s \int_{-t/2}^{t/2} \text{SINAL}(-\xi''z - \eta''y - \theta''\omega)\, dn \cdot ds \tag{28}$$

$$M_y = -\int_s \int_{-t/2}^{t/2} \text{SINAL}(\epsilon_0 - \xi''z - \theta''\omega)\, dn \cdot ds \tag{29}$$

$$M_z = \int_s \int_{-t/2}^{t/2} \text{SINAL}(\epsilon_0 - \eta''y - \theta''\omega)\, dn \cdot ds \tag{30}$$

$$B = -\int_s \int_{-t/2}^{t/2} \text{SINAL}(\epsilon_0 - \xi''z - \eta''y)\, dn \cdot ds \tag{31}$$

Como $\text{SINAL}(\epsilon_X)$ é um operador de posição e as parcelas que compõem ϵ_X são quaisquer, segue-se que o sistema formado pelas Eqs. 28, 29, 30 e 31 necessita de valores de ϵ_o, $\xi''z$, $\eta''y$ que o satisfaça simultaneamente, para que se torne possível a obtenção de um sistema coordenado principal; alia-se ainda a necessidade de satisfazer a Eq. 31 para obter-se o pólo principal. Face à grande variedade de valores que podem tomar as parcelas que compõem os argumentos das funções sinal, embutidas nas equações do sistema quadri-dimensional, sendo que a combinação dessas parcelas entre si elevam enormemente o grau de dificuldade para resolver o sistema, pode-se afirmar com grande plausibilidade que: em regime plástico é praticamente impossível a obtenção de um sistema principal coordenado e de um pólo principal.

O centro de cisalhamento C pode variar para cada estágio de solicitação em regime plástico, sendo fundamental a determinação dos limites, máximo e mínimo, que o mesmo pode atingir para cada tipo de seção transversal.

Definida uma peça cilíndrica de seção transversal qualquer e por simplicidade admite-se que a mesma possua um eixo de simetria; determinado o centro de cisalhamento em regime elástico referenciado à um sistema cartesiano baricêntrico (Fig. 3), cujas coordenadas são $(a_{Z,e\ell};\ 0)$. Quando da plastificação, o centro de cisalhamento da seção, anteriormente situado sobre uma reta de inclinação constante e contida no plano de simetria da seção, varia em função da coordenada longitudinal, sendo que a função que define sua mudança assume valores definidos e contidos no plano de simetria.

Para cada tipo de carregamento externo e condição de contorno do elemento estrutural, fica definida a função $C_{p\ell} = F(x)$ em determinado estágio de solicitação após a plastificação, ressaltando-se que $C_{p\ell} = F(x)$ deve obedecer determinados limites para cada seção específica. Com a variação de $C_{p\ell} = F(x)$ e tendo-se que o plano de solicitação, por hipótese, permanece inalterado, pode-se concluir pela existência de torçores secundários no regime plástico, que em geral são desprezados.

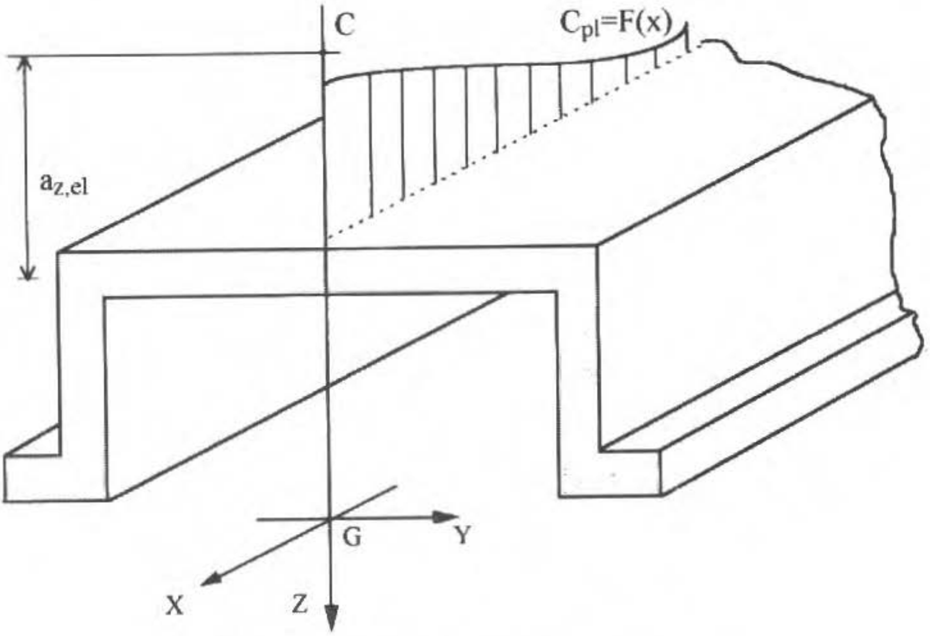

Fig. 3 Centro de Cisalhamento em Regime Elástico

Interação entre Esforços Seccionais

A Figura 4 ilustra a seção em "U", definindo seus parâmetros geométricos e mostrando a distribuição de tensões ao longo de seu perímetro, quando da plastificação total da seção.

As expressões seguintes, adaptadas de Mrázik et alii (1987), permitem visualizar resumidamente o comportamento desse perfil para a ação solicitante de flexão segundo o eixo OZ e de Bimomento.

O centro de cisalhamento quando da plastificação total da seção é dado por:

$$a_z = \frac{B_o^2 t_1 D_o}{2\left(B_o t_1 D_o + t_2 \dfrac{D_o^2}{4}\right)} \tag{32}$$

sendo

$$Z_z = B_o t_1 D_o + t_2 \frac{D_o^2}{4} \tag{33}$$

o módulo de resistência à flexão da seção totalmente plastificada, logo:

$$a_z = \frac{B_o t_1 D_o}{2Z_z} \tag{34}$$

No regime elástico tem-se:

$$a_{z,e\ell} = \frac{B_o t_1 D_o}{2W_z} \tag{35}$$

onde W_Z é o módulo de resistência à flexão, que admitindo-se $D \cong D_0 \cong d$, fica:

$$W_z = B_o t_1 D_o + \frac{1}{6} t_2 D_o^2 \tag{36}$$

A relação entre a posição do centro de cisalhamento no regime plástico e elástico é dada por:

$$a_{z,p\ell} = \frac{W_z}{Z_z} a_{z,e\ell} = \frac{1}{a_z} a_{z,e\ell} \tag{37}$$

e como $\alpha_Z > 1$, verifica-se que o centro de cisalhamento aproxima-se da mesa quando da plastificação.

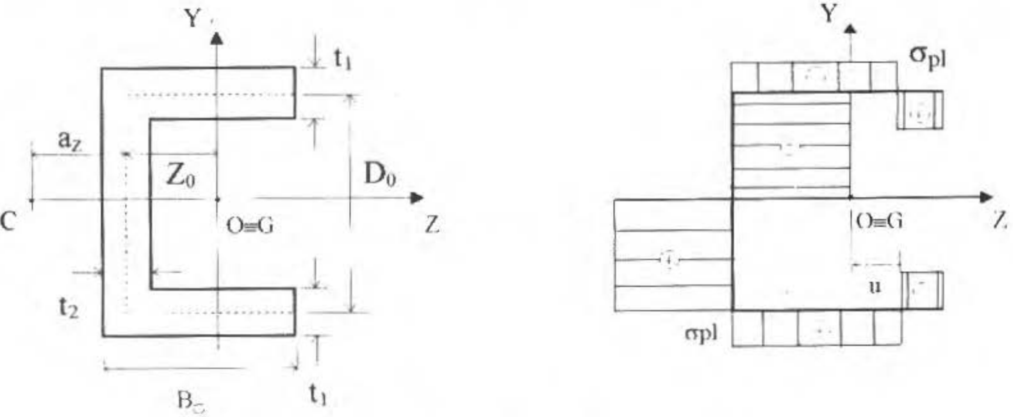

Fig. 4 Perfil U - Geometria e Distribuição de Tensões Normais Plásticas

O equilíbrio interno permite escrever:

$$M_z = \int_A \sigma_{p\ell} y \, dA = \sigma_{p\ell}\left[t_l\left(2Z_o + 2u - B_o\right) + t_2 \frac{D_o}{4}\right] D_o \tag{38}$$

$$\begin{aligned} B \; &= \int_A \sigma_{p\ell}\omega \, dA = 2\left\{\sigma_{p\ell} t_l \left(Z_o + u\right)\left[a_z \frac{D_o}{2} - \frac{D_o}{2}\left(\frac{Z_o + u}{2}\right)\right]\right\} - \\ &-\sigma_{p\ell} t_l \left(B_o - Z_o - u\right)\left[a_z \frac{D_o}{2} - \frac{D_o}{2}\left(Z_o + u\right) - \left(\frac{B_o - Z_o - u}{2}\right)\right] + \sigma_{p\ell} a_z t_2 \frac{D_o^2}{8} \end{aligned} \tag{39}$$

ou iterando esses dois esforços

$$\mathrm{B} = \mathrm{M_z a_z} + \mathrm{s_{p\ell} t_1}\left[\frac{\mathrm{B_o^2}}{\mathrm{t_1}} - (\mathrm{Z_o} - \mathrm{u})^2\right]\mathrm{D_o} \tag{40}$$

Eliminando o termo $(Z_0 - u)$ das Eqs. 38 e 39:

$$\sigma_{p\ell}^2 Z_\omega - \sigma_{p\ell}(\mathrm{B} - \mathrm{JM_z}) - \frac{\mathrm{M_z^2}}{4\mathrm{C}} = 0 \tag{41}$$

que é a equação quadrática da tensão normal de plastificação, com seus parâmetros definidos por:

$$Z_\omega = \left(B_o^2 t_l + \frac{B_o t_2 D_o}{2} - \frac{t_2 D_o^2}{16 t_l}\right)\frac{D_o}{4} \tag{42}$$

que é o módulo de resistência plástica ao bimomento e as relações geométricas

$$C = tlDo \tag{43}$$

$$J = a_z - \frac{B_o}{2} + \frac{t_2}{t_l} \cdot \frac{D_o}{8} \tag{44}$$

Referências

Mrázik, A.; Š Kaloud, M.; Tochác Ě K, M., 1987, - "Plastic Design of Steel Structures"; Ellis Horwood Ltd, Czechoslovakia.

Kollbrunner, C.F.; Haydin, N. 1975, "Dünnwandige Stäbe - Band 2"; Springer Verlag, C.D.R.

Murray, N.W., 1986, "Introduction to the Theory of Thin-Walled Structures"; Oxford Engineering Series, United Kingdon.

Gjelsvik, A., 1981, "The Theory of Thin Walled Bars"; Wiley-Interscience Publicaion, U.S.A.

Chen, W.F., Han, D.J. , 1988, "Plasticity for Structural Engineers"; Springer Verlag, U.S.A.

Flügge, W., 1973, "Stresses in Shells", Springer-Verlag, U.S.A.

Åkesson, B.; Bäcklund, J., 1973, "Plastisches Wlassowsches Wölbwirdestandsmoment Offener Walzprofile"; Der Stahlbau, pp. 13-19, B.R.D.

RBCM - J. of the Braz. Soc. Mechanical Sciences
Vol. XIX - No.1 - 1997 - pp. 58-71

ISSN 0100-7386
Printed in Brazil

Application of PFS Model (Production Flow Schema) Based Analysis of Manufacturing Systems for Performance Assessment

Paulo Eigi Miyagi
Wilson Munemassa Arata
Lucas Antonio Moscato
Universidade de São Paulo
Escola Politécnica
Departamento de Engenharia Mecânica
05508-900 São Paulo, SP Brasil

Abstract

The present work shows a modeling procedure for discrete manufacturing systems based on Production Flow Schema (PFS). A systematic approach to construct GSPN (Generalized Stochastic Petri Net) models is proposed, whose isomorphism with Markov process allows the extraction of quantitative data. The paper addresses a way to get information that is meaningful for manufacturing systems instead of using probabilities of the states of the Markov chain. Finally, a procedure to perform a sensitivity analysis allows to assess the influence of the quantitative parameters on system behavior.

Keywords: Manufacturing System, Modeling Methodology, Petri Nets, Performance Evaluation, Quantitative Analysis

Introduction

The analysis of manufacturing systems involves extensive performance evaluation, in accordance with Silva and Vallete (1989). Such evaluation results give important information for many decision-making activities, for example in assessing the economical issues of an implementation, where performance figures such as production rates and inventory are strongly required. The present work focus on modeling and quantitative performance analysis of manufacturing systems.

Several aspects are usually considered for system analysis, the shop floor layout, number of machines, processing machines and transportation subsystem capacities (speed), buffer sizes, strategies adopted for the operations coordination (assignment of machines to operations, priorities, sequencing, etc.) and setup times. In systems design, the search for a suitable combination of these parameters involves decisions concerning technical and economical tradeoffs.

Since the study is concerned with the organization of a set of manufacturing operations and not with the behavior of low level sensoring and actuation devices, the techniques developed for Discrete-Event Dynamic Systems are appropriate. Among the most known, we can cite Petri Nets, Markov Chains and Queuing Networks.

For the validation of a manufacturing system, Petri nets (Peterson, 1981; Reisig, 1985, 1992) offer some advantages:

- A graphical and precise formalism that allows easy dialogue between the different teams (designers, contractors, users, etc.) that participate in the analysis process about the expected behavior of the system.
- The ability to model features such as process synchronization, decision processes and sequencing.
- A well-founded theory for the verification of qualitative properties.

While Petri Nets deal with issues about the logic of the system's dynamics, the other techniques are used for extracting quantitative information from their models. For example:

Manuscript received: July 1996. Technical Editor: Leonardo Goldstein Jr.

- The Markov Chains technique (Papoulis, 1984; Kleinrock, 1976) is an effective way to study the behavior of the probabilities of the states of a described system. The main disadvantage is the state space explosion that occurs even in moderate size systems (Silva, 1992).

- The Queuing Networks technique (Kleinrock, 1976) is a useful way to obtain information related to clients, such as, workpieces, tools and raw materials that need services (e.g., machining, transportation) which are accomplished by service centers. The information that can be obtained by the network analysis includes average waiting time, average number of clients, etc. One major drawback in this technique is how to treat the synchronization and blocking of entering clients (Jungnitz et al., 1992).

One can observe that each of the above techniques deals with different aspects of manufacturing systems, because they model different features with different kinds of information. In Marsan et al. (1984) and Molloy (1982), an extension for Petri Nets called GSPN (Generalized Stochastic Petri Nets) are presented and is shown as an approach that merges the characteristics of the models above, like ease of representation, modeling of synchronization and consideration of the involved timings. As a consequence, it is possible to perform qualitative and quantitative evaluation of the dynamics of a manufacturing system in a relatively unified way.

A very important aspect to point out is the necessity of manufacturing systems to have a progressive modeling because they are usually large and complex. The refinement mechanism of the modeling allows the construction of hierarchically structured models. If a suitable set of refinement/transformation rule is defined, there will be a pay off in the forthcoming modeling and analysis.

The present work introduces an approach for manufacturing systems modeling by a refined PFS (Production Flow Schema), from where it is obtained a GSPN model for systems analysis. The paper also presents a procedure to obtain the required performance figures for manufacturing systems.

Overview of The Analysis Methodology

Several powerful techniques have been already developed and applied in modeling manufacturing systems. Many of the proposals include extensions, combinations and variations of the same techniques, in an attempt to suit them for specific purposes or to deal with systems that have some peculiarities, allowing deeper evaluations. However, a major concern still remains: the generation of models themselves.

Usually, the construction of models is not a simple task; the most frequent problem is to view the system from as many different perspectives as possible, so that the several demands by the interacting people in a project can be met (like analysis for correctness, performance, system reliability, controllability, implementability and so on). In this context, Petri nets are recognized as the friendliest approach. It is based on a few simple structural elements and some describing some rules (relatively easy to understand, but general enough to represent important dynamical features in systems activities). Also, Petri nets present the ability to define and describe hierarchical structures.

Despite such features the potential of Petri nets is very likely to be wasted without a systematic and rational modeling procedure, and the use of Petri nets for modeling real systems may show negligible or no advantages at all. To alleviate this problem and, at the same time, take full advantage of the available analytic tools, a methodology to construct a model for analysis of discrete event manufacturing systems is presented.

Figure 1 shows the main structure and the steps of the procedure. The following sections will detail the methodology.

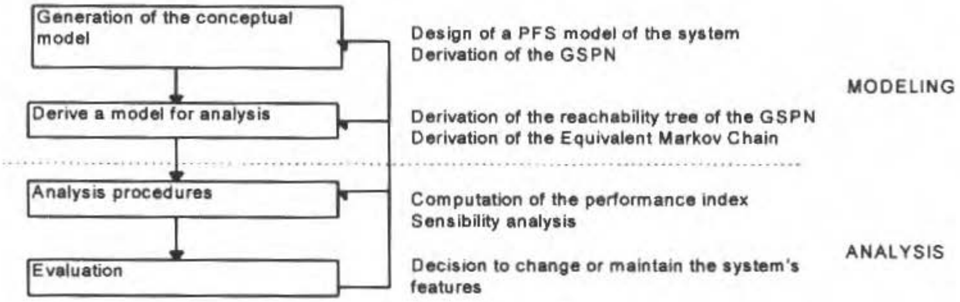

Fig. 1 Methodology for Analysis of Discrete Manufacturing Systems

Modeling of Systems

Conceptual Modeling

At the conceptual level, the aim is modeling the main characteristics of the functions to be considered in a manufacturing system analysis. It is necessary to identify the precedence relationships between operations, the elements that promote and control the parallelism and the identification of the involved decision processes in the routing of parts and the resources sharing, without further detailing.

Based on the Petri nets' ability to describe the system's hierarchy, it is used the PFS - Production Flow Schema (see Hasegawa et al., 1988; Miyagi et al., 1988; Silva and Miyagi, 1995 and Appendix A) - to represent a higher level of abstraction of the system without representing the system dynamics. By deferring the inclusion of detailed dynamics' rules, there is a delay in commitment (Thembleby, 1988), meaning that we state hypothesis only when necessary for the comprehension of the problem. Therefore, we benefit from avoiding (a) undesirable restrictions in the later detailing of the model and (b) the consequences of verifying the invalidity of some of the hypothesis, that can lead to an onerous and unsafe restructuring of the model. The PFS allows representing the essential elements of manufacturing systems without detailing them, which can be made later when there is a clearer knowledge of the dynamics to deal with.

The operation of a manufacturing system is represented by an abstraction where the *activities* involve interactions between *clients* and *resources*, which is a first way to organize the available data, and whose structure evolves to other functional (detailed) models, making them easier to understand.

Through PFS, a model in GSPN is obtained. The interest of the authors is restricted to live, limited and reinitializable nets, ensuring that the isomorphic Markov chain will be ergodic (Marsan et al., 1984; Molloy, 1982).

To illustrate the methodology and present some actual data, it is given a simple example of the operations of a manufacturing system whose PFS is shown in Fig. 2. The present section and the following section deal with the example.

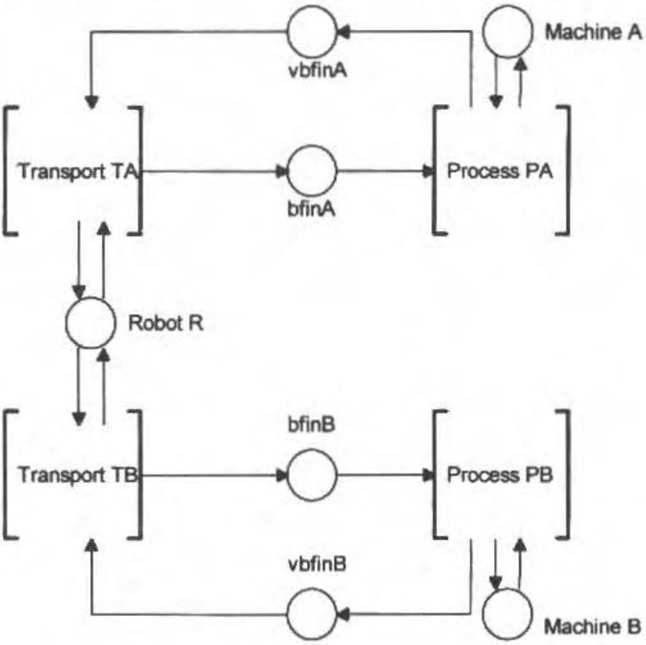

Fig. 2 PFS of a Manufacturing System (Conceptual Description of the System)

There are two activity sequences: TA-PA and TB-PB. Sub-system R is constituted by robots, whose resources may be allocated by transport activities TA and TB, being a potential case of resource sharing. Vacancies in the input buffer of the processing center A, vbfinA, can be allocated by TA and released by PA; the interpretation of vbfinB (vacancies in the input buffer of the processing center B), TB, and PB is analogous. The resources of the processing centers (machines A and B) have their allocation-release cycles associated with the activities PA e PB, respectively. Clients go through the buffers bfinA and bfinB between transport and processing activities.

Construction of the GSPN

GSPN detail the dynamic behavior of the activities by representing rules that regulate the interactions among conditions, which cause their appearing, maintenance and vanishing. Conditions are any relevant information which regulates the behavior's evolution of a system; these conditions and their combinations are called states (Peterson, 1981). In terms of GSPN elements, the following interpretations are adopted:

- Places represent conditions (e.g., processing in course, parts being transported, client waiting in a buffer and operation in stand-by).

- The presence of tokens in a place indicates that the corresponding condition is verified; their absence indicates the opposite.

- Transitions specify what pre-conditions must be satisfied (verified) to generate other conditions; their firing represent the vanishing of certain conditions and generation of others. The temporization models the permanence times of the conditions represented by the places that enable timed transitions.

Thus, refining Fig. 2, it is possible to have a GSPN as shown on Fig. 3.

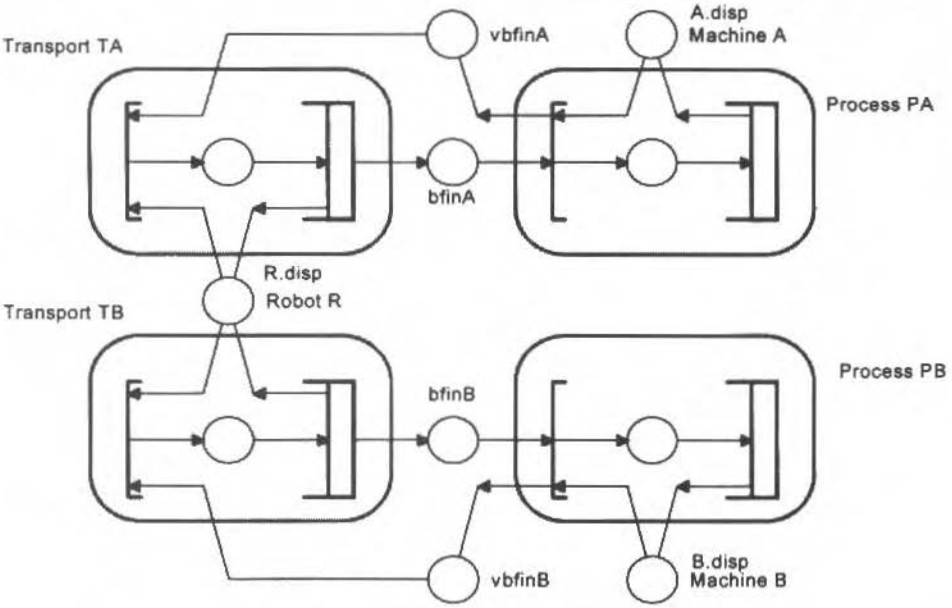

Fig. 3 GSPN of Fig. 2 (Detailed Structure of the System)

It is important to remember that this is only one of the possible "translations," from a PFS to GSPN, each one being suited for the peculiarities of a desired dynamic behavior. In this case, the distributors are translated directly into places, which represent availability of resources (vbfinA, vbfinB, R.disp, A.disp and B.disp) or clients stopped in buffers (bfinA and bfinB); resources are available if there are tokens in the corresponding places.

The activities are represented by sub-nets in GSPN: one transition represents the beginning of the activity, conditioned to resources availability (TA and TB begin if there are free places in the input buffers and available robots; the activities PA and PB begin with the allocation of machines from the processing centers while releasing buffer vacancies); a place representing operation in course; a timed transition whose firing rate characterizes the time of execution and whose firing indicates the end of the activity, causing the release of resources.

The model obtained so far considers the qualitative aspects of the functions performed by the system, i.e., how the activities are organized and when resources are allocated. To study the quantitative aspects, the following considerations are included in the graph:

- Number of resources: this is defined by an initial marking where all resources are available, i.e., only places that represent resources availability (in the example, A.disp, B.disp, R.disp, vbfinA and vbfinB) have tokens, as many as the quantity of the respective resources in the system, while there are no tokens in the places that indicate resources occupation.
- Temporization, given by the respective firing rates.

In order to illustrate it, the following example is given: there are two robots to execute the transports in the processing centers A and B, two vacancies in each of the inputs buffers of both machines and one machine in each processing center. The rate $1000n_A$ is attributed for the transition t_{TA}, where n_A represents the number of marks in p_{TA}; each mark in p_{TA} indicates one robot transporting one client. Thus, two tokens represent two transport activities in course and then the ending rate of these dislocations is twice as much as in the case of a single robot. By analogy, a rate of $2000n_B$ is defined for t_{TB}. For the timed transitions involved in process P_A and P_B, are attributed the rates of 1000 and 2000 parts per day. The interpreted GSPN model, corresponding to this situation, is illustrated in Fig. 4.

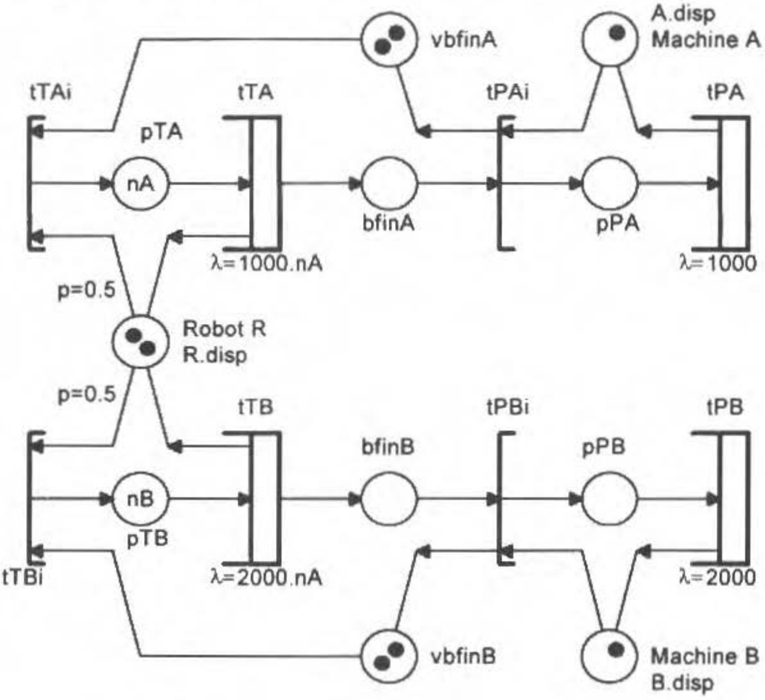

Fig. 4 Marked GSPN of Fig. 3 (Functional Description of the System)

Analysis of Systems

The quantitative analysis treated in this work is not done directly over a GSPN, but over a Continuous Time Markov Chain (CTMC) (Papoulis, 1984; Kleinrock, 1976) isomorphic to it. A GSPN model the rules and time constraints that govern the dynamic behavior of the system through the flow of tokens. The isomorphic CMTC models the states and the transitions between states of the respective GSPN. These states represent the different arrangements of tokens on the GSPN that result from the flow of tokens. State transitions therefore represent the firing of GSPN transitions. These transition states are assigned-transition rates that measure the permanence time in states before the transition takes place. The method used for the derivation of CMTC from GSPN and that copes with the calculation of these timing features and the introduction of the probabilities defined by random switches into the Markovian model is based on the approach proposed by Marsan et al. (1984).

In that approach, it is considered the case of live, bounded, reinitializable nets, with the additional restriction that there are no cycles with vanishing states. Such nets are represented by isomorphic CMTC which are ergodic. Once the CMTC is obtained, we compute its steady state probabilities represented by the vector $\pi=[\pi 1, \pi 2, ..., \pi n]$, where n is the number of states (tangible) effectively modeled by the CTMC.

From the GSPN given in Fig. 4, we obtain a CTMC whose transition rate matrix $\mathbf{Q}=[q_{ij}]_{nxm}$ is given by expression (1), where "." denotes 0 and q_{ij} ($i\neq j$) has the value of the transition rate of the transition from the state i to j defined by CMTC. When i=j, $q_{ij}=-\sum_{k\neq i} q_{ik}$. We obtain π by solving $\pi.Q=0$.

$$Q^T = 1000 \cdot \begin{bmatrix}
-4 & 2 & 1 & . & . & . & . & . & . & . & . & . & . & . & . & . & . & . & . & . & . & . & . & . & . & . & . & . \\
. & -6 & . & 1 & . & . & . & . & . & . & . & . & . & . & . & . & . & . & . & . & . & . & . & . & . & . & . & . \\
. & . & -5 & 2 & 0.5 & . & . & . & . & . & 1 & . & . & . & . & . & . & . & . & . & . & . & . & . & . & . & . & . \\
. & . & . & -7 & . & 0.5 & . & . & . & . & . & 1 & . & . & . & . & . & . & . & . & . & . & . & . & . & . & . & . \\
. & . & . & . & -3 & 2 & . & 1 & . & . & . & . & . & . & . & . & . & . & . & . & . & . & . & . & . & . & . & . \\
4 & . & . & . & 1 & -5 & 2 & . & 1 & . & . & . & . & . & . & . & . & . & . & . & . & . & . & . & . & . & . & . \\
. & 4 & . & . & . & 1 & -5 & . & . & 1 & . & . & . & . & . & . & . & . & . & . & . & . & . & . & . & . & . & . \\
. & . & . & . & 0.5 & . & . & -4 & 2 & . & . & . & . & . & . & 2 & . & . & . & . & . & . & . & 1 & . & . & . & . \\
. & . & 4 & . & . & 0.5 & . & 1 & -6 & 2 & . & . & . & . & . & . & 2 & . & . & . & . & . & . & . & 1 & . & . & . \\
. & . & . & 4 & . & . & 1 & . & 1 & -6 & . & . & . & . & . & . & . & 2 & . & . & . & . & . & . & . & 1 & . & . \\
. & . & . & . & . & . & . & 0.5 & . & . & -5 & 2 & . & . & . & . & . & . & . & . & . & . & . & . & . & . & 1 & . \\
. & . & . & . & . & . & . & . & 0.5 & . & . & -7 & . & . & . & . & . & . & . & . & . & . & . & . & . & . & . & 1 \\
. & . & . & . & . & . & . & . & . & . & . & . & -3 & 1 & 2 & . & . & . & . & . & . & . & . & . & . & . & . & . \\
. & . & . & . & . & . & . & . & . & . & . & . & 1 & -4 & . & . & . & . & . & . & . & . & 2 & . & . & 2 & . & . \\
. & . & . & . & . & . & . & . & . & . & . & . & 2 & . & -5 & . & . & . & . & . & . & . & . & . & . & 1 & . & 4 \\
. & . & . & . & . & . & . & . & . & . & . & . & . & . & . & -2 & 2 & . & . & 1 & . & . & . & . & . & . & . & . \\
. & . & . & . & 1 & . & . & . & . & . & . & . & . & . & . & . & -4 & 2 & . & . & 1 & . & . & . & . & . & . & . \\
. & . & . & . & . & 1 & . & . & . & . & . & . & . & . & . & . & . & -4 & 2 & . & . & 1 & . & . & . & . & . & . \\
. & . & . & . & . & . & 2 & . & . & . & . & . & . & . & . & . & . & . & -4 & . & . & . & 1 & . & . & . & . & . \\
. & . & . & . & . & . & . & . & . & . & . & . & . & . & . & . & . & . & . & -3 & 2 & . & . & . & . & . & . & . \\
. & . & . & . & . & . & . & 1 & . & . & . & . & . & . & . & . & . & . & . & . & -5 & 2 & . & . & . & . & . & . \\
. & . & . & . & . & . & . & . & 1 & . & . & . & . & . & . & . & . & . & . & . & . & -5 & 2 & . & . & . & . & . \\
. & . & . & . & . & . & . & . & . & 2 & . & . & . & 1 & . & . & . & . & 2 & . & . & . & -5 & . & . & . & . & . \\
. & . & . & . & . & . & . & 0.5 & . & . & . & . & . & . & . & . & . & . & . & 2 & . & . & . & -4 & 2 & . & . & . \\
. & . & . & . & . & . & . & . & 0.5 & . & 4 & . & . & . & . & . & . & . & . & . & 2 & . & . & 2 & -6 & 2 & . & . \\
. & . & . & . & . & . & . & . & . & 1 & . & 4 & . & 2 & 1 & . & . & . & . & . & . & 2 & . & . & 2 & -6 & . & . \\
. & . & . & . & . & . & . & . & . & . & . & . & . & . & . & . & . & . & . & . & . & . & . & 1 & . & . & -5 & 2 \\
. & . & . & . & . & . & . & . & . & . & . & . & . & . & 2 & . & . & . & . & . & . & . & . & . & 1 & . & 4 & -7
\end{bmatrix} \qquad (1)$$

We can observe that its by-hand construction (28 nodes and connecting arcs) is somewhat cumbersome when compared to the GSPN that originated it, which illustrates the benefits from the ease of representation of GSPN. Also, it can be shown that the GSPN is live, bounded and reinitializable, so that the ergodicity of the CTMC is ensured and its equilibrium state probabilities can be calculated.

Performance Indexes

Information that can be obtained from π in a more convenient form for the evaluation of the manufacturing system is called performance indexes. Here, we use three of them:

Definition 1 - Idleness degree of a resource R: represent the probability of having R available or idle. It is calculated by:

$$G_{idle}(R) = \sum_{i \in V(R)} \pi_i \qquad (2)$$

where V(R) represents the set of CTMC states in which the place corresponding to the availability of R has at least one token.

Definition 2 - Average number of clients in buffer b, given by:

$$\overline{N}(b) = \sum_{i=1}^{n} \pi_i [\sum_{p_j \in B(b)} m_i(p_j)] \qquad (3)$$

where mi(pj) represents the number of tokens in place pj on state (or marking) i and B(b) represents the set of places that indicates that there are clients waiting to be removed from buffer b.

Definition 3 - Throughput of an activity A represents the execution rate of an activity or the effective rate of clients served. It is given by:

$$T(A) = \sum_{i \in H(A)} \pi_i \lambda_i(A) \tag{4}$$

where H(A) represents the set of states in which the transition t_A corresponding to the end of activity A is enabled and $\lambda_i(A)$ represents the firing rate of t_A on the marking i.

In the case represented by Fig. 4, the indexes obtained are shown on Tables 1, 2 and 3.

Table 1 Idleness Degree of Resources

Resource R	$G_{idle}(R)$
R.disp	0.2890
vbfinA	0.2384
vbfinB	0.3941
A.disp	0.1536
B.disp	0.2335

Table 2 Average Number of Clients in the Buffers

buffer b	$\bar{N}$(buffer)
bfinA	0.9015
bfinB	0.7542

Table 3 Activity Throughputs

Activity A	T(A)
T_A	846.4290
P_A	846.4293
T_B	1533.0900
P_B	1533.0907

The relatively low idleness degree of R indicates that the transport activities are intense. The average number of clients in buffers bfinA and bfinB are below the maximum allowed to both of them; the idleness level of the processing centers A and B is higher than the ideal (null), but it can be justified by the nature of the production (e.g., by the flexibility desired to the system); throughputs of activities are lower than the maximum (1000 and 2000 parts per day): these results may suggest that the bottleneck of the production system is the transport activity.

Sensitivity Analysis

Through sensitivity analysis as presented in Karnavas et al. (1993), it is possible to evaluate the influence of quantitative parameters over the performance indexes. Let *I* be a performance index and *A=(a1,a2,...,an)* be a vector of *n* quantitative parameters of the system's model, i.e., the firing rates and the random switches' probabilities (which compose the transition's probabilities derived from vanishing states).

Definition 4 - For a certain configuration of quantitative parameter A, the absolute sensitivity of an index I with respect to a parameter a_i, $S_{abs}(I,A,a_i)$, is given by:

$$S_{abs}(I, A, a_i) = \frac{\partial I}{\partial a_i} \tag{5}$$

Definition 5 - For a certain configuration of quantitative parameter A, the relative sensitivity of an index I with respect to a parameter a_i, Srel(I,A,a_i), is given by:

$$S_{rel}(I, A, a_i) = S_{abs}(I, A, a_i)\frac{a_i}{I} \tag{6}$$

Srel(I,A,a_i) represents the quotient between the relative variation of I resulting from a variation in a parameter ai and the relative variation of the same parameter a_i in a specific parametric configuration A.

The expressions for performance indexes can be represented by a product of two vectors: $I=\pi m$ where π is the line-vector of steady-state probabilities and m is a column-vector with n elements whose composition depends on the index to be used.

Then, the absolute sensitivity of I with respect to a_i is:

$$S_{abs}(I, A, a_i) = (\frac{\partial}{\partial a_i}\pi)m + \pi(\frac{\partial}{\partial a_i}m) \tag{7}$$

For the computation of probabilities, the following equations are used:

$$\pi Q=0 \tag{8}$$

$$\sum_{i=1}^{n}\pi_i = 1 \tag{9}$$

Deriving Eqs. (8) and (9):

$$(\frac{\partial}{\partial a_i}\pi)Q + \pi(\frac{\partial}{\partial a_i}Q) = 0 \tag{10}$$

$$\sum_{i=1}^{n}\frac{\partial \pi_i}{\partial a_i} = 0 \tag{11}$$

Rewriting Eq. (10):

$$(\frac{\partial}{\partial a_i}\pi)Q = -\pi(\frac{\partial}{\partial a_i}Q) \tag{12}$$

Through Eqs. (11) and (12), it is possible to obtain a linear system of equations of the type xA=B. From these relations we have the derivative of π with respect to a_i can be obtained and used in the expression (7), enabling the computation of sensitivities.

For the model in Fig. 4, relative sensitivities with respect to the quantitative parameters are presented in Tables 4, 5 and 6.

Table 4 Relative Sensitivities of the Resources' Idleness Degree

Parameters	Resources				
	R	vbfinA	vbfinB	A	B
pA	0.0537	-0.1491	-0.0800	-0.0721	-0.0520
pB	0.0471	-0.0552	-0.1538	-0.0423	-0.0947
λ(tTA)	0.4034	-0.1852	-0.6586	-0.2814	-0.2570
λ(tTB)	0.4038	-0.3594	-0.3307	-0.0985	-0.3432
λ(tPA)	-0.4268	0.3495	0.5211	0.3330	0.1650
λ(tPB)	-0.3804	0.1951	0.4682	0.0469	0.4352

Table 5 Relative Sensitivities of the Buffers' Average Number of Clients

Parameters	Resources	
	bfinA	bfinB
pA	0.1511	0.0883
pB	0.0868	0.1625
λ(tTA)	0.8274	0.5084
λ(tTB)	0.2518	0.9190
λ(tPA)	-0.9437	-0.3874
λ(tPB)	-0.1354	-1.0400

Table 6 Relative Sensitivities of the Activities' Throughputs

Parameters	Activities			
	TA	PA	TB	PB
pA	-0.0180	0.0721	-0.0475	0.0520
pB	-0.0478	0.0423	-0.0049	0.0947
λ(tTA)	0.2814	0.2814	0.2570	0.2570
λ(tTB)	0.0985	0.0985	0.3432	0.3432
λ(tPA)	0.6670	0.6670	-0.1650	-0.1650
λ(tPB)	-0.0469	-0.0469	0.5648	0.5648

Analyzing the resulting relative sensitivities, it is possible to conclude the following:

- The elements of the system present couplings, given that all of them influence the indexes to some degree.
- Consistent with the identification of the sub-system *R* as the main bottleneck of the production system, it can be noticed that an increase in its working capacity (given by parameters $\lambda(tTA)$ and $\lambda(tTB)$) gives the best results, since:
  - It brings down the work load on this sub-system (observed by the increase in its idleness degree);
  - It improves the use of other resources (decrease on the idleness degree and increase of work load of the processing centers, given by the increase on the average number of clients in the buffers), and

  - It increases the activities' throughputs.

- It is possible to verify that some interactions may not be evident when only indexes are analyzed, for example, that an increase in the processing capacity of centers *A* (or *B*), represented by $\lambda(tPA)$ (or $\lambda(tPB)$), generates a decrease of throughputs of the activities *TB* and *PB* (or *TA* and *PA*).

Conclusions

It is initially introduced a methodology where PFS is applied to generate a GSPN which is translated to the equivalent Markov chain model in a systematic and rational approach. The simple example given in this work illustrates the main procedures to describe more complex systems.

It was shown how some quantitative information, other than simple probabilities - and more meaningful for manufacturing systems - can be obtained from the steady-state probabilities. The computation of their sensitivity benefits from the fact that the linear algebraic equations for obtaining the steady-state probabilities vector and the one for obtaining its derivatives have the same coefficient matrix ($\boldsymbol{Q}$). Therefore, once the steady state probabilities have been computed, the sensitivity analysis can be carried out with relatively low computational cost. Although the tendencies evaluated by the sensitivities have a local nature, this cost may justify its calculation even in cases where the range of the parameter variation is larger, provided that the inherent inaccuracy can be justifiably tolerated.

Concerning large systems, it can be easily seen that the analysis of the isomorphic CMTC is computationally onerous even for medium sized systems. To deal with the size problem, approximation approaches have been considered such as:

- Partitioning the GSPN so that the submodels are analyzable (Jungnitz et al., 1992) by the means we have presented, and
- Aggregation of states in the isomorphic CMTC, as in Silva (1992).

The procedure and results of this work contribute to the design and evaluation of manufacturing systems, but we consider that the following points need further research:

- Development of a computer aided system to help the interpretation of the results;
- Implementation of efficient algorithms to compute indexes and sensitivities, including the possibility of employing approximate methods, and
- Study of the relationship between the curves "index versus quantitative parameters" and the model's components.

Acknowledgment

The authors are thankful to Dr. Raul Gonzales Lima and Dr. Marcelo Godoy Simões for the useful discussions in the revision of the text. The authors extend their gratitude to CAPES, CNPq, FAPESP and the European Community for their support in the activities of this research project.

Appendix A - Production Flow Schema (PFS)

PFS (Hasegawa et al., 1988; Miyagi et al., 1988; Silva & Miyagi, 1995) is a scheme derived from the Petri nets of the Channel-Agent type (Reisig, 1992). PFS is constituted by the following elements (see Fig. A1):

- Active elements or Activities: they are represented by open-sided rectangular blocks.

- Passive elements or Distributor: denoted by circles.
- Oriented arcs: connect activities to distributors (never two elements of the same type).

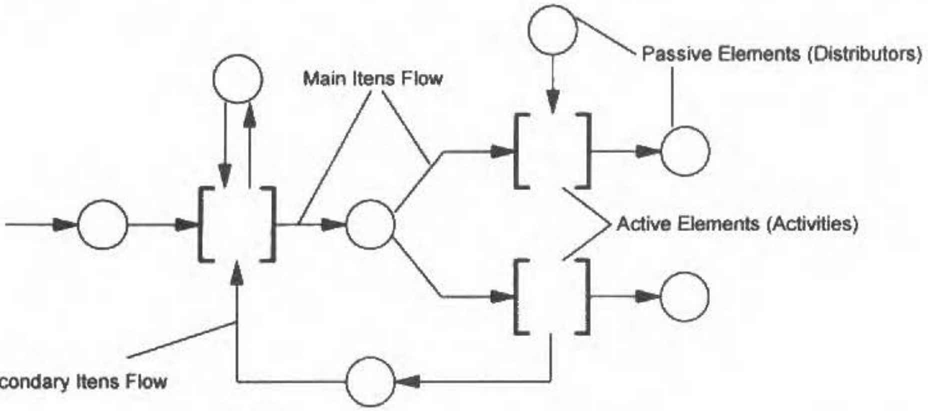

Fig. A1 PFS Graph and Structural Elements

PFS show how items involved in the production act in the execution of the functions necessary to obtain the desired products. An important concept presented by the PFS is the flow of items which represents the process of allocation and deallocation of items (which can be raw material, machines, tools, execution orders and control information) to an activity and in which execution they are involved. PFS indicate that the activities of a system (represented by the active elements) involve the interaction between items, theirs flows and other activities, which are represented by the elements connected by oriented arcs. Flow can be classified in primary and secondary:

- Primary flows are represented by the PFS elements connected to the closed edges of the activities.
- Secondary flows refer to elements that are linked to open sides of activities.

Closed edges of the activities indicate their beginning and ending. By the open ones, the connection to items tends to be more relaxed, at least at this level of abstraction: the way it interferes on activities must be specified in detailed models to be generated (e.g., sometimes, an item might not be used because another one was chosen to perform the same function).

Considering analysis of manufacturing systems, PFS specify a system structure, presenting explicitly the interaction between resources and clients. Resources are the system components with specific functions (e.g., machines, carriers, inspection systems); clients refer to the material substract on which the resources work (e.g., parts, lots of parts, pallets). Then, the convention used in its work can be described:

- Activities represent technological transformations such as operations done with resources (such as clients' movements or its property's transformation) and support tasks (such as resources allocation or malfunctioning machine signaling). Notice that these operations are not explained in this level of abstraction.
- Distributors have two functions:
    - Those involved in primary flows represent the clients being stored in the buffers or magazines.
    - Those that are part of the secondary flow of the activity blocks represent the resources to be used by the activities.
- About oriented arcs:

- Those belonging to primary flow indicate the possible activity sequences to be undergone by the clients.
- In the secondary flow, an arc entering the activity block indicates that the resource connected might be allocated; the outgoing arcs indicate that there might be release of the associated resource.

An example of PFS is given on Fig. A2, where some of the modeling characteristics are shown:

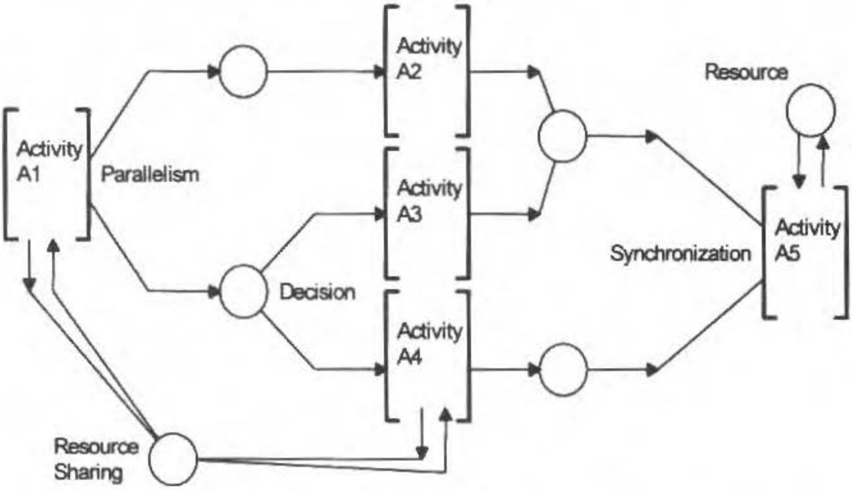

Fig. A2 Behavior Features Modeled by PFS

- Parallelization: The end of the activity A1 generates two clients that suffer different actions, one concurrently to another.
- Synchronization: In a broad sense, it is a way to restrict the parallelism, making the execution of one part of the processes obey some restrictions, such as waiting for a signal to come from other process or waiting for the release of some resource; in the Fig. A2, the activity A5 must wait for the presence of the items corresponding to its input.
- Decision: Clients have more than one option about the next activity. PFS only indicates the existence of the decision processes, which must be detailed in the subsequent refined models.
- Resources sharing: several activities may use the same resource, which can cause conflicts concerning the priority in its allocation; as in the previous item, the arbitration of conflicts must be specified in the detailed models.

References

Hasegawa K., Takahashi, K., and Miyagi, P.E., 1988, "Application of the Mark Flow Graph to Represent Discrete Event Production Systems and System Control", Transactions of the Society of Instrument and Control Engineers, Vol.24, No.1, pp 69-75.

Jungnitz, H., Sanches, B., and Silva, M., 1992, "Response Time Approximation for the Performance Analysis of Manufacturing Systems Modeled by Stochastic Marked Graphs", Proceedings of IEEE International Conference on Robotics and Automation, IEEE, Vol.2, pp 1000-1005.

Karnavas, W.J., Sanches, P.J., and Bahil, A.T., 1993, "Sensitivity Analysis of Continuous and Discrete Systems in the Time and Frequency Domains", IEEE Transactions on Systems, Man and Cybernetics, Vol.23, No.2, pp 488-501.

Kleinrock, L., 1976, "Queuing Systems", John Wiley & Sons, New York.

Marsan, M.A., Conte G., Balbo G., 1984, "A Class of Generalized Stochastic Petri Nets for the Performance Evaluation of Multiprocessor Systems", ACM Transactions on Computer Systems, Vol.2, No.2, pp 93-122.

Miyagi, P.E., Hasegawa, K., and Takahashi, K., 1988, "A Programming Language for Discrete Event Production Systems Based on Production Flow Schema and Mark Flow Graph", Transactions of the Society of Instrument and Control Engineers, Vol.24, No.2, pp 183-190.

Molloy, M.K., 1982, "Performance Analysis Using Stochastic Petri Nets", IEEE Transactions on Computers, Vol.31, No.9, pp 913-917.

Papoulis, A., 1984, "Probability, Random Variables and Stochastic Processes", 2nd Ed., McGraw-Hill, New York.

Peterson, J.L., 1981, "Petri Net Theory and the Modeling of Systems", Prentice-Hall, Englewood Cliffs.

Reisig, W., 1985, "Petri Nets - An Introduction", Springer-Verlag, Berlin-Heidelberg.

Reisig, W., 1992, "A Primer in Petri Net Design", Springer-Verlag, Berlin-Heidelberg.

Silva E.A.S., and Muntz, R.R., 1992, "Métodos Computacionais de Solução de Cadeias de Markov: Aplicações a Sistemas de Computação", 8ª Escola de Computação, SBC, Gramado, RS. (In Portuguese)

Silva, J R, and Miyagi, P E., 1995, "PFS/MFG: A high level net for the modeling of discrete manufacturing systems", in: Camarinha-Matos, L.M., Afsarmanesh, H. (Ed.), "Balanced Automation Systems - Archtectures and Design Methods", Chapman & Hall, London, pp 349-362.

Silva, M., and Vallete, R., 1989, "Petri Nets in Flexible Manufacturing", in: Rozenberg, G., "Advances in Petri Nets", Vol.424, Springer-Verlag, Berlin-Heidelberg.

Thembleby, H., 1988, "Delaying Commitment", IEEE Software, Vol.5, No.3, pp 78-86.

RBCM - J. of the Braz. Soc. Mechanical Sciences
Vol. XIX - No. 1 - 1997 - pp. 72-79

ISSN 0100-7386
Printed in Brazil

Effect of Porosity on the Strength Coefficient and Strain-Hardening Exponent of Sintered Ferrous Materials

Ernani Sales Palma
Universidade Federal de Minas Gerais
Departamento de Engenharia Mecânica
31260-901 Belo Horizonte, MG Brasil

Abstract

Some features of strain hardening of porous materials during tensile tests are considered. Modelling of true stress-true strain curves were done by using Ludwik's equation. The influence of porosity on the strain hardening exponent and on the strength coefficient for porous Fe, Fe-C, Fe-C-Cu and Fe-P alloys is presented and experimental results are discussed and compared with the literature.

Keywords: Sintered Materials, Strain Hardening, Mechanical Properties, Effects of Porosity

Introduction

When metallic materials are loaded in a simple tension test, a point of instability is reached as load is increased, and localized plastic strain begins. After this point, the load required to produce deformation reaches a maximum value, and then drops off until rupture takes place (Ratke and Welch, 1983, Petch and Armstrong, 1990 and Thomason, 1990). At this maximum, uniform strain becomes unstable and necking begins when strain-hardening rate becomes equal to flow stress, or when

$$\frac{d\sigma_T}{d\delta} = \sigma_T \tag{1}$$

where σ_T and δ are true stress and true strain, respectively.

Besides, in uniform plastic strain range, many engineering alloys exhibit an approximately linear relationship between the logarithm of true stress and the logarithm of true strain. For these alloys the relationship between true stress (σ_T) and true strain (δ) may be described by using the Ludwik's equation (Reichel and Dahl, 1983, Ratke and Welch, 1983, and Reichel, 1988), which

$$\sigma_T = \sigma_{0,L} + A_L \delta^n \tag{2}$$

In this equation, A_L is the strength coefficient, n is the strain-hardening exponent, and $\sigma_{0,L}$ is the stress at $\delta = 0$. All these parameters are determined empirically.

Differently from conventional metalic materials, sintered materials are distinguished by their porosity. The effects of pores on mechanical properties of these materials have been intensively investigated and well documented (Haynes and Egediege, 1989, Slesar et al. 1992, Danninger et al. 1993, Palma, 1994, and Christian and German, 1995). Generally, it has been found that an increase in porosity content leads to a decrease in yield stress, ultimate tensile stress, ductility, Young's modulus of elasticity and so on. This effect has been associated to the dependence of the load bearing cross section of porosity, and mainly, due to the internal notch effect of pores.

Although vast literature exists on the effect of porosity on mechanical properties of sintered materials, relatively little attention has been given to the influence of porosity on strain hardening of

Manuscript received: October 1995. Technical Editor: Agenor de Toledo Fleury

these materials. Thus, the object of the present work is to investigate the effects of porosity content on the strain-hardening exponent, and strength coefficients of four differents sintered materials.

Preparation of Testpieces

The raw materials used in this investigation were "Höganäs ASC 100.29" iron powder, Iron-Phosphorus premixe containing 0.6 wt.-% phosphor, copper and graphite elemental powders. Samples of Fe, Fe-Cu, and Fe-C-Cu were made from elemental powders, each one mixed with 0.6 wt.-% lubricant (Mikrowachs). Testpieces of Fe-P were prepared by mixing iron elemental powder with Fe-P-premixe and 0.6 wt.-% lubricant (Mikrowachs). The chemical compositions of these materials are given in Table 1.

The compacting pressure was varied from 390 until 600 MPa in order to obtain as sintered porosities in tensile specimens (Fig. 1) ranging from $P_0 = 3.7$ to 12.5 %, as summarized in Table 2. Sinterization of the specimens was carried out for 30 min at 1150 °C in an atmosphere of cracked ammonia.

Table 1 Chemical Composition of Investigated Materials (wt %)

Material	C	P	Cu	Si	Al	Mn	Cr	Ni	Fe
Fe	0.02	0.01	0.02	0.10	0.05	0.03	0.01	0.02	Bal.
Fe-Cu	0.02	0.01	1.50	0.01	0.01	0.03	0.01	0.02	Bal.
Fe-C-Cu	0.60	0.01	1.55	0.02	0.01	0.03	0.01	0.02	Bal.
Fe	0.003	0.45	0.12	0.13	0.06	0.12	<0.07	0.06	Bal.

Table 2 Porosities of the Materials as Sintered

Material	Porosity P_o (%)			
Fe	3.7±0.2	6.2±0.5	8.8±0.4	12.5±0.7
Fe-Cu	-	6.2±0.3	8.3±0.6	12.1±0.4
Fe-C-Cu	-	5.9±0.2	8.3±0.4	12.3±0.6
Fe-P	-	6.5	9.7±0.3	12.2±0.6

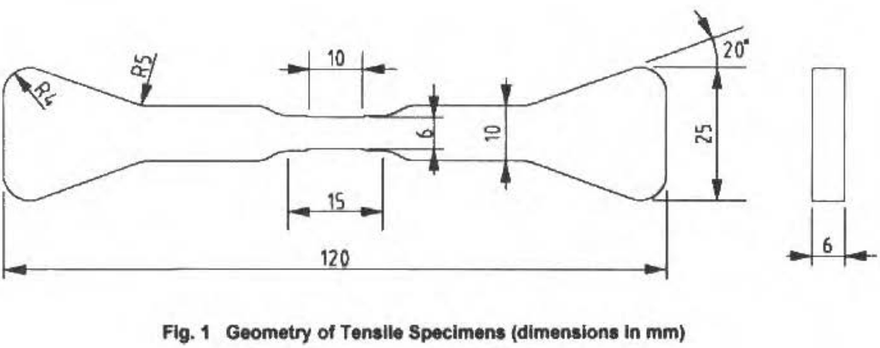

Fig. 1 Geometry of Tensile Specimens (dimensions in mm)

Experimental Procedure

The density (ρ) of sintered specimens was determined from their weight in air and in water. Then, the porosity P_O (as sintered) was determined by using the equation.

$$P_0 = \left(1 - \frac{\rho}{7.87}\right) 100 \tag{3}$$

Tensile tests were carried out on an universal testing machine (100 kN), with a constant cross-head speed of 0.18mm/min, corresponding to a initial strain rate of $2.0 \times 10^{-4}\ s^{-1}$, at room temperature.

Up to seven tensile testpieces of each material and porosity were strain gauged and then pulled to failure. The stress strain curves were recorded in a microcomputer, and the 0.2% offset yield stress was noted.

The true stress σ_T and true strain δ were determined by using

$$\sigma_T = \sigma(1 + \varepsilon_P) \tag{4}$$

and

$$\delta = \ln(1 + \varepsilon_P) \tag{5}$$

where σ is the engineering stress and ε_p the plastic strain.

The true stress-true strain curves were modelled by using Eq. (2), and the strain hardening exponent n and strength coefficient A_L were determined by fitting a best curve through experimental points.

Experimental Results and Discussion

As expected, the 0.2% offset yield stress values ($\sigma_{0.2}$) were found to decrease with increasing porosity, for all investigated materials (Fig. 2).

In Figure 3, the experimental points of iron with porosity $P_O = 3.7$ and 12.5% are plotted together with the stress-strain curves obtained from Eq. (2). It can be seen, that there is a very good agreement between calculated and experimental values. Similar results were obtained making the same type of comparison for Fe-P with $P_O = 6.5$ and 12.5%, as shown in Fig. 4.

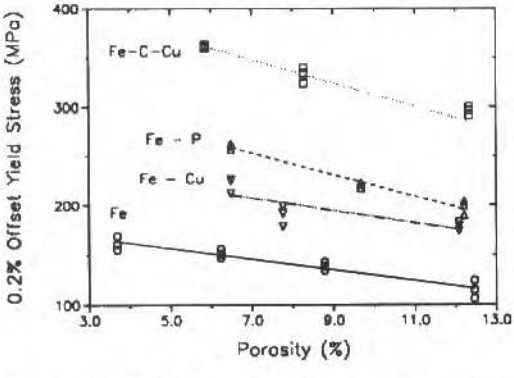

Fig. 2 Effect of Porosity on 0.2% Offset Yield Stress for all Investigated Materials

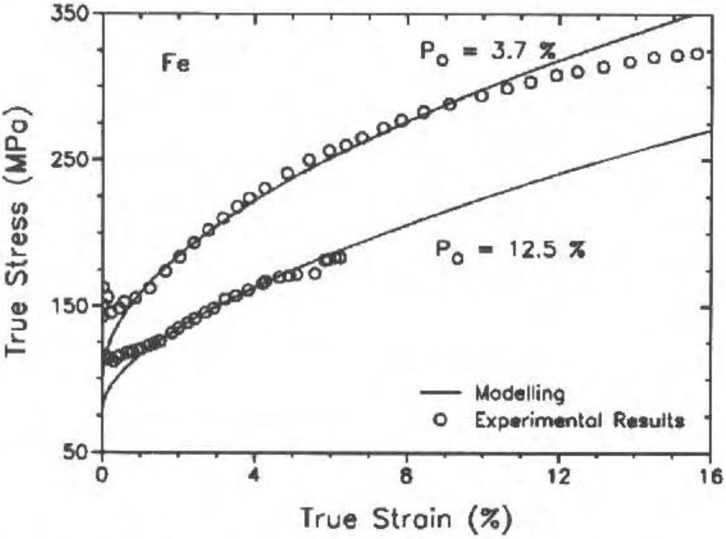

Fig. 3 True Stress-True Strain Curves of Iron and their Modelling by Using Eq. (2)

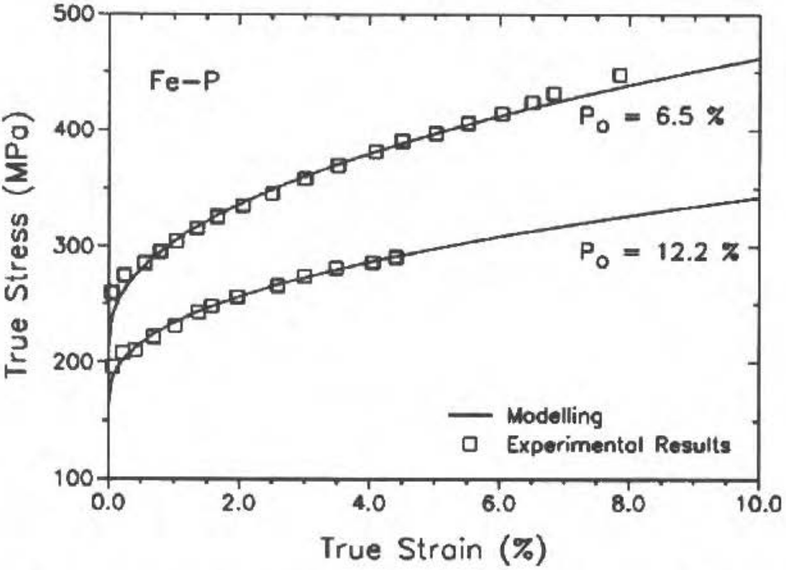

Fig. 4 True Stress-True Strain Curves of Fe-P and their Modelling by Using Eq. (2)

The effects of porosity on strain hardening exponents (n) for all investigated materials are shown in Fig. 5. It can be observed that the strain hardening exponent is pratically independent of porosity, increasing slightly with porosity. These results agree with the findings by Ivashchenko (1984) and Drachinskii (1985), who found n between 0,62 and 0,75 for sintered iron, independently of porosity. According to the explanation of strain hardening exponent given by Reichel (1983), it represents the dependence of average dislocations free way from parameter of matrix as grain boundary, precipitation and dislocation density. Those parameter are pratically independent of porosity, and this could be the reason why n is almost independent of porosity.

On the other hand, the strength coefficients (A_L) are strongly dependent of porosity. As shown in Fig. 6, these coefficients decrease by increasing porosity content.

A comparison between Fig. 2 and Fig. 6 shows a similar behaviour of 0.2% offset yield stress and strength coefficient A_L with the porosity content. The $\sigma_{0.2}/A_L$ rates for all materials were calculated and summarized in Table 3. As can be seen, this rate $\sigma_{0.2}/A_L$ is almost independent of porosity, that is, they are aproximatelly constant for each material.

For the sake of convenience, the results of strain hardening exponents (n) and strength coefficient A_L for all materials and porosities are represented in a tabular form (Table 3)

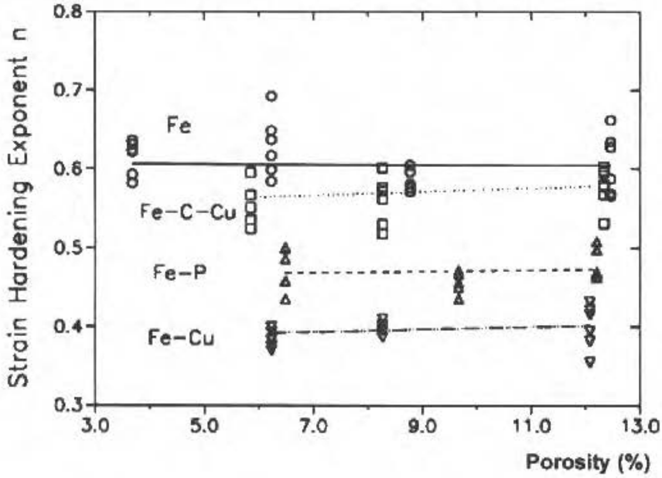

Fig. 5 Influence of Porosity on Strain Hardening Exponent n

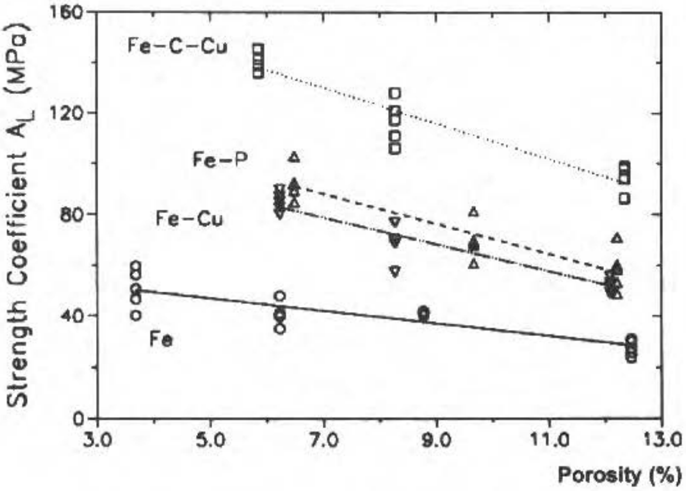

Fig. 6 Influence of Porosity on Strength Coefficient A_L

Table 3 $\sigma_{0.2}/A_L$ Rate, Strain Hardening Exponents and Strength Coefficient for all Materials

	P_O (%)	3.7	6.2	8.8	12.5
Fe	n	0.61	0.63	0.59	0.61
	A_L (MPa)	48.9	43.4	41.2	33.9
	$\sigma_{0.2}/A_L$	3.3	3.5	3.4	3.4
	P_O (%)	-	6.2	6.3	12.1
Fe-Cu	n	-	0.39	0.40	0.40
	A_L (MPa)	-	76.9	66.7	58.9
	$\sigma_{0.2}/A_L$	-	2.9	2.9	3.1
	P_O (%)	-	5.9	8.3	12.3
Fe-C-Cu	n	-	0.58	0.56	0.58
	A_L (MPa)	-	125.1	104.4	91.0
	$\sigma_{0.2}/A_L$	-	3.0	3.2	3.2
	P_O (%)	-	6.5	9.7	12.2
Fe-P	n	-	0.47	0.45	0.48
	A_L (MPa)	-	85.1	71.9	63.9
	$\sigma_{0.2}/A_L$	-	3.1	3.1	3.0

Many empirical relationships between yield stress and porosity are proposed in the literature (Salak et al, 1984, Exner and Pohl, 1978 and Hamiuddin, 1986). As an optimal relationship for 832 test points, Šalak (1984) proposed the empirical relationship

$$\sigma_{0,2} = \sigma_{(0,2),0} \; exp(-CP_0) \qquad (6)$$

where $\sigma_{0.2}$ and $\sigma_{(0.2),O}$ are the 0.2% offset yield stress for porous and pore free materials, respectivelly, and C is a material constant. Since the dependence of strength coefficient A_L and yield stress with porosity content was observed to be the same, one can expect that the relationship

$$A_L = A_{L0} exp(-CP_0) \qquad (7)$$

where A_{Lo} correspond to the strength coefficient of pore free materials, should be approximately true. Therefore, dividing Eq. (2) by $\sigma_{0,L}$, yields

$$\frac{\Delta\sigma}{\sigma_{0L}} = \frac{\sigma_T - \sigma_{0L}}{\sigma_{0L}} = \frac{A_L}{\sigma_{0,L}} \delta^n \qquad (8)$$

If it is assumed that $\sigma_{0,L} \approx \sigma_y$, the yield stress of porous materials, and substituting $\sigma_{0.2}$ by σ_y into Eq. (6) yields

$$\sigma_y = \sigma_{y0} \exp(-CP_0) \tag{9}$$

where σ_{y0} is the yield stress of pore free materials. Substituting Eq. (7) and Eq. (9) into Eq. (8) gives

$$\frac{\Delta\sigma}{\sigma_y} = \frac{\sigma_T - \sigma_y}{\sigma_y} = \frac{A_{L0}}{\sigma_{y0}}\delta^n \tag{10}$$

From Eq. (10) it can be noted that the ratio $\Delta\sigma/\sigma_y$ is independent of porosity, since A_{LO} and σ_{y0} are parameters of pore free materials. This fact can be demonstrated by analysing Fig. 7, where the influence of plastic strain and porosity on the ratio $\Delta\sigma/\sigma_y$ for iron is shown. There is a very good agreement between this Fig. and Eq. (10), i.e., variation in porosity plays no important role, if relative stress is used.

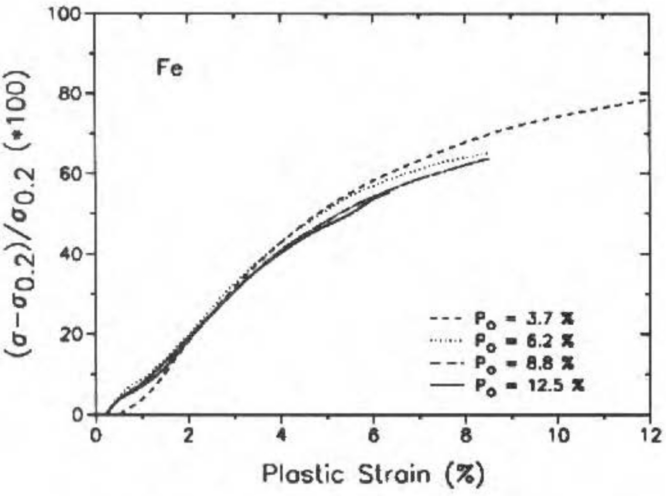

Fig. 7 Rate $\Delta\sigma/\sigma_y$ for Iron With Several Porosities as a Function of Plastic Strain

Finally, it is usually found that strain hardening rate $d\sigma/d\delta$ decreases by increasing porosity content (Klumpp, 1992), which is in complete agreement with the results discussed above. Deriving stress in Eq. (2) with respect to true strain, yields

$$\frac{d\sigma_T}{d\delta} = n A_L \delta^{n-1} \tag{11}$$

showing that strain hardening rate depends not only on the strain hardening exponent n, but also on the strength coefficient A_L. As the latter decreases by increasing porosity, it is also expected that $d\sigma/d\delta$ decreases with porosity.

Conclusions

Studies of sintered ferrous materials, with several different porosities, tensile tested at room temperature have shown that:

- True stress-true strain curves of sintered materials, in uniform strain range, can be described by Ludwik's equation (Eq. (2)) .
- Strain hardening exponent n is almost independent of porosity.
- Strength coefficient A_L and 0.2% offset yield stress decrease by increasing porosity. The rate $\sigma_{0.2}/A_L$ is constant for each material.
- Strain hardening rate $d\sigma_T/d\delta$ decrease by increasing porosity, since it depends on both n and A_L. The rate $d\sigma_T/\sigma$, on the other side, is independent of porosity.

References

Christian, K.D., and German, R.M., 1995, "Relation Between Pore Structure and Fatigue Behavior in Sintered Iron-Copper-Carbon", The Int. J. of Powder Metall., Vol. 31, pp.51-61.

Danninger, H. et al., 1993, "Microstructure and Mechanical Properties of Sintered Iron", Powder Metall. Int., Vol.. 25, Part I: pp.111-117, Part II: pp.170-173.

Drachinskii, A.S. et al., 1985, "Strain Hardening and Failure of Powder Metallurgy Iron", Sov. Powder Metall. Cer., Vol. 10, pp.805-809.

Exner, H.E, and Pohl, D., 1978, "Fracture Behavior of Sintered Iron", Powder Metall. Int., Vol. 19, pp.193-196.

Hamiuddin, M., 1986,"Correlation between Mechanical Properties and Porosity of Sintered Iron and Steels - a Review", Powder Metall. Int., Vol. 18, pp.73-76.

Haynes, R., and Egediege, J.T., 1989, "Effect of Porosity and Sintering Conditions on Elastic Constants of Sintered Irons", Powder Metall., Vol. 32, pp.47-52.

Ivashchenko, R.K. et al., 1984, "Mechanical Properties and Strain Strengthening of Sintered Iron", Sov. Powder Metall. Mat. Ceram., Vol. 23, pp.107-123.

Klumpp, S., 1992,"Quasistatisches und Zyklisches Verformungsverhalten Reiner und Legierter Sintereisenwerkstoffe", (In German), Ph.D. Thesis, IWK 1, University Karlsruhe, R.F. Germany.

Palma, E.S., 1994, "Verformungsverhalten von Sintereisenwerkstoffen bei Einachsig Homogenen und Inhomogenen Beanspruchungen" (In German), Ph.D. Thesis, IWK 1, University Karlsruhe, R.F. Germany.

Petch, N.J., and Armstrong, R.W., 1990, "The Tensile Test", Acta Metall. Mater., Vol. 38, pp.2695-2700.

Ratke, L., and Welch, P., 1983,"The Questionability of Empirical Workhardening Laws", Z. Metallkunde, Vol. 74, pp.226-232.

Reichel, U., and Dahl, W., 1983, "Beschreibung der Fließkurve auf der Basis Phänomenologischer Ansätze am Beispiel Eines Baustahls", Steel Research, Vol. 59, pp. 171-178.

Reichel, U., 1988,"Analyse des Verfestigungsverhaltens von Stählen Anhand Phänomenologischer Modelle", (In German), Ph.D. Thesis, RWTH, University Aachen, R.F. Germany.

Šalak, A. et al., 1974,"The Dependence of Mechanical Properties of Sintered Iron Compacts Upon Porosity", Powder Metall. Int., Vol. 6, pp.128-132.

Slesar, M. et al., 1992, "Plain Porosity as a Microstructural Characteristic of Sintered Materials", Powder Metall. Int., Vol. 24, pp.232-237.

Thomason, P.F., 1990, Ductile Fracture of Metals, Pergamon Press, Oxford, USA.

RBCM - J. of the Braz. Soc. Mechanical Sciences
Vol. XIX - No.1 - 1997 - pp. 80-91

ISSN 0100-7386
Printed in Brazil

Um Estudo do Comportamento Mecânico de Tiras Bimetálicas Submetidas ao Ensaio de Compressão em Estado Plano de Deformações

An Analysis Of The Mechanical Behaviour Of Bimetalic Strips Under The Plain Strain Compression Test

Flávio de Aguiar Araújo
Paulo Roberto Pereira Andery
Horacio Helman
Universidade Federal de Minas Gerais
Escola de Engenharia
Departamento de Engenharia Metalúrgica
30160-030 Belo Horizonte, MG Brasil

Abstract

In this work, a theoretical model describing the mechanical behaviour of bimetalic strips under the plain strain compression test (Ford test), is presented. The model allows to predict the pressure distribution on the tool/strip contact surface, the compression loads and the apparent yield curves of the metals when in the pair, from the knowledge of the yield curves of each metal.

Keywords: Plain Compression Test, Slab Method, Cladding, Ford Test, Bimetalic Composites.

Resumo

É apresentado um modelo teórico para a descrição do comportamento mecânico de chapas bimetálicas submetidas a compressão em estado plano de deformações. O modelo permite a previsão da distribuição de pressões na superfície de contato metal/matriz, as cargas de compressão e as curvas de escoamento dos metais quando ensaiados em conjunto, a partir do conhecimento das curvas de escoamento características de cada metal.

Palavras-Chave: Compressão em Estado Plano de Deformações, Colaminação, Teste Ford, Chapas Bimetálicas.

Introdução

A produção de tiras ou chapas bimetálicas através da colaminação (roll cladding) tem sido objeto de especial atenção nos últimos anos. A maior parte dos pesquisadores tem concentrado sua atenção em aspectos tecnológicos do processo e na análise de parâmetros que influenciam na qualidade e resistência da união. São relativamente escassos os trabalhos na literatura que enfocam aspectos relacionados à resistência dos metais, à interação entre eles e à influência de parâmetros operacionais, tais como atrito, distribuição de pressões ou cálculo das cargas de laminação.

O presente trabalho analisa o comportamento mecânico de pares bimetálicos submetidos ao ensaio de compressão em estado plano de deformações (ensaio Ford).

O ensaio Ford já foi amplamente considerado na literatura, e vários autores o empregaram na determinação das tensões de escoamento de metais (Watts e Ford, 1959, Polakowski, 1949, Altan et al., 1973, Nadai, 1939). A analogia entre o ensaio Ford e a laminação também foi discutida na literatura (Polakowski).

No presente trabalho são analisadas as curvas " tensão x deformação" de pares bimetálicos (antes da união em fase sólida por compressão), e comparadas com as curvas obtidas para cada metal isoladamente. É proposta uma função que caracteriza a interação existente entre os metais, de forma a poder prever-se o comportamento mecânico dos metais no par, a partir do conhecimento das curvas

Manuscript received: August 1996. Technical Editor: Leonardo Goldstein Jr.

" tensão x deformação" características de cada um. A mesma função é empregada no cálculo da distribuição de pressões e cargas de compressão.

Procedimento Experimental

Foram empregados dois conjuntos de materiais: alumínio e cobre, formando um par, e aço e ligas a base de alumínio e estanho (SAE 781 e SAE 783) constituindo o outro par. Os corpos de prova utilizados nos ensaios de compressão tinham 30 mm de largura, 150 mm de comprimento e espessura variável. Os indentadores utilizados tinham 4,0 mm de largura, e seguiu-se o procedimento para ensaio oportunamente descrito (Andery e Helman, 1992).

Os ensaios foram realizados em uma máquina MTS 810 , servo-hidráulica, com aquisição computadorizada de dados. Para a avaliação das deformações plásticas nos ensaios realizados com cada metal individualmente, foram utilizadas as inclinações médias das retas de carregamento e descarregamento (parte linear das curvas). A aplicação de carga foi monotonicamente crescente, com velocidade de carregamento e descarregamento controlada, e aquisição contínua de dados. As superfícies de contato dos corpos de prova com os indentadores foram lubrificadas com bissulfeto de molibdênio.

Nos ensaios realizados em pares metálicos , as superfícies de contato entre os metais foram lixadas e escovadas, e os corpos de prova foram superpostos. Valores distintos de carga foram aplicados em regiões diferentes dos corpos de prova assim constituídos. As espessuras finais de cada metal do corpo de prova foram medidas após descarregamento, utilizando-se micrômetro, sendo registrada a relação "tensão x deformação" para cada ensaio.

A curva " tensão x deformação" obtida para cada metal ensaiado no par ou individualmente foi aproximada através de uma função na forma da expressão de Ludwick, e para cada ponto da curva a discrepância entre a expressão obtida e os valores reais foi sempre inferior a 5%.

Resultados e Discussão

Comportamento dos Materiais nas Curvas "Tensão x Deformação"

As Figuras 1 e 2 mostram curvas típicas " tensão x deformação" obtidas nos ensaios. As curvas obtidas para cada metal isoladamente são comparadas com as obtidas nos ensaios do par (corpo de prova composto).

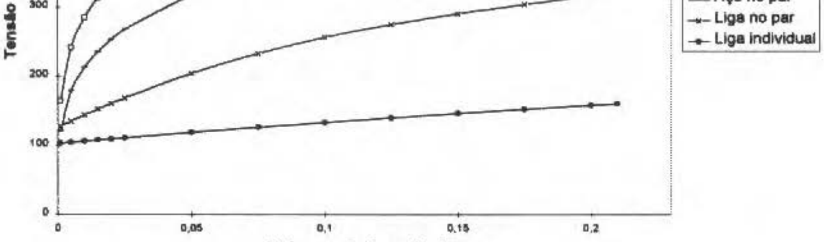

Fig. 1 Curvas Típicas "Tensão x Deformação", para os Metais Ensaiados Individualmente e no Par (Aço e Liga)

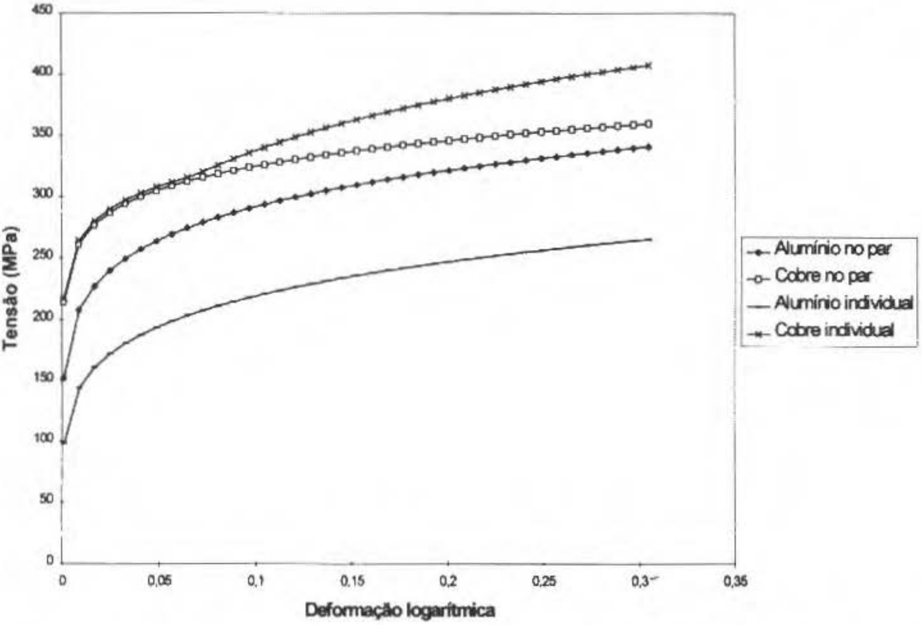

Fig. 2 Curvas Tipicas "Tensão x Deformação", para os Metais Ensaiados Individualmente e no Par (Cobre e Alumínio)

Em todos os casos estudados, observou-se que quando os metais são ensaiados em conjunto, ocorre uma alteração em relação a seu comportamento mecânico, obtido nas curvas dos metais ensaiados individualmente. O metal mais duro, ensaiado no par, apresenta menores níveis de tensão, para uma dada deformação, quando comparado com sua curva de escoamento característica. Inversamente, o metal mais macio apresenta maiores níveis de tensão, quando sua curva de escoamento é comparada com a obtida do metal ensaiado individualmente.

Devido à tendência do metal mais macio escoar mais rapidamente e com menores níveis de tensão que o metal mais resistente do par, e pelo fato de que as tensões cisalhantes resultantes do atrito na interface entre eles se opõem a essa diferença de velocidades, estabelece-se um estado de tensões de compressão no metal mais macio, e de tração no metal mais resistente. Observa-se assim um efeito de "arrastamento" de um metal sobre o outro e como conseqüência, altera-se a resistência dos metais no par, de modo que o mais macio comporta-se como se fosse mais resistente, enquanto que o metal mais resistente do par apresenta tensões de escoamento mais baixas.

Esse comportamento, resultante da interação entre os metais, é semelhante ao relatado na literatura no caso de extrusão hidrostática de pares bimetálicos (Helman, 1978), ou na laminação em "sandwich" de metais de alta resistência (Arnold e Witton, 1959; Kiuchi, 1990; Weinstein e Pawelski, 1968).

Para caracterizar a tensão de cisalhamento "τ" (denominada aqui "tensão de arraste") que aparece na interface entre os metais, como resultado da diferença entre seus comportamentos mecânicos, assumiu-se que essa tensão seja função da relação entre as tensões de escoamento por cisalhamento características de cada metal. Ou seja:

$$\tau = \tau(\alpha) \tag{1}$$

sendo $$\alpha = K_s / K_h \tag{2}$$

onde K_s e K_h são as tensões de escoamento por cisalhamento do metal mais macio e do mais resistente respectivamente, obtidas através das curvas de escoamento dos metais ensaiados isoladamente.

Para estudar a relação funcional entre τ e α propõe-se uma função, que será denominada "função de arraste" (ϕ), que obedeça as seguintes condições:

- $\tau = 0$ quando $K_s = 0$,ou seja, o metal mais macio comporta-se como um fluido ideal, não apresentando resistência à deformação por cisalhamento;
- $\tau = 0$ quando $K_s = K_h$, ou seja, os dois metais são mecanicamente equivalentes e
- $\tau = K_s$ quando K_h corresponde a um metal que pode ser considerado como rígido em relação a K_s. Nestas condições, a tensão de cisalhamento na interface atinge o seu valor limite, igual a tensão de escoamento por cisalhamento do metal mais macio do par.

A partir dessas condições foi proposta uma relação na forma:

$$\tau = q \ \phi \ K_s \qquad (3)$$

onde

$$\phi = (\alpha - \alpha^2)^{\alpha} \qquad (4)$$

e q é uma constante, a ser determinada experimentalmente.

A tensão de cisalhamento na interface entre os metais, caracterizada pela função de arraste descrita acima, é responsável pelo decréscimo no nível de tensões da curva do metal resistente, e pelo acréscimo no nível de tensões da curva do metal mais macio. A partir da condição de equilíbrio para as forças nos corpos de prova submetidos em conjunto à indentação plana, foi calculado o decréscimo no nível de tensões δ_h que o metal mais resistente sofrerá quando ensaiado no par, para uma dada deformação externa aplicada, e o acréscimo no nível de tensões δ_s a que estará submetido o metal mais macio, nas mesmas condições (Andery e Helman, 1992).

Esses valores foram calculados como sendo :

$$\delta_s = q\, b\, S_s\, (\alpha - \alpha^2)^{\alpha} / 4\, h_s \qquad (5)$$

$$\delta_h = q\, b\, S_s\, (\alpha - \alpha^2)^{\alpha} / 4\, h_h \qquad (6)$$

onde b é a largura do indentador, S_s a tensão de escoamento do metal mais macio, em estado plano de deformações, e h_h e h_s as espessuras instantâneas do material mais resistente e do mais macio do par, respectivamente, para os diferentes valores da força de compressão aplicada ao conjunto.

Determinou-se experimentalmente que a deformação verdadeira de cada metal no par obedece uma relação aproximadamente linear com a deformação total imposta ao conjunto. Dessa forma, é possível escrever:

$$\varepsilon_s = A + B \ \varepsilon_t \qquad (7)$$

$$\varepsilon_h = A^* + B^* \varepsilon_t \qquad (8)$$

onde A, A*, B e B* são constantes obtidas por regressão linear, ε_s e ε_h são as deformações verdadeiras de cada metal do conjunto e ε_t a deformação verdadeira total do bimetal. Essa constatação tem suporte na literatura (Yahiro, 1991). A Figura 3 ilustra, a título de exemplo, o comportamento das deformações de cada metal em função da deformação total, conforme definido acima, para um dos pares aço/liga estudados.

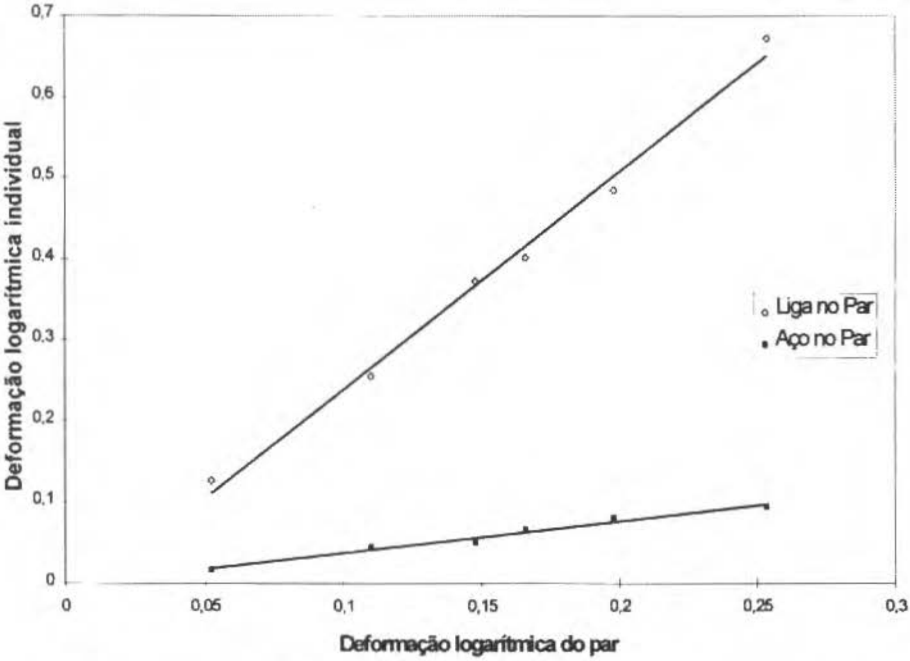

Fig. 3 Deformação de cada Metal do Par em Função de Deformação Total Imposta ao Conjunto

Dessa forma, a partir de uma deformação total do par, é possível determinar as deformações de cada metal, as suas espessuras e, consequentemente, os valores de δ_s e δ_h conforme definidos acima.

Para uma deformação externa aplicada ao par, e conhecendo pelas relações (7) e (8) as espessuras individuais dos metais, correspondentes a um valor determinado da carga de indentação, tem-se:

$$S_{sp}(\varepsilon) = S_{si}(\varepsilon) + \delta_s(\varepsilon) \tag{9}$$

$$S_{hp}(\varepsilon) = S_{hi}(\varepsilon) - \delta_h(\varepsilon) \tag{10}$$

onde S_{hp} e S_{sp} são as tensões, para uma dada deformação, dos metais ensaiados em conjunto, correspondentes a um valor de carga aplicada, e S_{hi} e S_{si} as tensões , para as mesmas deformações, correspondentes à curva de escoamento característica de cada metal, quando ensaiado isoladamente.

Em resumo, a utilização das Eqs. (9) e (10) para distintos valores de carga, correspondentes a distintos valores da deformação ε_t aplicada ao par, possibilita o conhecimento das curvas "tensão x deformação" dos metais no par, a partir do conhecimento das curvas de escoamento de cada metal ensaiado individualmente, sendo a diferença no seu comportamento mecânico originada pela tensão de arraste descrita acima.

As Figuras 4 e 5 ilustram as curvas "tensão x deformação" para os pares aço/liga e cobre/alumínio ensaiados em conjunto. As curvas experimentais obtidas são comparadas com as curvas cujos valores de tensão foram calculados pelo procedimento acima. Observa-se uma razoável concordância entre valores teóricos e experimentais , com erros relativos inferiores a 10%. No cálculo dos valores de δ_s e δ_h utilizou-se valores médios do coeficiente q , calculados em função da comparação entre os valores reais e os calculados.

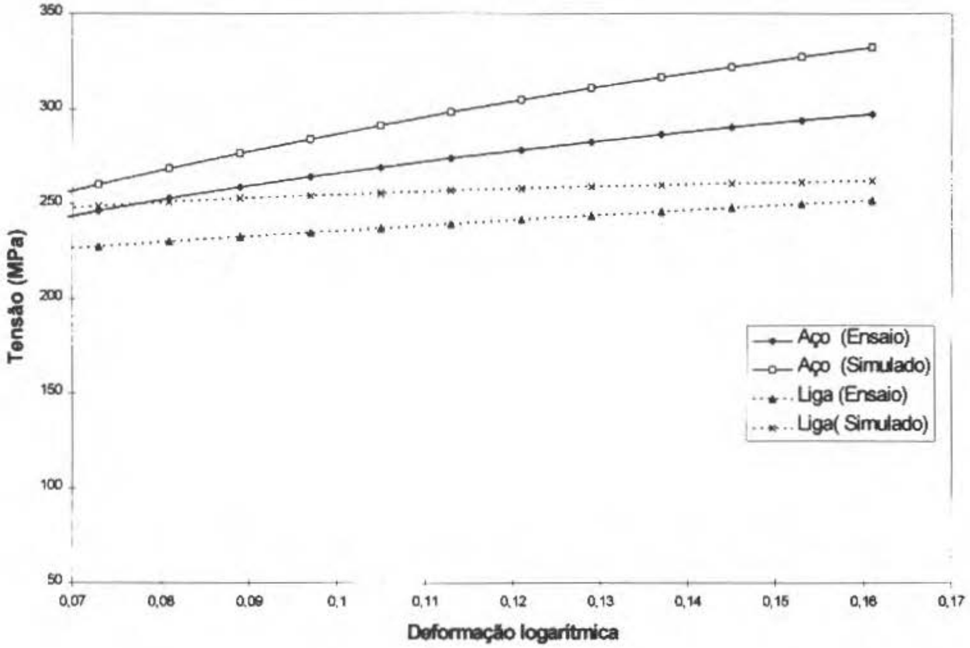

Fig. 4 Curvas "Tensão x Deformação" para os Metais Ensaiados em Conjunto (Aço/Liga).

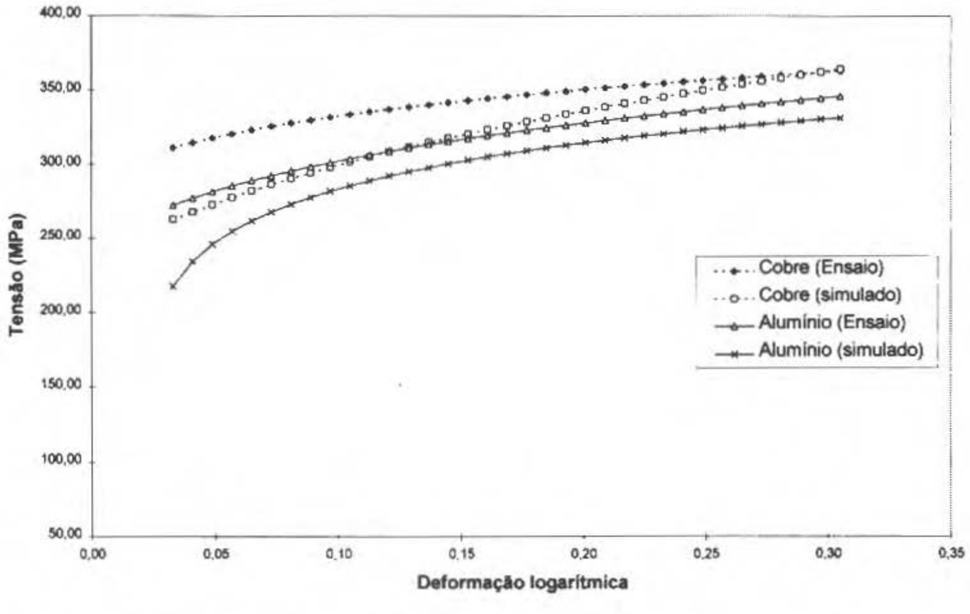

Fig. 5 Curvas "Tensão x Deformação" para os Metais Ensaiados em Conjunto (Cobre/Alumínio).

A simulação das curvas de escoamento dos metais levando em conta a interação entre eles permite avaliar o seu comportamento mecânico durante o processo de conformação, em condições de estado plano de deformações, e possibilita o cálculo da distribuição de pressões e cargas durante a indentação.

Previsão da Distribuição de Pressões e Cargas de Indentação

A partir de uma análise feita utilizando o método dos blocos, foi possível determinar a distribuição de pressões durante a indentação e, integrando a colina de atrito, a carga aplicada. Foram feitas as hipóteses habituais pertinentes ao método dos blocos e um esquema das tensões consideradas e convenções adotadas é mostrado na Fig. 6.

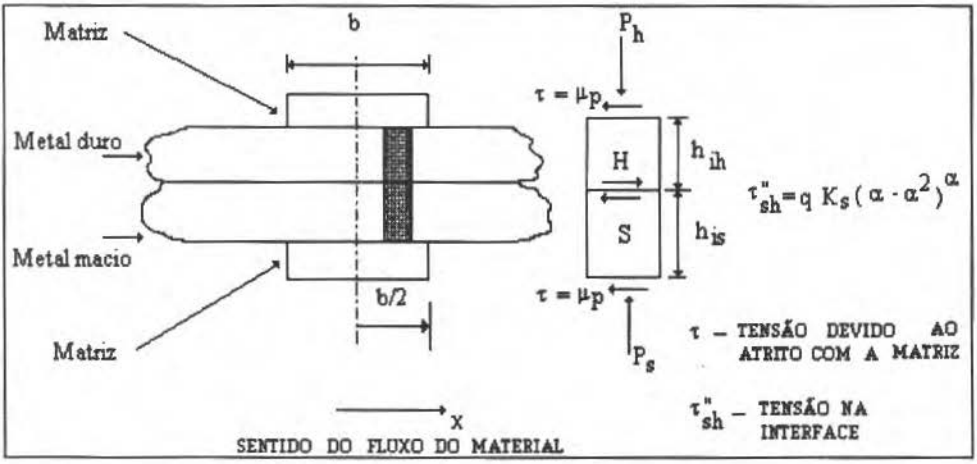

Fig. 6 Esquema Mostrando as Convenções Empregadas e Tensões, para Análise Através do Método dos Blocos

Foram assim obtidas as seguintes equações:

$$P_s(x) = q\,\frac{K_s}{\mu_s}(\alpha-\alpha^2)^\alpha\,((1+(S_{si}/(q\,(K_s/\mu_s)\,(\alpha-\alpha^2)^\alpha))\\ \times \exp(\mu_s/h_s)\,(b/2-x)-1 \tag{11}$$

$$P_h(x) = q\,\frac{K_h}{\mu_h}(\alpha-\alpha^2)^\alpha\, 1-(1-(S_{hi}/(q\,(K_s/\mu_h)\,(\alpha-\alpha^2)^\alpha)\\ \times \exp(\mu_h/h_h)\,(b/2-x) \tag{12}$$

onde S_s é a tensão de escoamento do metal menos resistente, S_h a tensão de escoamento do metal mais resistente K_s, a tensão de escoamento por cisalhamento do metal mais macio, h_i e h_h as espessuras instantâneas, b a largura do indentador, μ_s e μ_h os coeficientes de atrito na interface entre cada metal e o indentador e $p_s(x)$ e $p_h(x)$ são as pressões agindo sobre o metal mais macio e o metal mais resistente do par, em função da posição considerada ao longo da largura do indentador. Assumiu-se o modelo coulombiano para as tensões de atrito.

Para o cálculo das cargas de indentação foram empregas as expressões:

$$P_s = 2\,w\,q\,\frac{K_s}{\mu_s}.(\alpha-\alpha^2)\alpha\left[1+\frac{S_{si}}{(qK_s/\mu_s)(\alpha-\alpha^2)\alpha}\right] \\ \times\frac{h_s}{\mu_s}(exp((\mu_s/h_s)(b/2))-1)-wbq\frac{K_s}{\mu_s}(\alpha-\alpha^2)\alpha \qquad (13)$$

$$P_h = w\,b\,q\frac{K_s}{\mu_h}(\alpha-\alpha^2)\alpha\;1+2q\frac{K_s}{\mu_h}(\alpha-\alpha^2)\alpha \\ \times w\left[1-\frac{S_{hi}}{(qK_s/\mu_h)(\alpha-\alpha^2)\alpha}\right]h_h\,(1-exp((\mu_h/h_h)(b/2)) \qquad (14)$$

resultantes da integração das expressões (11) e (12), P_s é o valor da carga no metal mais macio e P_h é a carga no metal mais resistente.

Nas hipóteses feitas inicialmente para a análise por meio do método dos blocos não foram estabelecidas condições que assegurem a igualdade entre as cargas de compressão calculadas em ambos os lados da interface entre os metais. O fator q nas equações acima é selecionado de forma tal que, embora com diferentes distribuições de pressões para cada metal, as cargas de indentação resultantes da integração das colinas de atrito de cada metal sejam iguais. Foram considerados como parâmetros de cálculo as espessuras iniciais e a espessura final obtida para o par, correspondente a um determinado valor de carga.

A Tabela 1, abaixo, mostra os parâmetros de ensaio e os resultados obtidos para três dos casos estudados:

Tabela 1 Valores de Carga Reais e Calculados para Dois Casos

Caso	Par	Espessura Inicial [mm]		Espessura Final [mm]		Coeficiente de Atrito	
		Duro	Mole	Duro	Mole	Duro	Mole
1	Cu/Al	2,12	2,98	1,688	0,925	0,05	0,05
2	Aço/Liga	1,97	2,27	1,95	1,865	0,01	0,01
3	Aço/Liga	1,98	0,83	1,32	0,41	0,01	0,01

Caso	Carga Real [kfg]	Carga Calculada [kgf]		Diferença Percentual	Erro Mole [%]	Erro Duro [%]
		Mole	Duro			
1	5390	5808	5691	2,07	7,75	5,3
2	2530	2622,2	2622,3	0,003	3,65	3,64
3	6000	6431,2	6431	0,003	7,19	7,18

onde a diferença percentual é dada por $[(P_h - P_s)/P_s] \times 100$ e os erros por $[(P - P_{real} / P_{real}] \times 100$, sendo P_{real} a força de compressão medida no ensaio.

A Figura 7 mostra as distribuições de pressões para o primeiro caso apresentado. Como as deformações dos dois materiais foram tais que as tensões de escoamento resultaram em valores próximos entre si, com parâmetro $\alpha = 0{,}967$, o efeito do arraste na interface foi menos pronunciado. Os valores das cargas calculados mostram razoável concordância com os valores obtidos nos ensaios.

As Figs. 8 e 9 mostram as distribuições de pressões obtidas para os casos 2 e 3 da Tabela 1 acima.

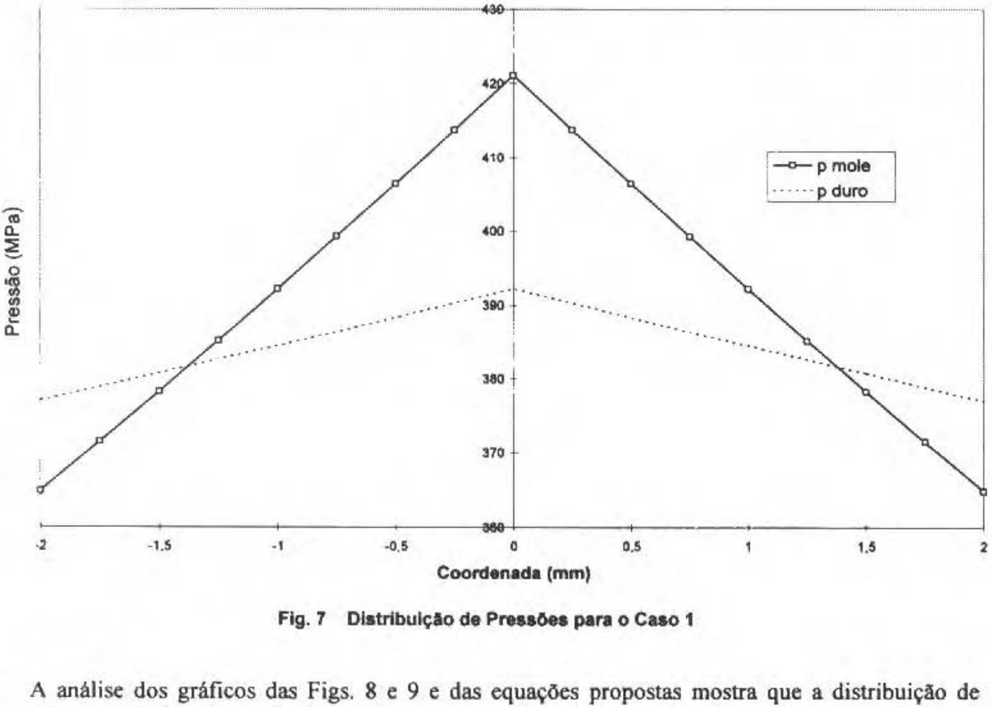

Fig. 7 Distribuição de Pressões para o Caso 1

A análise dos gráficos das Figs. 8 e 9 e das equações propostas mostra que a distribuição de pressões no metal mais macio do par tem o comportamento esperado, observado nos ensaios Ford convencionais, acrescendo-se o efeito da tensão de arraste na interface, que age no mesmo sentido da tensão de atrito, como resultado da interação entre os metais. Por outro lado, o metal mais resistente do par apresenta um comportamento distinto. Com efeito, as pressões atingem um valor máximo nas bordas e um valor mínimo no centro, devido ao efeito dessa mesma tensão de arraste, que nesse caso, age em sentido oposto as tensões de atrito. Nesses casos o efeito dessa interação entre os metais é aparentemente mais significativo, a ponto de inverter o formato da colina de atrito resultante da indentação.

Os valores encontrados para as cargas de indentação, quando comparados com os valores obtidos experimentalmente, resultam em erros relativos muito pequenos nos casos 2 e 3. Na análise de outros casos observou-se erros relativos inferiores a 10 % para valores de α variando entre 0,65 e 0,75. Nos ensaios realizados, foram encontrados erros maiores para valores de α fora dessa faixa. O conjunto de dados experimentais disponíveis não permite concluir que exista uma tendência de um ajuste melhor das equações para determinados valores das relações entre as tensões de escoamento.

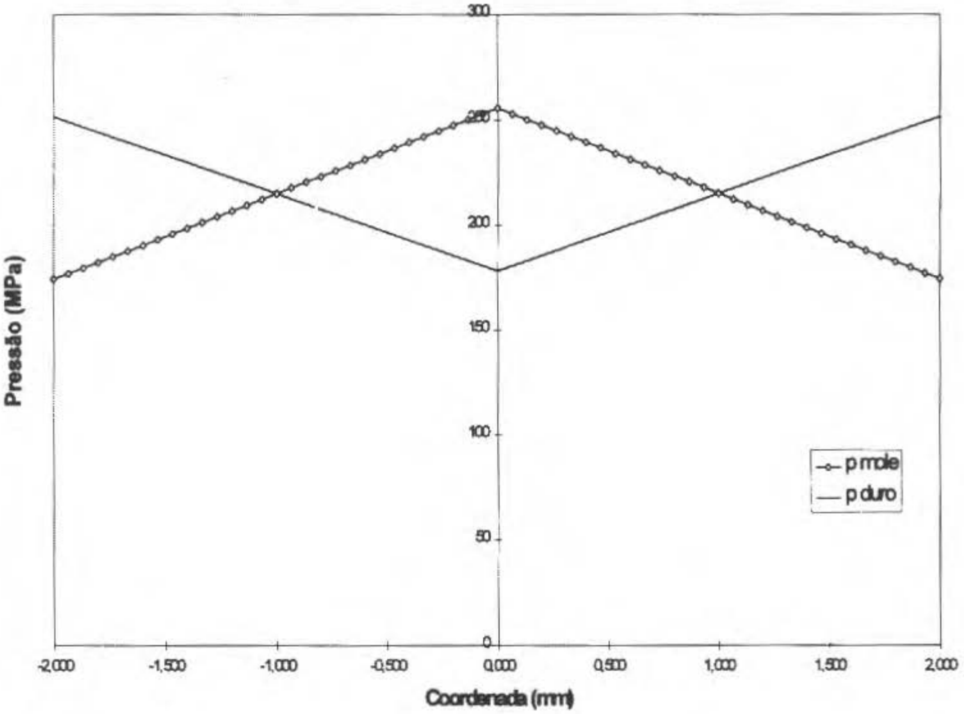

Fig. 8 Distribuição de Pressões para o Caso 2

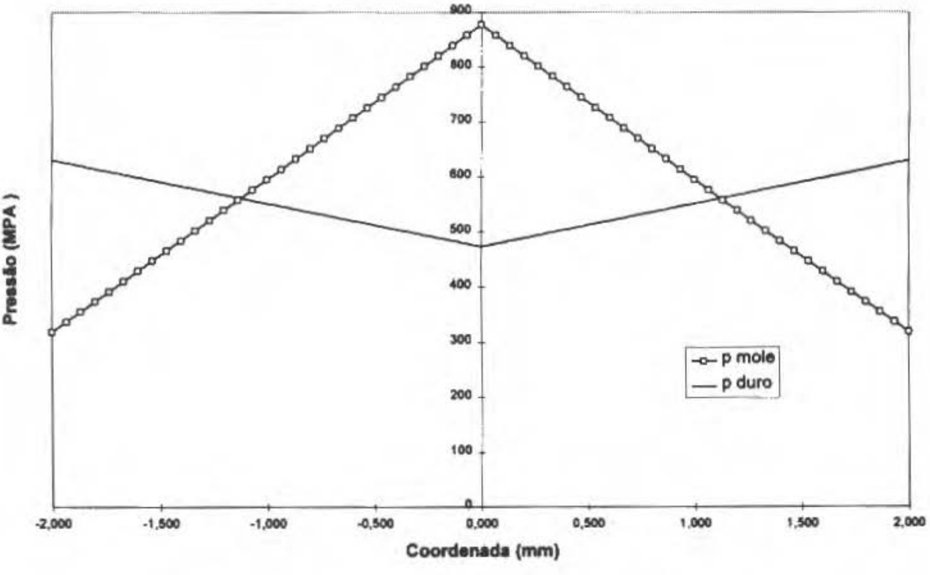

Fig. 9 Distribuição de Pressões para o Caso 3

Previsão da Distribuição de Espessuras

No estudo da compressão em estado plano de deformações de tiras bimetálicas espera-se respostas sobre a distribuição de deformações e as espessuras finais obtidas para cada metal do par, em função de uma força externa aplicada. Essa análise é fundamental, uma vez que é necessário conhecer a relação de espessuras dos metais nos pares a serem utilizados industrialmente.

O critério utilizado foi o da determinação, através de um processo iterativo, das espessuras de cada metal que permitem a igualdade entre as cargas de compressão calculadas para os dois metais em cada lado da interface metal/matriz. Em cada iteração, a soma das espessuras dos metais tem de ser igual a espessura do par, previamente estabelecida.

Para coeficientes de atrito previamente fixados, determinou-se o fator q das Eqs. (13) e (14) que permitissem essa igualdade entre as cargas.

A Tabela 2 abaixo mostra os resultados obtidos para dois dos casos do par aço/liga estudados.

Tabela 2 Distribuição de Espessuras dos Metais do Par

Caso	Espessura Inicial Real [mm]		Espessura Final Real [mm]		Coeficiente de Atrito	Fator de Arraste
	Aço	Liga	Aço	Liga		
1	1,97	2,27	1,95	1,865	0,01	2
2	1,98	0,83	1,92	0,66	0,01	1

Caso	Espessura Final Calculada [mm]		Erros Relativos % (Espessuras)		Cargas Calculadas (kgf)		Erro Relativo [%]	
	Aço	Liga	Aço	Liga	Aço	Liga	Aço	Liga
1	1,958	1,857	0,4	0,44	2446,7	2423,9	3,3	4,2
2	1,954	0,626	1,78	5,2	2964,5	2968	2,7	2,8

A análise dos resultados para os casos apresentados e para os outros casos estudados mostra uma boa concordância entre as espessuras finais calculadas quando comparadas com as espessuras reais obtidas dos ensaios.

Conclusões

Foi proposto um modelo para descrever a interação entre dois metais ensaiados em conjunto, em compressão em estado plano de deformações. O modelo permite uma razoável aproximação das curvas "tensão x deformação" dos metais no par, a partir das curvas dos metais ensaiados individualmente, bem como a avaliação da distribuição de pressões e cargas de indentação.

Por outro lado, o modelo permite uma razoável previsão das espessuras finais de cada metal no par indentado, a partir do conhecimento das curvas de escoamento características de cada metal, da carga aplicada e da espessura final do conjunto.

Referências

Andery, P., e Helman, H., 1992, "O ensaio de Compressão Plana no Estudo da Colaminação de Metais Diferentes", Anais do Simpósio de Conformação Plástica dos Metais, São Paulo, SP.

Altan, T., e Bougler, F.W., 1973, "Flow Stresses of Metals and Its Application in Metal Forming Analyses", Journal of Engineering for Industry, Asme Transactios, pp. 1009-1019.

Arnold, W., e Witton, P.W. , 1959, "Stress and Deformation Studies for Sandwich Rolling of Hard Metals", Institution of Mechanical Engineers, Proceedings, Vol. 173, N.8, pp. 241-256.

Helman, H., 1978, "Análise da Produção de Barras Bimetálicas por Extrusão Hidrostática Atráves do Método dos Blocos, Metalurgia ABM, Vol. 34, N.8, pp. 481-487.

Kiuchi, M., 1990, "Mathematical Simulation of Complex Asymetricall Rolling of Clad Sheets and Sandwich Sheets", Transactions of Namri/ SME.

Nadai, Al Pittsburgh, P.A., 1939 "The Forces Required for Rolling Steel Under Tension", Journal of Applied Mechanics, Vol. 6, pp. 54-62.

Polakowski, N.H., 1949, "The Compression Test in Relation to Cold Rolling", Journal of the Iron and Steel Institute, 1949, pp. 250-276.

Roldán, Alberto, 1993, Dissertação de Mestrado, Depto. Eng. Metalúrgica, UFMG.

Watts, B., e Ford, H., 1959, "An Experimental Investigation of the Yielding of Strip Between Smooth Dies", British Welding Journal, Vol. 6, N.6, pp. 13-28.

Weinstein, A., e Pawelski, O., 1968, "Plane Strain Drawing of Sandwiched Metals", Proc. 8th International MTDR Conference, Pergamon Press.

Yahiro, A., et al., 1991, "Development of Non Ferrous Clad Plate and Sheet by Warm Rolling with Different Temperature of Materials" I.S.I.J. International, Vol. 31, N.6, pp. 647-454.

RBCM - J. of the Braz. Soc. Mechanical Sciences
Vol. XIX - No.1 - 1997 - pp. 92-103

ISSN 0100-7386
Printed in Brazil

Hydrogen Damage Analysis in Catalytical Cracking Units Steels of Petroleum Refineries by Scanning Electron Microscopy

Marcos Baroncini Proença
Célia Marina de Alvarenga Freire
Cláudia Aoki
Universidade Estadual de Campinas
Faculdade de Engenharia Mecânica
Departamento de Materiais
13083-970 Campinas, SP Brasil

Abstract

Corrosion of vessels and piping made of steel by sour water in catalytical cracking units of petroleum refineries generate atomic hydrogen. Large part of this hydrogen will go to the atmosphere as H_2, a fraction will diffuse in the steel lattice and stay in the defects, while the balance will diffuse through the lattice. The most well known effect in these steels is blistering and cracking induced by the retained fraction of hydrogen. In this work scanning electron microscopy was used to identify the damage caused by hydrogen and the damage susceptibility of two steels commonly used in catalytical cracking vessels.

Keywords: Hydrogen Damage, Scanning Electron Microscopy, Catalytical Cracking Vessel Steel.

Introduction

One of the biggest problems found in petroleum refineries is controlling hydrogen damage in steels used in catalytical cracking vessels and piping (Strong, Magestic, Wilhelm, 1991 ; Ehmke, 1991 ; REPLAN 0024). Hydrogen damage may be classified into four distinct types: hydrogen blistering, hydrogen embrittlement, decarburization and hydrogen attack (Fontana,1987). Hydrogen blistering is the most prevalent in the petroleum industry and results from the penetration of hydrogen into the steel wall of a vessel containing an eletrolyte, and exposed to the atmosphere.

Hydrogen evolution occurs on the inner surface as a result of corrosion; at any time there is a fixed concentration of hydrogen atoms on the steel surface, some of which diffuses into the steel and forms hydrogen molecules on the exterior surface. However , if the hydrogen atoms diffuse into a void, they combine into molecular hydrogen and cannot keep difusing, consequently increasing the concentration and pressure of hydrogen gas within the void. The equilibrium pressure of molecular hydrogen in contact with atomic hydrogen is several hundred thousand atmospheres, resulting in local deformation and , in an extreme condition, in the complete destruction of the vessel wall. Hydrogen embrittlement is also present in petroleum refineries, caused by penetration of hydrogen into a steel, with a resulting loss of ductility and of tensile strength. The exact mechanism of hydrogen embrittlement is not as well known as for hydrogen blistering. However, the initial cause is the same , that is, the diffusion of atomic hydrogen into de steel latice. Most of the explanation that have been proposed for the hydrogen embrittlement mechanism are based on the phenomenon of slip interference by dissolved hydrogen, problably due to the accumulation of these hydrogen near dislocation sites or microvoids. If the absortion is due to contact with hydrogen gas, the hydrogen embrittlement is often called as hydrogen stress cracking. If the hydrogen is absorbed because of corrosion the embrittlement is called stress corrosion cracking or, eventually, hydrogen stress cracking. If corrosion is due to the presence of hydrogen sulfide, a common term in use is sulfide stress cracking. Decarburization is most often produced by moist hydrogen at high temperatures, and lowers the tensile strength of steel as a result of removing carbon from the steel. Hydrogen attack refers to the interaction between hydrogen and a component of an alloy at high temperatures.

Metalographic analysis and local inspection in refineries indicate that the damage mechanisms include corrosion involving hydrogen entrance into the steel structure and stress corrosion cracking. The prevalence of the embrittlement in catalytical cracking units is estimated to happen in about 30 to

Manuscript received: June 1996. Technical Editor: Leonardo Goldstein Jr.

40 percent of all equipment (Alefeld, 1978). Embrittlement and blistering in steels used in piping and vessels was indicated in a REPLAN - Refinaria do Planalto Central, inspection report (REPLAN 0024) concerning the catalytical cracking unit vessels V-22503, wich operate at a temperature of 53°C and a pressure of 1.20 kgf/cm^2, and V-22508, at 34°C and 17.00 kgf/cm^2. Corrosion engineers have focused their efforts in corrosion prevention of these vessels and piping steels by corrosion control programs and repair techniques, where is mainly indicated the use of inhibitors as sodium and ammonium polyssulfides, and by material selection (Strong, Magestic, Wilhelm, 1991 ; Edmondson, Rue, 1992). Recently, there have been a move to substitute ASTM 285 steels for ASTM 516 steels in catalytical cracking units, because the ASTM 516 steel is a silicon-killed steel, without internal stresses,or residual stresses, wich favors corrosion and hydrogen damage. There is, however, few information published about the microscopic evaluation of hydrogen damage in equipments as well as concerning the behavior of these steels. In this work scanning electron microscopy was used to identify the damage caused by hydrogen in ASTM 285 and ASTM 516 hydrogenated samples, and to evaluate their susceptibility.

Methodology

The analysis of hydrogen damage was made by scanning electron microscopy of the samples of ASTM 285 grade G and ASTM 516 grade 70 steels, whose nominal composition are presented in Tables 1 and 2. The samples were laminated in a four rolls laminator until a thickness of 500μm and annealed in vacuum.

Table 1 Nominal Composition of ASTM 516 Grade 70 Steel

Elements	Content (%)
C_{max}	0.27
Mn	0.85-1.20
P_{max}	0.035
S_{max}	0.04
Si	0.15-0.40

Table 2 Nominal Composition of ASTM 285 Grade G Steel

Elements	Content (%)
C_{max}	0.28
Mn	0.90-0.98
P_{max}	0.035
S_{max}	0.040
Si	-------

Samples Hydrogenation

According to the double potentiostatic method the sample, situated as a ion permeable membrane between two compartments of a double electrolytic cell, was connected to a programable multichannel electrochemical interface. Each of these compartments constitute an electrochemical cell, with the working electrode being the sample, the reference electrode a saturated calomel electrode and the counter electrode, platinum. At one side of the double cell, sample hydrogenation was promoted while in the other was detected the hydrogen diffused throughout the sample. The measurements made were converted into plots of I (current), or E (tension), as a function of time, from which were obtained the hydrogen diffusion coefficient as well as the hydrogen solubility and permeability in the sample.

In this work this technique was used only to promote the hydrogenation of the samples wich were, in sequence, analyzed by scanning electron microscopy. The hydrogenation was done with a current density of 5mA/cm^2 and a potential of 0V oc (open circuit), with a sample exposed surface of 1 cm^2, with a NaOH solution (0.1N) in both sides of the double electrolytic cell , at room temperature and pressure, in a programmable multichannel electrochemical interface model GALVPOT GP 2001H by TAI (Tecnologia Aplicada à Indústria) developed in the Hydrogen Laboratory of COPPE/UFRJ. The entire system was monitored through this interface (Proença, Freire, Santos, Arantes, 1996).

Scanning Electron Microscopy Analysis

The scanning electron microscopy is a powerful technique to analyze and characterize heterogeneous organic and inorganic materials, in microscopic and sub-microscopic scales, with good precision. In this technique an electron beam acts on the sample surface producing secondary and primary electrons, Auger electrons and fotons at various energy levels, wich can be detected and analyzed. The secondary electrons wich are emitted constitute one of the most important emissions for scanning electron microscopy because they allow observing, with good precision, topographic differences in sample surfaces (Goldstein, 1992).

In this work the hydrogenated samples were covered with a thin gold film to improve image resolution, and analyzed using a JXA-840 A electron probe microanalyzer from JEOL. This microanalyzer scanning resolution is up to 4.0 nm for a working distance of 8 mm, and up to 10 nm for a working distance from 4 to 39mm . The image size amplification range is from 10 to 300000 times. It is made of a tungsten filament cathode and anodes at two vertical adjustable positions. Secondary electron emission was used because it is recommended for allowing better observation of the hydrogen caused damages on the samples surfaces.

Results and Discussion

Figures 1 to 17 show the damages caused by hydrogen in the ASTM 285 grade G and ASTM 516 grade 70 samples.

Figures 1 and 2 show blistering wich is brought about by atomic hydrogen diffused throughout the ASTM 285 sample crystalline structure when they encounter void spaces. In these spaces there is an increasing tension, which becomes sufficient to give atomic hydrogen the needed energy to generate molecular hydrogen. These larger hydrogen molecules which are generated become trapped, causing the void space to accumulate hydrogen, rising the void internal tension, that can become larger than the one corresponding to the steel elastic strain , causing plastic deformation and fissures. The same phenomenon can be observed in Figs. 3 and 4,for the ASTM 516 sample.

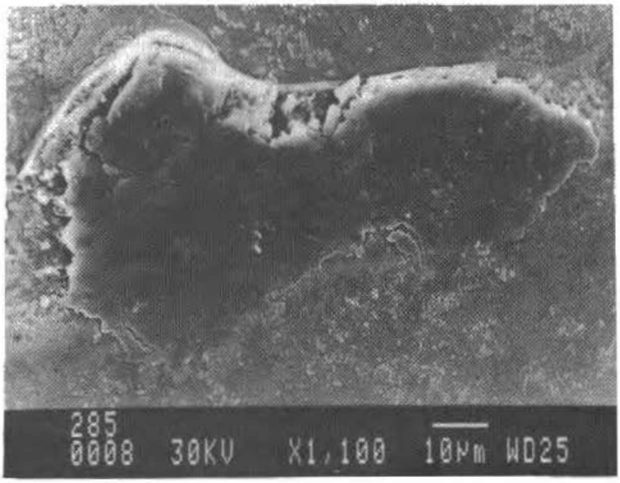

Fig. 1 Hydrogen Blistering In ASTM 285 Grade G Sample (1100x)

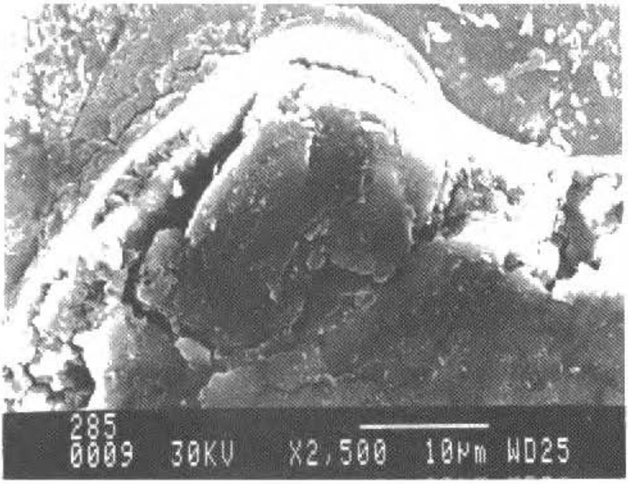

Fig. 2 Hydrogen Blistering in ASTM 285 Grade G Sample(2500x)

Fig. 3 Hydrogen Blistering in ASTM 516 Grade 70 Sample (4000x)

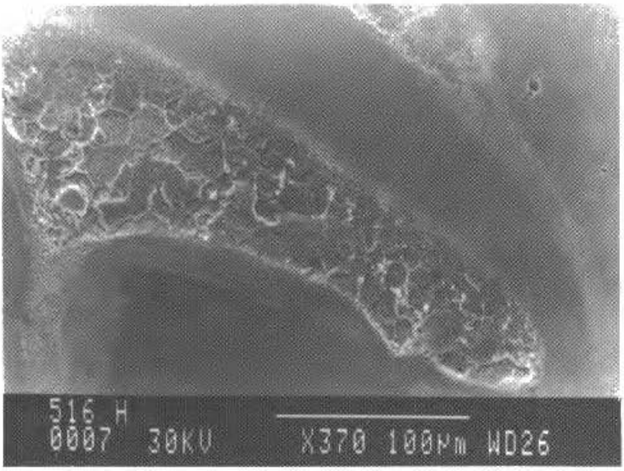

Fig. 4 Hydrogen Blistering in ASTM 516 Grade 70 Sample (370x)

Figures 5 to 8 show hydrogen induced cracking in the ASTM 285 sample, caused by a mechanism similar to the one wich caused blistering. However, in this case the molecular hydrogen wich was generated promoted a tension level larger than the steel breaking point tension. Figures 9 to 11 show hydrogen induced cracking in the ASTM 516 sample by the same mechanism. Blisterings can also be observed in Fig. 9 and deteriorated regions in Figs. 10 and 11.

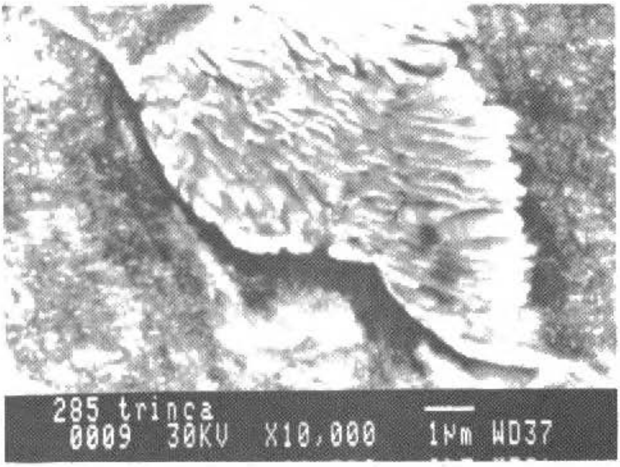

Fig. 5 Hydrogen Induced Cracking in ASTM 285 Grade G Sample (Nital 5% - 10000x)

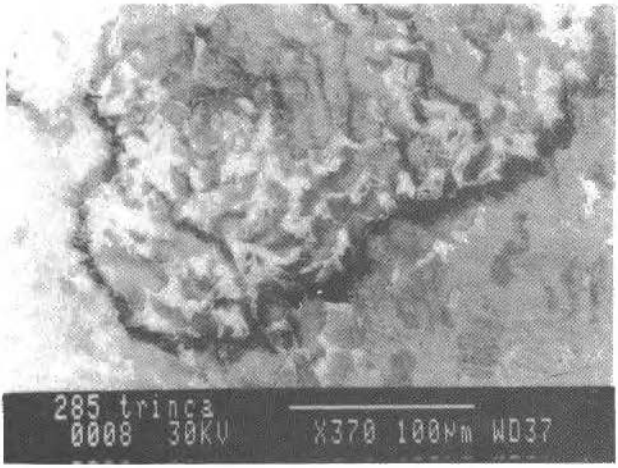

Fig. 6 **Hydrogen Induced Cracking in ASTM 285 Grade G Sample (Nital 5% - 370x)**

Fig. 7 **Hydrogen Induced Cracking in ASTM 285 Grade G Sample (550x)**

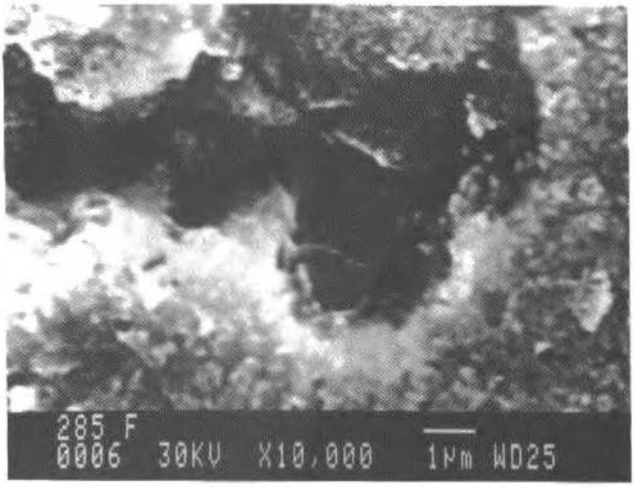

Fig. 8 Hydrogen Induced Cracking in ASTM 285 Grade G Sample (5000x)

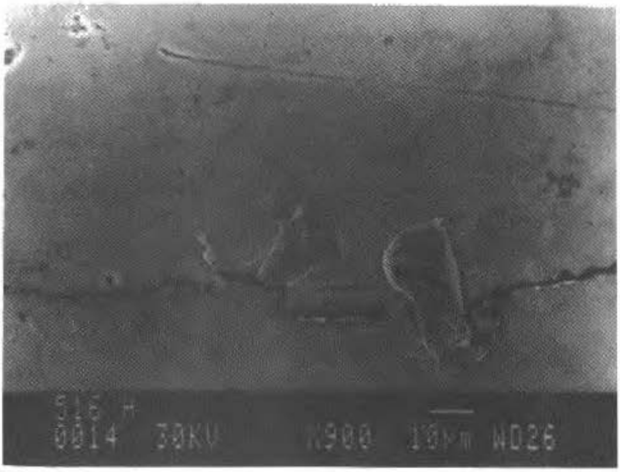

Fig. 9 Hydrogen Induced Cracking in ASTM 516 Grade 70 Sample (900x)

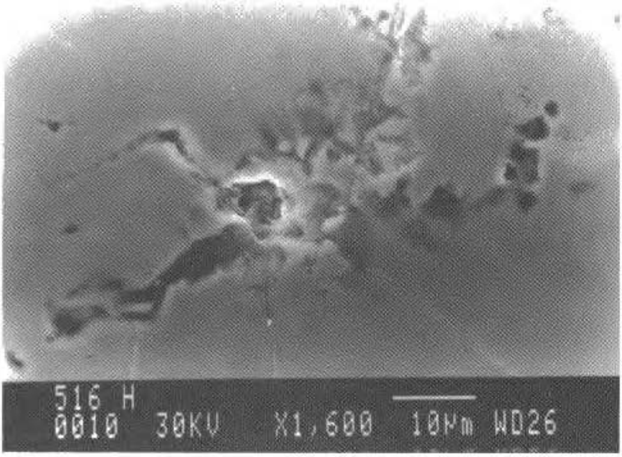

Fig. 10 Hydrogen Induced Cracking in ASTM 516 Grade 70 Sample (1600x)

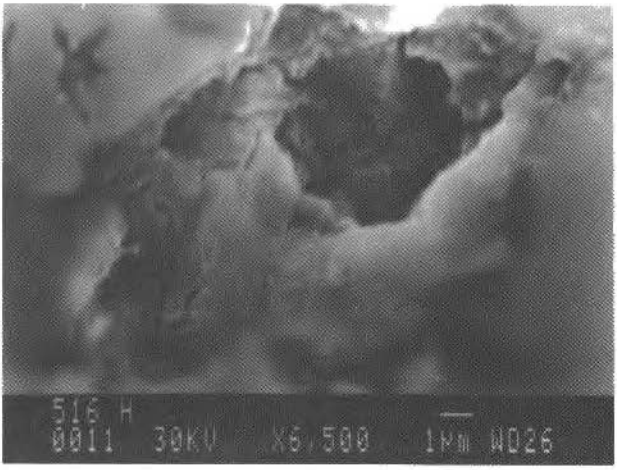

Fig. 11 Hydrogen Induced Cracking in ASTM 516 Grade 70 Sample (6500x)

Figures 12 and 13 show grain boundary deteriorated regions in the ASTM 285 sample, generate by the accumulated hydrogen molecules. Figures 14 and 15 show grain boundary deteriorated regions in the ASTM 516 sample.

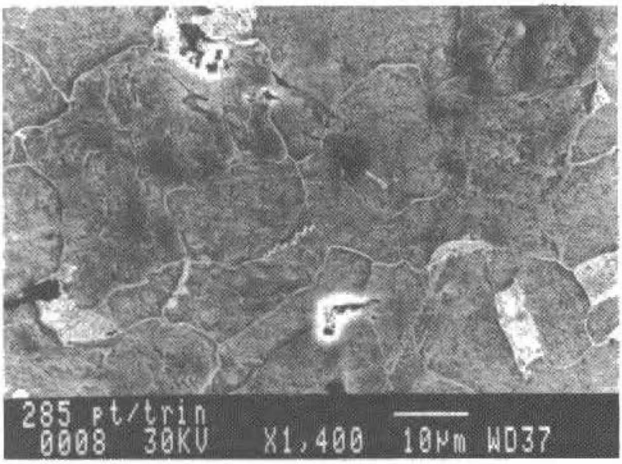

Fig. 12 Grain Boundary Deteriorated Regions in ASTM 285 Grade G Sample (Nital 5% - 1400x)

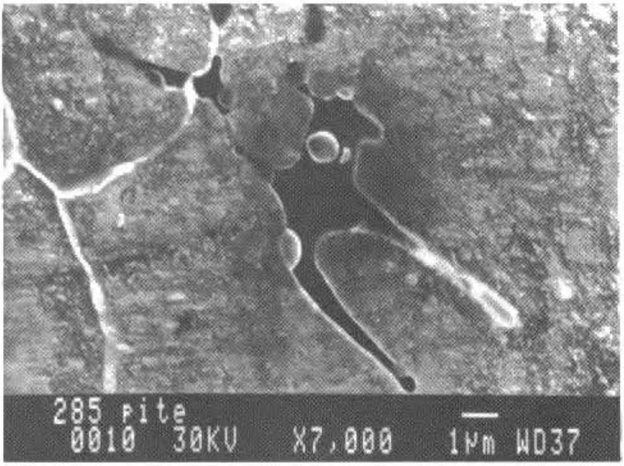

Fig. 13 Grain Boundary Deteriorated Regions in ASTM 285 Grade G Sample (Nital 5% - 7000x)

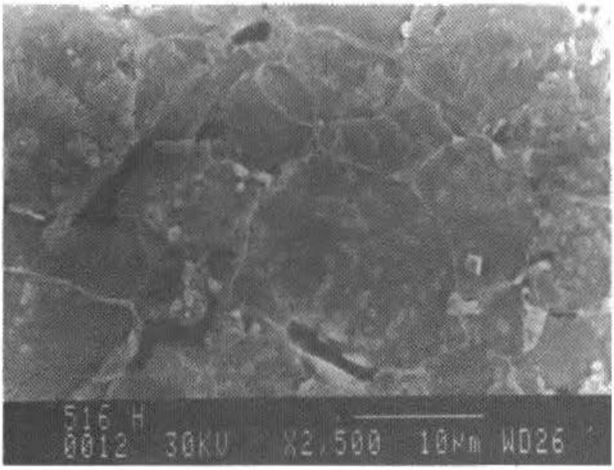

Fig. 14 Grain Boundary Deteriorated Regions in ASTM 516 Sample (Nital 5% - 2500x)

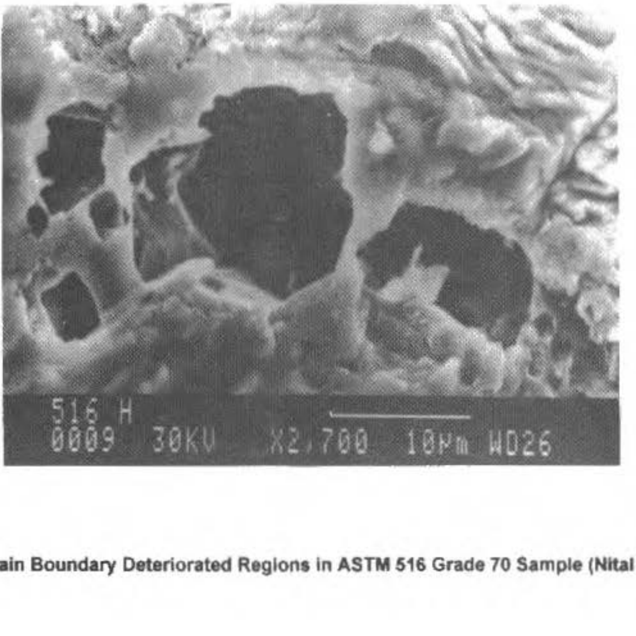

Fig. 15 Grain Boundary Deteriorated Regions in ASTM 516 Grade 70 Sample (Nital 5% - 2700x)

Figures 16 and 17 show the deterioration wich ocurred close to inclusions in the ASTM 285 and ASTM 516 samples, generated by molecular hydrogen accumulation in these structural defects. Grain boundary deterioration can also be observed in Fig. 17.

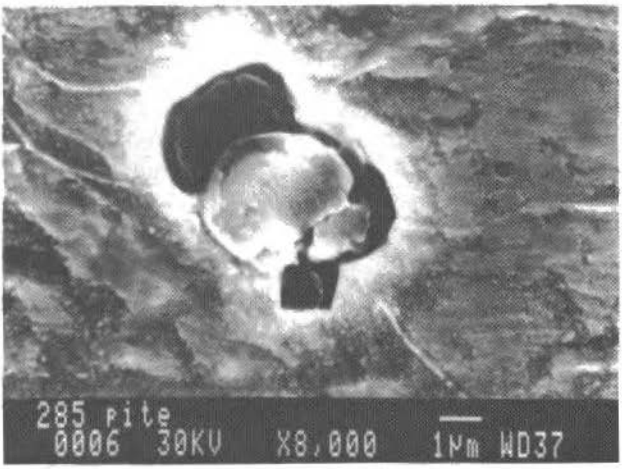

Fig. 16 Deterioration Close to Inclusions in the ASTM 285 Grade G Sample (8000x)

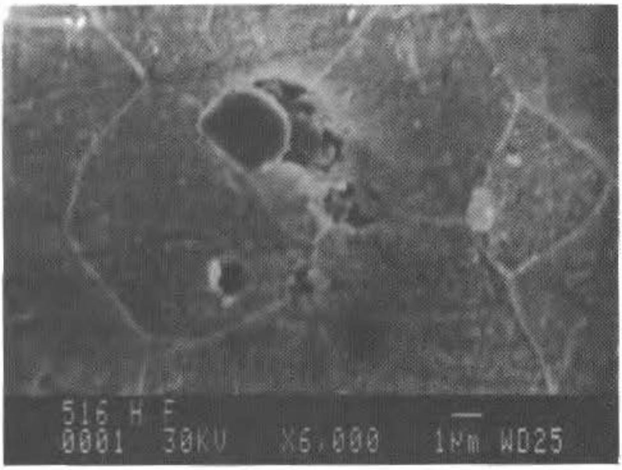

Fig. 17 Deterioration Close to Inclusions in the ASTM516 Grade 70 Sample (6000x)

Comparing the damage caused by hydrogen in the ASTM 285 grade G and ASTM 516 grade 70 samples, which could be identified by scanning electron microscopy, one observe the same types of deterioration in both steels, wich suggests the same hydrogen diffusion behavior on the samples, at the experimental conditions adopted. Although the ASTM 516 steel is a silicon-killed steel, it still has defects wich are favorable to hydrogen damage, as in the ASTM 285 steel. However, the fact that the ASTM 516 steel is a steel without internal stresses can be very important concerning sour water corrosion suceptibility.

Conclusions

The scanning electron microscopy observations suggest the same hydrogen diffusion behavior on the samples, for the experimental conditions which were adopted.

Both types of steel tested presented the same types of damage caused by hydrogen. Hence, from this point of view, it does not proceed the move to substitute the ASTM 285 steel for the ASTM 516 steel in catalytic cracking units of petroleum refineries.

References

Alefeld, G., 1978, "Hydrogens in Metals", Springer-Verlag, Berlin, Germany.

Eberhart ,M.E., 1985, Latanision, R.M.,Johnson, K.H., "A Molecular Orbital Model of Intergranular Embrittlement",Acta Met., Vol. 33, pp.1969-1973.

Edmondson, J.G.and Rue, J.R., 1992,"Wet H_2S Corrosion and Inhibition", Corrosion92/NACE, 441, 2, p. 441/1-441/8.

Ehmke, E.F., 1991,"Polyssulfide Stops FCCU Corrosion", Hydrocarbon Processing, Vol. 4, pp. 149-155.

Fontana, M.G., 1987, "Corrosion Engineering", Third edition,McGraw-Hill International Editions, New York.

Goldstein, J.I., 1992,"Scanning Electron Microscopy and X-Ray Microanalysis", Second Edition, Plenun Press, London.

JXA-840A Electron Probe Microanalisator, JEOL.

Morris, D. R., Sastri, V. S., Elboujdani, M., and Revie, R. W., 1994, "Electrochemical Sensors for Monitoring Hydrogen in Steel", Corrosion Engineering 5, 8, p.641-647.

Proença, M. B., Freire, C.M. A., Santos, M.B., and Arantes, D.R., 1996, "Hydrogen Monitoring in Catalytical Cracking Vessel Steels with Eletrochemical Impedance Spectroscopy", Braszilian Journal of Chemical Engineering 13, 4, p.240-249, december.

REPLAN 0024, Relatório de Inspeção da Unidade de Craqueamento Catalítico, Código 7530-748-02870.

Schutt,H.U., 1993,"Intergranular Wet Hydrogen Sulfide Cracking", MP/November, 9, pp. 55-60.

Strong, R.C., Majestic, V.K., and Wilhelm,S.M., 1991," Basic Steps Lead to Successful Corrosion Control", Oil & Gas Journal, 8, pp. 81-84, 30 september.

RBCM - J. of the Braz. Soc. Mechanical Sciences
Vol. XIX - No.1 - 1997

ISSN 0100-7386
Printed in Brazil

Abstracts

Soares, M., Mendes, P. R. S., and Naccache, M. F., 1997, "Heat Transfer to Viscoplastic Fluids in Laminar Flow Through Isothermal Short Tubes", RBCM - J. of the Braz. Soc. Mechanical Sciences, Vol. 19, No. 1, pp. 1-14.

The heat transfer problem that accurs during the laminar flow of a Herschel-Bulkley fluid through the entrance portion of tubes is studied. The Nusselt number is obtained as a function of the axial coordinate, yield stress, and power-law exponent. The thermal boundary condition of uniform wall temperature is examined. Among other results, it is seen that the developing length decreases as the fluid behavior departs from the Newtonian one.

Keywords: Non-Newtonian Fluid Heat Transfer, Viscoplastic Fluid, Laminar Flow, Entrance-Region Flow, Uniform Wall Temperature.

Guimarães G., Teodoro E. B., and Fhillip P. C., 1997, "On Optimizing the Estimation of Thermophysical Properties", RBCM - J. of the Braz. Soc. Mechanical Sciences, Vol. 19, No. 1, pp. 15-29 (In Portuguese).

This work presents an analysis of an experimental technique for simultaneous determination of the thermal conductivity and the thermal diffusivity of non metallic materials. The properties are determined by using the parameter estimation method. The experimental temperatures on the frontal and back surfaces of a sample are compared with their respective theoretical values obtained from the mathematical model. The heat flux evolution at the front surface and the heat loss evolution at the back surface are used as the boundary conditions. The purpose of this work is to investigate the ideal shape of the heat flux evolution, its duration and optimum measurement time. This information is important to guide designers on optimizing the parameters estimation.

Keywords : Optimization, Parameter Estimation, Experimental Techniques, Thermal Properties Measurements, Inverse Problems

Awruch, A. M., and Ehlers, C. F., 1997, "Vibration and Dynamic Instability Analysis of Turbomachinery Blades and Airfoils", RBCM - J. of the Braz. Soc. Mechanical Sciences, Vol. 19, No. 1, pp. 30-47.

Computational methods for determining natural frequencies and to study buckling and dynamic instability of turbomachinery blades and airfoils are presented here. A beam element with four degrees of freedom per node together with subspace interation method are used to calculate frequencies and vibration modes. Stability due to non conservative forces is analysed using a beam element with six degrees of freedom per node and the QZ method is employed to compute eigenvalues.

Keywords: Turbomachinery Blades and Airfoils, Vibration Analysis, Dynamic Instability, Finite Elements.

Sánches Filho, E. S., 1997, "Plastic Analysis of Bending-Torsion of Thin-Walled Beams", 1997, RBCM - J. of the Braz. Soc. Mechanical Sciences, Vol. 19, No. 1, pp. 48-57 (In Portuguese).

This paper presents the basic expressions of the Plasticity Theory which allow the formulation of the bending-torsion in the plastic regime for which the equilibrium equations are deduced, showing the change of position of the shear center in the plastic section. The combined forces in the section are also presented.

Keywords: Plastic Analysis, Bending-Torsion, Thin-Walled Beams.

Miyagi, P. E., Arata, W. M., and Moscato, L. A., 1997, "Application of PFS Model (Production Flow Schema) Based Analysis of Manufacturing Systems for Performance Assessment", RBCM - J. of the Braz. Soc. Mechanical Sciences, Vol. 19, No. 1, pp. 58-71.

The present work shows a modeling procedure for discrete manufacturing systems based on Production Flow Schema (PFS). A systematic approach to construct GSPN (Generalized Stochastic Petri Net) models is proposed, whose isomorphism with Markov process allows the extraction of quantitative data. The paper addresses a way to get information that is meaningful for manufacturing systems instead of using probabilities of the states of the Markov chain. Finally, a procedure to perform a sensitivity analysis allows to assess the influence of the quantitative parameters on system behavior.

Keywords: Manufacturing System, Modeling Methodology, Petri Nets, Performance Evaluation, Quantitative Analysis

Palma, E. S., 1997, "Effect of Porosity on the Strength Coefficient and Strain-Hardening Exponent of Sintered Ferrous Materials", RBCM - J. of the Braz. Soc. Mechanical Sciences, Vol. 19, No. 1, pp. 72-79.

Some features of strain hardening of porous materials during tensile tests are considered. Modelling of true stress-true strain curves were done by using Ludwik's equation. The influence of porosity on the strain hardening exponent and on the strength coefficient for porous Fe, Fe-C, Fe-C-Cu and Fe-P alloys is presented and experimental results are discussed and compared with the literature.

Keywords: Sintered Materials, Strain Hardening, Mechanical Properties, Effects of Porosity

Araújo, F. A., Andery, P. R. P., and Helman, H., 1997, "An Analysis Of The Mechanical Behaviour Of Bimetalic Strips Under The Plain Strain Compression Test", RBCM - J. of the Braz. Soc. Mechanical Sciences, Vol. 19, No. 1, pp. 80-91 (In Portuguese).

In this work, a theoretical model describing the mechanical behaviour of bimetalic strips under the plain strain compression test (Ford test), is presented. The model allows to predict the pressure distribution on the tool/strip contact surface, the compression loads and the apparent yield curves of the metals when in the pair, from the knowledge of the yield curves of each metal.

Keywords: Plain Compression Test, Slab Method, Cladding, Ford Test, Bimetalic Composites.

Proença, M. B., Freire, C. M. A., and Aoki, C., 1997, "Hydrogen Damage Analysis in Catalytical Cracking Units Steels of Petroleum Refineries by Scanning Electron Microscopy", RBCM - J. of the Braz. Soc. Mechanical Sciences, Vol. 19, No. 1, pp. 92-103.

Corrosion of vessels and piping made of steel by sour water in catalytical cracking units of petroleum refineries generate atomic hydrogen. Large part of this hydrogen will go to the atmosphere as H_2, a fraction will diffuse in the steel lattice and stay in the defects, while the balance will diffuse through the lattice. The most well known effect in these steels is blistering and cracking induced by the retained fraction of hydrogen. In this work scanning electron microscopy was used to identify the damage caused by hydrogen and the damage susceptibility of two steels commonly used in catalytical cracking vessels.

Keywords: Hydrogen Damage, Scanning Electron Microscopy, Catalytical Cracking Vessel Steel.

Note for Contributors: Articles on Disk

- Authors are strongly encouraged to submit the final accepted manuscripts on disk, using text editors for Windows or Word for Windows.
- The disk must be marked with the paper identification number and software used. Two copies of the printout should be included.

FORMULÁRIO DE AFILIAÇÃO

ASSOCIAÇÃO BRASILEIRA DE CIÊNCIAS MECÂNICAS
Av. Rio Branco, 124 - 18º andar - 20040-001 Rio de Janeiro - RJ
Tel.: (021) 221-0438 - Fax.: (021) 222-7128
e-mail: abcmaifs@ omega.lncc.br
CGC 83.431.593/0001-78

INDIVIDUAL

Por favor, preencha os dois lados do formulário.

Nome ______________________________

Endereço Residencial ______________________________

CEP ______________ Cidade ______________ Estado ______________

País ______________ Tel.: ( )______________ Fax: ( )______________

E-mail ______________________________

Empresa ______________________________

Dept./Divisão ______________________________ Posição ______________

Endereço Comercial ______________________________

CEP ______________ Cidade ______________ Estado ______________

País ______________ Tel.: ( )______________ Fax: ( )______________

E-mail ______________________________

Candidato-me a: ☐ Admissão ☐ Mudança de Categoria

Na categoria de: ☐ Sócio efetivo ☐ Sócio Aspirante

Solicito enviar correspondência para o seguinte endereço:

☐ Comercial ☐ Residencial

Data ______________ Assinatura ______________________________

Para uso da ABCM

Aprovado ______________ Data ______________ Sócio nº ______________

FORMAÇÃO E EXPERIÊNCIA PROFISSIONAL

Por favor, liste em ordem cronológica os dados completos de sua formação e experiência profissional. A falta desses dados impedirá o processo de admissão. Obrigado.

FORMAÇÃO ACADÊMICA

Graduação -	Área	Anos	a
	Instituição	País	
Mestrado -	Área	Anos	a
	Instituição	País	
Doutorado -	Área	Anos	a
	Instituição	País	
Outro -	Área	Anos	a
	Instituição	País	

EXPERIÊNCIA PROFISSIONAL

Empresa ______ Anos ______ a ______
Natureza da atividade ______ Posição ______

Empresa ______ Anos ______ a ______
Natureza da atividade ______ Posição ______

Empresa ______ Anos ______ a ______
Natureza da atividade ______ Posição ______

Indique até um máximo de 8 áreas de acordo com os códigos numéricos do Anexo.

Áreas de Especialização ______

Aplicação ______

Comentários ______

Área de Especialização

Especifique no Formulário de Afiliação os códigos numéricos das suas Áreas de Especialização e de Aplicação (verso).

1000	**Fundamentos e Métodos Básicos em Mecânica Teórica e Aplicada**
1010	Mecânica do Contínuo
1110	Método dos Elementos Finitos
1120	Método dos Elementos de Contorno
1130	Métodos Assintóticos
1140	Método das Diferenças Finitas
1150	Outro Métodos em Mec. Computacional
1210	Métodos Estocásticos e Estatísticos
1310	Modelagem
1410	Fundamentos de Análise Experimental
1510	Metrologia
1610	Gerência de Projetos
2000	**Dinâmica e Vibrações**
2110	Cinemática e Dinâmica
2210	Vibrações de Sólidos - Fundamentos
2310	Vibrações - Elementos de Estruturas
2320	Vibrações - Estruturas
2330	Propagação de Ondas em Sólidos
2340	Impacto em Sólidos
2350	Identificação de Parâmetros
2420	Propagação de Ondas em Fluidos
2510	Interação Fluido-Estrutura
2610	Astronáutica - Mec. Celeste e Orbital
2710	Explosão e Balística
2810	Acústica
3000	**Controle e Otimização**
3110	Projeto e Teoria de Sistemas Mecânicos
3210	Sistemas de Controle Ótimo
3220	Sistemas de Controle Adaptativo
3230	Aplicações em Sistemas e Controle
3310	Robótica
3410	Otimização de Sistemas e Processos
4000	**Materiais**
4110	Biomateriais
4120	Materiais Metálicos
4130	Materiais Cerâmicos
4140	Materiais Poliméricos
4150	Materiais Conjugados
4210	Conformação Mecânica
4300	Caracterização e Controle Microestrutural
4410	Comp. Mecânico dos Materiais
4420	Comp. Mec. Mat. - Baixas Temperaturas
4430	Comp. Mec. Mat. - Altas Temperaturas
4440	Comp. Mec. Mat. - Carregamto. Variável
4450	Comp. Mec. Mat. - Carregamto. Dinâm.
4500	Mecanismos de Fratura
4600	Mecânica da Fratura
4710	Ensaios Destrutivos
4720	Ensaios Não-Destrutivos
4800	Corrosão
5000	**Mecânica dos Sólidos**
5010	Elasticidade Linear
5020	Elasticidade Não-Linear
5030	Viscoelasticidade
5040	Plasticidade
5050	Visco-Plasticidade
5060	Mecânica dos Materiais Conjugados
5070	Mecânica dos Meios Porosos
5110	Reologia
5210	Cabos, Hastes e Vigas
5220	Membranas, Placas e Cascas
5230	Estruturas - Geral
5240	Estruturas - Contato com o Solo
5250	Estruturas - Submersas/Semi-submersas
5260	Estruturas - Móveis
5270	Estruturas - Vasos e Contenção
5310	Mecânica dos Solos - Básico
5320	Mecânica dos Solos - Aplicações
5330	Mecânica das Rochas
5410	Efeitos Eletro-Magnéticos em M. Sólidos
5420	Efeitos Térmicos em M. dos Sólidos
5510	Estabilidade de Estruturas
5520	Comportamento após a Flambagem
5530	Estados Limites e Cargas de Colapso
5540	Acomodação e Acúmulo de Dano
5610	Mecânica de Fratura
5650	Tribologia
5655	Atrito e Desgaste
5710	Componentes de Máquinas
5720	Acoplamentos e Juntas Não-Soldadas
5800	Análise Experimental de Tensões
6000	**Mecânica dos Fluidos**
6010	Reologia
6110	Hidráulica
6210	Escoamento Incompressível
6220	Escoamento Compressível
6230	Escoamento Rarefeito
6240	Escoamento em Meios Porosos
6250	Magneto-Hidrodinâmica e Plasma
6270	Escoamento Multifásico
6310	Camada Limite - Contorno Sólido
6320	Camada Limite - Contorno Livre
6410	Escoamento Interno - Dutos, Canais, etc
6430	Escoamento com Superfície Livre
6510	Estabilidade de Escoamento
6520	Turbulência
6530	Hidrodinâmica - Veículo de Estrut. Naval
6540	Aerodinâmica
6610	Mec. Fluidos - Aplicações em Máquinas
6650	Lubrificação
6710	Transientes em Fluidos
6810	Téc. Expertal. e Visualização Escoamento
7000	**Termociências**
7010	Termodinâmica
7110	Transp. de Calor - Convec. Monofásica
7120	Transp. de Calor - Convec. Bifásica
7130	Transp. de Calor - Condução
7140	Transp. de Calor - Radiação/Mod. Comb
7150	Transp. de Calor - Dispositivos/Sistemas
7210	Termodinâmica dos Sólidos
7310	Transporte de Massa
7410	Combustão
7420	Combustão em Leito Fluidizado
7510	Acionadores e Dispositivos de Propulsão
8000	**Geociências**
8010	Micromeritics
8110	Meios Porosos
8210	Geomecânica
8310	Mecânica dos Abalos Sísmicos
8410	Hidrologia, Oceanografia, Meteorologia
9000	**Energia e Meio Ambiente**
9110	Combustíveis Fósseis
9120	Sistemas Nucleares - Fissão
9125	Sistemas Nucleares - Fusão
9130	Sistemas Geotérmicos
9140	Sistemas Solares
9150	Sistemas Eólicos
9160	Sistemas de Energia Oceânica
9210	Armazenamento de Energia
9220	Distribuição de Energia
9310	Mecânica dos Fluidos Ambiental
9410	Mecânica de Dispositivos de Armazenamento de Resíduo
10000	**Biociências**
10110	Biomecânica
10210	Ergonomia
10310	Reabilitação
10410	Mecânica nos Esportes

Áreas de Aplicação

Exemplo: um especialista em Mecânica dos Fluídos (família 6000) atuando na área de Turbulência (6520), deverá escolher a Área de Aplicação 350, se estiver trabalhando em Propulsão.

010	Acústica e Controle de Ruído
020	Aplicações em Biociências
030	CAD
040	CAM
050	Componentes de Máquinas
060	Controle Ambiental
070	Controle de Qualidade
080	Criogenia
090	Engenharia e Física de Reatores
100	Engenharia de Petróleo
110	Engenharia Oceanográfica
120	Equipamentos de Processos
130	Equipamentos Industriais
140	Fontes Alternativas de Energia
150	Forjamento
160	Fundição
170	Garantia de Qualidade
180	Indústria Têxtil e Tecnologia Correlata
190	Inspeção e Certificação
200	Instalações Industriais
210	Instrumentação
220	Lubrificação Industrial
230	Mancais e Rolamentos
240	Máquinas Ferramentas
250	Máquinas de Fluxo
260	Máquinas Motrizes
270	Mecânica Fina
280	Metalurgia Geral e Beneficiamento de Minério
290	Metrologia
300	Mineração e Metalurgia Extrativa
310	Óptica
320	Pontes e Barragens
330	Processos de Fabricação
340	Projeto de Estruturas
350	Propulsão
360	Prospecção e Propulsão
370	Servo Mecanismos e Controle
380	Siderurgia
390	Sistemas Hidráulicos
400	Sistemas Pneumáticos
410	Soldagem
420	Solicitações Acidentais - Efeitos de Vento, Sismo, Explosão, Fogo e Inundação
430	Tecnologia de Alimentos
440	Tecnologia Mineral
450	Transporte (excluído veículos)
460	Transmissão de Energia
470	Tratamento Térmico e Termoquímico
480	Tubulações Industriais e Nucleares
490	Usinas Hidrelétricas
500	Usinas Termoelétricas
510	Vácuo
520	Vasos de Pressão, Trocadores de Calor e Equipamentos Pesados
530	Veículos - Terrestres, Espaciais e Marítimos

Information for Authors

SCOPE AND POLICY

• The purpose of the Journal of the Brazilian Society of Mechanical Sciences is to publish papers of permanent interest dealing with research, development and design related to science and technology in Mechanical Engineering, encompassing interfaces with Civil, Electrical, Chemical, Naval, Nuclear, Agricultural, Materials, Petroleum, Aerospace, Food, System Engineering, etc., as well as with Physics and Applied Mathematics.

• The Journal publishes Full-Length Papers, Review Papers and Letters to the Editor. Authors must agree not publish elsewhere a paper submitted to and accepted by the Journal. Exception can be made for papers previously published in proceedings of conferences. In this case it should be cited as a footnote on the title page. Copies of the conference referees reviews should be also included. Review articles should constitute a critical appraisal of published information.

• The decision of acceptance for publication lies with the Editors and is based on the recommendations of at least two ad hoc reviewers, and of the Editorial Board, if necessary.

SUBMISSION

• Manuscripts and all the correspondence should be sent to the Editor or, alternatively, to the appropriate Associate Editor.

• Four (4) copies of the manuscript are required. The author should submit the original figures, which will be returned if the paper is not accepted after the review process.

• Manuscripts should be submitted in English or Portuguese. Spanish will also be considered.

• A manuscript submitted for publication should be accompanied by a cover letter containing the full name(s) of author(s), mailing adresses, the author for contact, including phone and fax number, and, if the authors so wish, the names of up to five persons who could act as referees.

FORMAT

• Manuscripts should begin with the title, including the english title, the abstract and up to five key words. If the paper's language is not English, an extended summary of about 500 words should be included. The manuscript should not contain the author(s) name(s).

• In research papers, sufficient information should be provided in the text or by refering to papers in generally available Journals to permit the work to be repeated.

• Manuscripts should be typed double-spaced, on one side of the page, using A-4 sized paper, with 2 cm margins. The pages should be numbered and not to excess 24 pages, including tables and figures. The lead author of a RBCM paper which exceeds the standard length of pages will be assessed a excess page charge.

• All symbols should be defined in the text. A separate nomenclature section should list, in alphabetical order, the symbols used in the text and their definitions. The greek symbols follow the English symbols, and are followed by the subscripts and superscripts. Each dimensional symbol must have SI (Metric) units mentioned at the end. In addition, English units may be included parenthetically. Dimensionless groups and coefficients must be so indicated as dimensionless after their definition.

• Uncertainties should be specified for experimental and numerical results.

USTRATIONS AND TABLES

• Figures and Tables should be referred in consecutive arabic numerals. They should have a caption and be placed as close as possible to the text first reference.

• Line drawings should be prepared on tracing paper or vellum, using India ink; line work must be even and black. Laser print output is acceptable. The drawings with technical data/results should have a boundary on all four sides with scale indicators (tick marks) on all four sides. The legend for the data symbols should be put in the figure as well as labels for each curve wherever possible.

• Illustrations should not be larger than 12 x 17 cm. Lettering should be large enough to be clearly legible (1.5-2.0 mm).

• Photographs must be glossy prints.

REFERENCES

• References should be cited in the text by giving the last name of the author(s) and the year of publication of the reference: either "Recent work (Smith and Jones, 1985) ... or "Recently Smith and Jones (1985) With four or more names, use the form "Smith et al.(1985)" in the text. When two or more references would have the same text identification, distinguish them by appending "a", "b", etc., to the year of publication.

• Acceptable references include: journal articles,dissertations, published conference proceedings, numbered paper preprints from conferences, books, submitted articles if the journal is identified, and private communications.

• References should be listed in alphabetical order, according to the last name of the first author, at the end of paper. Some sample references follow:

Bordalo, S.N., Ferziger, J.H. and Kline, S.J., 1989, "The Development of Zonal Models for Turbulence", Proceedings, 10th ABCM - Mechanical Engineering Conference, Vol. I, Rio de Janeiro, Brazil, pp. 41-44.

Clark, J.A., 1986, Private Communication, University of Michigan, Ann Arbor, MI.

Coimbra, A.L., 1978, "Lessons of Continuum Mechanics", Editora Edgard Blucher Ltda, São Paulo, Brazil.

Kandlikar. S.G. and Shah, R.K., 1989, "Asymptotic Effectiveness - NTU Formulas for Multiphase Plate Heat Exchangers", ASME Journal of Heat Transfer, Vol. 111, pp. 314-321.

McCormak, R.W., 1988, "On the Development of Efficient Algorithms for Three Dimensional Fluid Flow", Journal of The Brazilian Society of Mechanical Sciences, Vol. 10, pp. 323-346.

Silva, L.H.M., 1988. "New Integral Formulation for Problems in Mechanics", (in portuguese), Ph.D. Thesis, Federal University of Santa Catarina, Florianópolis, SC, Brazil.

Sparrow, E.M., 1980a, "Forced-Convection Heat Transfer in a Duct Having Spanwise-Periodic Rectangular Protuberances", Numerical Heat Transfer, Vol. 3, pp. 149-167.

Sparrow, E.M., 1980b, "Fluid-to-Fluid Conjugate Heat Transfer for a Vertical Pipe-Internal Forced Convection and External Natural Convection", ASME Journal of Heat Transfer, Vol. 102, pp. 402-407.

ISSN 0100 7386

JOURNAL OF THE BRAZILIAN SOCIETY OF MECHANICAL SCIENCES
REVISTA BRASILEIRA DE CIÊNCIAS MECÂNICAS

VOL. XIX - No. 1 - MARCH 1997

Non-Newtonian Fluid Heat Transfer

Experiment Design

Turbomachinery Dynamics

Plastic Analysis

Analysis of Manufacturing Systems

Mechanical Properties of Sintered Materials

Roll Cladding

Hydrogen Damage in Steel